Vierbundelmenging in siliciumgebaseerde nanofotonische circuits
met een geoptimaliseerde dispersiekarakteristiek
voor telecommunicatie- en sensortoepassingen

Four-Wave-Mixing
in Dispersion-Engineered Silicon Nanophotonic Circuits
for Telecommunication and Sensing Applications

Bart Kuyken

Promotoren: prof. dr. ir. R. Baets, prof. dr. ir. G. Roelkens
Proefschrift ingediend tot het behalen van de graad van
Doctor in de Ingenieurswetenschappen

Vakgroep Informatietechnologie
Voorzitter: prof. dr. ir. D. De Zutter
Faculteit Ingenieurswetenschappen en Architectuur
Academiejaar 2012 - 2013

UNIVERSITEIT
GENT

ISBN 978-90-8578-601-6
NUR 965
Wettelijk depot: D/2013/10.500/34

Universiteit Gent
Faculteit Ingenieurswetenschappen en Architectuur
Vakgroep Informatietechnologie

Promotoren: Prof. dr. ir. Roel Baets
Prof. dr. ir. Günther Roelkens

Examencommissie:

Prof. dr. ir. Rik Van de Walle (voorzitter)	Universiteit Gent, ELIS
Prof. dr. ir. Roel Baets (promotor)	Universiteit Gent, INTEC
Prof. dr. ir. Günther Roelkens (promotor)	Universiteit Gent, INTEC
Prof. dr. ir. Peter Bienstman	Universiteit Gent, INTEC
Prof. dr. ir. Geert Morthier	Universiteit Gent, INTEC
Prof. dr. ir. Jeroen Beeckman	Universiteit Gent, ELIS
Prof. dr. Serge Massar	Université Libre de Bruxelles, LIQ
dr. Nathalie Picqué	CNRS, Max-Planck-Institut für Quantenoptik

Universiteit Gent
Faculteit Ingenieurswetenschappen en architectuur

Vakgroep Informatietechnologie
Sint-Pietersnieuwstraat 41, B-9000 Gent, België

Tel.: +32-9-264.33.16
Fax.: +32-9-331.35.93

Dit werk kwam tot stand in het kader van een aspirantenbeurs van het Fonds voor Wetenschappelijk Onderzoek - Vlaanderen (FWO - Vlaanderen).

Proefschrift tot het behalen van de graad van
Doctor in de Ingenieurswetenschappen
Academiejaar 2012-2013

Dankwoord

De afgelopen jaren waren voor mij een ongelooflijk avontuur. Eigenlijk begon dit avontuur een jaar voordat ik mijn doctoraat begon, toen ik het nieuws kreeg dat mijn BAEF-beurs was toegekend. Die beurs liet mij toe om een jaar naar Amerika te gaan. Het was prof. Roel Baets die mij op de hoogte had gebracht van deze beurs en ook de nodige hulp heeft aangeboden bij het voorbereiden van de applicatie. Zo kwam ik in contact met de fotonica groep in Gent en toen ik terug kwam naar België ben ik dan ook zonder twijfelen begonnen aan een doctoraat in deze groep met Roel als promotor. Bedankt hiervoor. Een groep waar ik vrijwel niemand kende, maar vrij snel ongelooflijke toffe mensen leerde kennen. Dit werd me voor de eerste maal echt duidelijk op een fotonica-event in Brussel (ik zoek de naam wel eens op, voor de geïnteresseerden) waar we (Peter, Eva, Diedrik, Thijs en Nannicha) laat gebleven waren en dan maar uiteindelijk een hotel hadden geboekt. Ik herinner mij vooral hoe vegetarische Dierdik 's avonds eenvoudig overtuigd kan worden door pitta-proppers om vlees te eten. Dat event (met de beste wil van de wereld kan ik er geen betere naam voor vinden) is ook de plaats waar ik Stéphane Clemmen de eerste maal ontmoette. Wat heel belangrijk was, bleek later in mijn eerste doctoraatsjaar. Shankar suggereerde toen om eens naar de niet-lineaire eigenschappen van 'zijn'amorf silicium te kijken. Het bleek al snel dat dit inderdaad wel eens de moeite kon zijn. Het enigste probleem was dat we in Gent niet de nodige apparatuur hadden om dit 'te goei'op te meten. Op naar de ULB, en naar Stéphane, hier werd ik met open armen ontvangen door hem en Prof. Serge Massar om naar hartenlust experimenten te doen in hun labo. Die periode koester ik nog altijd als één van de spannendste in mijn doctoraat. We ontdekten plots dat dit amorf silicium, zo leek het toch, ongeveer het beste materiaal, en om het kinderlijk te zeggen, ter wereld was om niet-lineaire experimenten mee te doen. Het voelde echt aan als een ontdekking, we werkten hard, maar hadden vooral heel wat geluk. Amai! Goed, later bleken er toch wel wat problemen te zijn, maar komaan zeg, hoeveel mensen maken zoiets mee! Een dank je wel aan Shankar, Stephane en Serge is toch wel zeker op zijn plaats.

In de lente van dat jaar begon ik meer en meer te werken met Günther, nu prof. Gunther Roelkens, maar toen nog niet en de eerste indruk is de belangrijkste heb ik van horen zeggen. Dit bracht mijn onderzoek in een echte stroomversnelling. Hij bracht mij in contact met dr. Willam Green. Ik heb Gunther daar ooit eens

voor bedankt, maar ben daar voor uitgelachen geweest. Dit ga ik dus geen tweede maal doen, kwestie van de ezel stoot enz... Maar goed, resultaat was toch maar dat ik de zomer van 2010 in New York kon gaan wonen. Ongelooflijke stad daar niet van, maar ik ga er hier geen reisgids van maken en proberen te focussen op wat er daar in het IBM Watson Research Center is gebeurd. Ik moet eerst zeggen dat ik daar ongelooflijk goed ontvangen ben door dr. William Green en Xiaoping Liu. Thank you very much guys. The summer of 2010 was a really exciting time, I learned a lot from you guys. Later ben ik verschillende malen terug gegaan en steeds weer was ik welkom. Enorm veel resultaten in dit werk zijn een rechtstreeks gevolg van die bezoeken. Maar goed terug naar de zomer van 2010, of nee, wacht even ik was vergeten zeggen dat ik Yannick al daarvoor had leren kennen en dat wij wel goed overeenkwamen. Maar nu echt terug naar de zomer van 2010, of nee, beter de herfst, eind september is het toch al herfst? Hoe dan ook, het was conferentie in Denver en ik, Joris, Koen en Yannick zijn daar naar toe gegaan. Ik kwam rechtstreeks van New York. Nu wie zijn Koen en Joris? Wel beste lezer, dit zijn twee mannen, nu begin de dertig, die toen ik begon in de groep in hun laatste jaar zaten en die mij enorm geholpen hebben bij een groot aantal experimenten. Echte experimentalisten dus! Soit, de conferentie: ongelooflijk plezant, ik herinner mij vooral de laatste avond waar we met de internationale fotonica sterren (of is het eerder krampachtig vastklampen, och ja, we kenden ze toch van zien) naar een karaoke bar zijn gegaan. Wat was dat allemaal?

Nu goed, ik ga hier niet jaar per jaar en al helemaal niet seizoen per seizoen alle avonturen uit de doeken doen. Ik was goed bezig maar het zou mij te ver drijven. Het eerste jaar dat ik hierboven beschreven heb heeft sowieso de toon gezet, het is, denk ik, wel duidelijk. Geef me een seintje als je meer wil weten. Toch wil ik het nog hebben over een aantal andere labo bezoeken, meestal met Francois (of was het nu Leo? In feite is het ook dr.). Wat was het nu weer allemaal? Twente, Munchen en de Sterre, juist? Op de TU Twente gaat mijn dank uit naar Prof Klaus Boller en Joern. Munchen was sowieso het leukst. Laat me vooral dr. Nathalie Picque bedanken om dit bezoek mogelijk te maken, maar ook Birgitta en Christine voor ons zo goed te ontvangen. Ik denk geregeld terug aan de vreemde situaties met Martin, maar ook het tafelvoetbaltoernooi waar we de finale hebben verloren omdat jij, Francois, zogezegd beter kon spelen als je 'iets'gedronken hebt. En dan was er nog de Sterre, of moet ik zeggen de kinderboerderij. We hebben geen resultaten behaald, maar toch bedankt Prof. Rik van Deun en Pieter voor jullie steun.

Ondertussen in Gent en niet op volgorde: zo veel hoogtepunten! Laten we beginnen op mijn bureau. Karel, je vindt dat ik te veel babbel, maar volgens mij babbel jij gewoon te weinig. We hebben het toch goed gehad, spijtig dat jij vroeger bent weggegaan, voor mij had je daar zeker nog tot oktober kunnen zitten. Aan de lezer: Karel heeft wel degelijk zijn doctoraat behaald. Martin, ons meest romantische vogeltje van de bureau, met de eeuwige foto van Leen naast hem, spijtig dat je niet meer op onze bureau zit. Marie, het levende bewijs dat je een prille relatie, de aankoop van een woning en een verbouwing helemaal kunt combineren met je werk. Wel toch niet helemaal, maar het was toch wel soms morantisch met onze

Wout. Nebiyu, I hope you find something even more exciting to do next year. En dan natuurlijk Yannick: bff! Nu beste lezer, we zijn met meer dan vijftig in onze groep ik kan dus niet iedereen afzonderlijk afgaan in elke andere bureau, maar toch doe ik een beetje mijn best (ja ja, hoe kan je nu een 'beetje 'je best doen?). Peter (en ook Hanne), we hebben het toch goed gehad in New York en Berlijn, maar ook in Gent en recent in Brussel, met je chique 'troi pièce'appartement. Eva, met het enorme aanstekelijke enthousiasme, enorm tof dat je er ook telkens bij was (aan de lezer, ik heb het nu niet over Berlijn en New York). Thijs, waarom ben jij nu eigenlijk terug in Nederland gaan wonen? Diedrik, ik heb het al over je gehad. Thomas, den teeveevee, die altijd heel klein schrijft, wanneer gaan wij nu eens echt samen naar de kapper? Martijn, den Tassaert, ooit ga ik wel eens naar jouw koor gaan kijken. En dan is er nog onze Elewout, ik denk nog vaak terug aan ons El Sandwijo experiment. We moeten het geld dat iedereen heeft voorgeschoten en niet terugevraagd heeft eens dringend verdelen tussen ons gedrieën (beste lezer, je kan nog altijd goed tellen 1 + 1 is nog altijd twee, het is namelijk zo dat Yannick ook in de El Sandijo organisatie zit. In feite is hij zelfs naar eigen zeggen CFO). Ongelooflijk hoeveel jij (naast El Sandwijo dan wel te verstaan) voor de groep hebt gedaan, zeker naar afscheidscadeaus toe. Trouwens ga jij nu naar Spanje verhuizen? Dit doet er mij er aan denken dat ik zeker even de koppeltjes op het werk bedank om te tonen wat liefde is (en soms een beetje te overdrijven, soms krijg ik het gevoel dat het een wedstrijd is voor jullie) Sam en Pauline, mooi! Marie en Wout, ook mooi! Cristina en Elewout, zeker mooi! Dan hebben we natuurlijk ook nog Kristof, met zijn gouden handjes. Eén keer over de gêne heen om ten (on)gepaste tijde gemasseerd te worden, kan je er wel van genieten. Beste lezer, ik kan je bijna horen fronsen, maar ik mag dit zeggen want iedereen doet het bij ons op het werk, dit is normaal.

En dan zijn er nog wat ik noem de Jonge Wolven: Raphaël (Rafke), Wuytens, Utsav en de Peyskens. Ik denk dat jullie goed bezig zijn! Shahram, de vriendelijkste en vrolijkste persoon op de bureau. Gunay, nee jij hebt nu eens geen gouden handen. En onze Mid-Ir crew: Ik wil natuurlijk de hele crew bedanken, maar in het bijzonder Muhammad, Aditya, Chen, Nannicha en Alban, it was really great working with you guys! En ook nog mijn bedanking aan Ananth en Servagya (en hier ook Aditya) om een nieuwe vibe te introduceren. Zoveel 'ennen'! En toch, ook met Kristien, Peter, Ilse (2), Jeroen en Liesbet was het fantastisch werken. Maar ook de andere proffen in de fotonica-groep Wim, Dries, Peter, Geert en Nicolas moet ik hier even bedanken voor hun toegankelijkheid En nog maar eens een 'en'

En dan mag ik zeker niet Eric, Pankaj, Daan en Sarah vergeten, het was altijd zeer leuk om jullie begeleider te zijn.

Er is natuurlijk ook nog Gent. Wat een ongeloofelijke stad om in te leven. We wonen nu misschien al niet allemaal meer in Gent, maar kom, heeft onze bende het niet ongelooflijk goed? Is het niet leuk dat we elkaar al zolang kennen? Ik vind van wel en ik hoop dat dit blijft duren. Beste lezer, ik zou de namen van iedereen kunnen afgaan, maar iets meer dan drie pagina's lijkt genoeg. Ik hou alleszins van jullie allemaal, en beste lezer in het ietwat melige kader van dit dankwoord hou ik ook van jou.

Laat me wel nog ons Helena bedanken, wij hebben het ook echt goed en we kennen elkaar ook al lang en ik hoop dat het ook blijft duren! En natuurlijk hou ik in het bijzonder van jou. En als laatste wil ik ook heel graag mijn ouders en mijn zus bedanken! Wat een fantastische tijd was het in de Jovastraat.

Gent, Mei 2013
Bart Kuyken

Table of Contents

List of Figures

Nederlandse samenvatting –Summary in Dutch–

1 Silicium fotonica

Optische verbindingen, verbindingen waarlangs de informatie via licht wordt overgebracht, hebben een enorm potentieel om lange, trage elektrische verbindingen op een chip te vervangen en zo nog snellere chips in de toekomst mogelijk te maken. Ondanks de enorme uitdaging om deze zogenaamde fotonische circuits te integreren met elektronische circuits, is er de laatste jaren enorm veel vooruitgang gemaakt. In het bijzonder zijn silicium fotonische circuits, circuits waar de golfgeleiders uit silicium gemaakt zijn, de laatste tien jaar snel geëvolueerd van een academische curiositeit naar een goed ontwikkeld platform voor optische interconnecties op een chip. Deze fotonische circuits kunnen gemaakt worden in een standaard CMOS productielijn met standaard CMOS processen en machines. Dit heeft een enorm voordeel: er kan worden voortgebouwd op de heel betrouwbare en goed ontwikkelde productietechnologie gebruikt voor het maken van elektronische circuits. Zodoende hebben deze fotonische chips een groot potentieel om op een betrouwbare en goedkope manier op heel grote schaal te worden geproduceerd. Deze chips zijn daarenboven ook heel nuttig voor de telecommunicatiewereld omdat de chips transparant zijn in het telecommunicatievenster (rond een golflengte van 1310 nm en 1550 nm) en een heel hoge densiteit van optische functies kunnen huizen. Maar ook in de context van biosensoren kunnen deze chips gebruikt worden om op nanoschaal analyses uit te voeren. Voorlopig gebeurt dit laatste met licht rond telecommunicatiegolflengtes, maar deze sensoren zouden potentieel veel nauwkeuriger en gevoeliger kunnen zijn als ze licht met langere golflengtes zouden gebruiken. De absorptie van verschillende moleculaire verbindingen is immers veel sterker bij langere golflengtes. Op figuur 1, is bij wijze van voorbeeld, de absorptie van CO_2 te zien, waar bij langere golflengtes de absorptie veel sterker is dan in het telecommunicatievenster.

2 Geïntegreerde niet-lineaire optica

Als in een materiaal de geïnduceerde polarisatie een niet-lineaire functie is van het aangelegde elektrisch veld, zal het zich gedragen als een niet-lineair optisch medium. Het niet-lineaire effect dat gebruikt wordt in dit werk is het optische

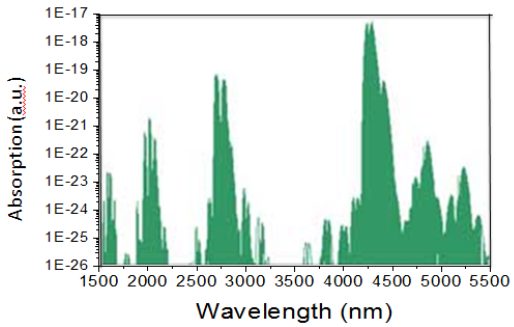

Figuur 1: De absorptie van CO_2 in functie van golflengte. De absorptie bij langere golflengtes is grootteordes sterker dan bij 1550 nm.

Kerr effect. Dit is een heel breedbandig en snel effect, het is een derde orde niet-lineariteit: de niet-lineaire polarisatie is proportioneel met de derde macht van het elektrisch veld.

Er zijn twee belangrijke verschillen tussen een niet-lineair systeem en een lineair systeem. Een eerste verschil is dat het superpositie principe niet meer geldt, dit betekent dat het signaal gegenereerd aan de uitgang van het niet-lineaire systeem als gevolg van twee ingangssignalen niet de superpositie is van de de afzonderlijke uitgangen wanneer de signalen afzonderlijk zouden worden aangelegd: de signalen interageren in het materiaal. Een tweede verschil als gevolg van het werken in een niet-lineair systeem, is dat aan de uitgang van een niet-lineair systeem, in het geval een sinusoïdaal signaal wordt aangelegd, een sinusoïdaal signaal met niet noodzakelijk dezelfde frequentie verschijnt. Deze twee eigenschappen worden in dit doctoraatswerk uitgebuit om enerzijds aan ultra-snelle optische dataverwerking rond telecommunicatiegolflengtes te doen en anderzijds om licht te genereren bij lange golflengtes door licht met kortere golflengtes te mengen. De niet-lineaire respons van een (amorfe) silicium golfgeleider kan heel sterk zijn, als gevolg van de hoge intensiteiten die bekomen worden omdat het licht in een kleine cross-sectie geduwd wordt in zo een golfgeleider. Daarenboven is de niet-lineaire respons van het golfgeleidermateriaal ook heel sterk. Figuur 2 toont een foto van een silicium golfgeleider die duidelijk maakt dat het licht heel erg zit samengepakt. Een niet-lineair interactie is altijd afhankelijk van de sterkte van het elektrisch veld, hoe hoger de intensiteit hoe sterker de niet-lineaire interactie. Zodoende is het mogelijk om niet-lineaire optische functies te bekomen in korte golfgeleiders op een chip bij redelijke vermogens.

3 Resultaten

Het grote voordeel van silicium golfgeleiders ten opzichte van andere platformen is dat ze CMOS compatibel zijn (chalcogenide golfgeleiders zijn bijvoorbeeld niet

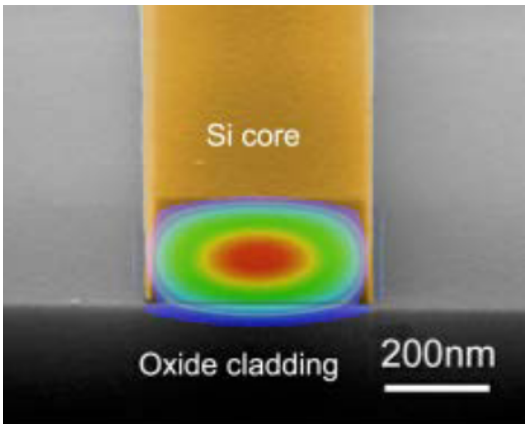

Figuur 2: Een rasterelektronenmicroscoop foto van een silicium optische golfgeleider. Door het grote indexcontrast tussen het silicium en zijn omgeving zit het licht samengepakt in een heel kleine doorsnede. De optische mode is gesuperponeerd op de foto. Foto ui [1]

CMOS compatibel) en dat ze ten opzichte van andere soorten golfgeleiders een heel sterke niet-lineaire repsonse vertonen (ongeveer 100 maal sterker dan de niet-lineaire repsons in siliciumnitride golfgeleiders en hydex golfgeleiders). Het grote nadeel aan silicium is dat het materiaal een sterke niet-lineaire absorptie coëfficiënt vertoont bij golflengtes in het telecommunicatievenster: de twee-fotonabsorptie. De sterke niet-lineaire absorptie heeft de efficiëntie van niet-lineaire processen in het telecommunicatievenster enorm gehinderd in silicium golfgeleiders. In dit werk worden twee oplossingen voorgesteld om rond het probleem van de niet-lineaire absorptie te geraken.

De eerste oplossing is om een ander CMOS compatibel materiaal met minder twee-fotonabsorptie te gebruiken om optische niet-lineaire functies te implementeren in het telecommunicatievenster. In dit werk worden CMOS compatibele gehydrogeneerde amorfe silicium golfgeleiders voorgesteld als alternatief voor de kristallijne silicium golfgeleiders om aan niet-lineaire optica te doen in het telecommunicatie venster. Er wordt aangetoond dat de niet-lineaire absorptie in amorfe silicium golfgeleiders veel zwakker is dan in een kristallijne silicium golfgeleider, maar dat tezelfdertijd de Kerr niet-lineariteit veel sterker is. Er wordt experimenteel een optische versterker aangetoond die korte signaalpulsen kan versterken met meer dan 26 dB. Figuur 3 toont de versterking van zwakke 3.8 ps signaalpulsen in functie van de golflengte van deze pulsen door 3.8 ps pomp pulsen met een piek vermogen van 5.3 W. Dit is een verbetering met een factor 100 in vergelijking met wat in kristallijn silicium mogelijk is [2]. Daarenboven is het potentieel van het platform nog eens aangetoond in een experiment waar een snel 320 GBit/s data signaal via een niet lineair proces optisch werd bemonsterd doordat de efficiëntie opnieuw 100 maal sterker is dan in gelijkaardige experimenten in kristallijn silicium [3].

Een tweede oplossing is om een mid-infrarood pomp signaal te gebruiken. De mid-infrarode pomp fotonen met een energie, die kleiner is of in de buurt is van de halve band kloof energie van silicium, zullen geen twee-fotonabsorptie ondervinden. Door de dispersie in de silicium golfgeleiders goed te ontwerpen wordt het mogelijk het faseverband tussen de signaal-, idler- en pompgolven met heel verschillende frequenties te linken. Op deze manier wordt het mogelijk om een telecommunicatiesignaal te versterken met 13 dB.

Daarenboven wordt er in dit werk ook aangetoond dat het mogelijk is om mid-infrarode signalen te manipuleren. Zo wordt er aangetoond dat het mogelijk is om mid-infarode signalen te versterken met 50 dB. Er wordt verder ook aangetoond dat het mogelijk is om door het proces van supercontinuumgeneratie een breed spectrum dat uitstrekt van 1535 nm tot 2550 nm te genereren in een 2 cm lange silicium golfgeleider door deze te pompen met nauwbandige mid-infarood pomp pulsen. Er wordt bovendien ook aangetoond dat het mogelijk is om een telecomsignaal te converteren naar het mid-infarood. Zo is het resultaat van een conversie te zien op figuur 4: een telecommunicatiesignaal met een golflengte van 1535 nm is geconverteerd naar een golflengte van 3635 nm met behulp van een mid-infrarode pomp.

Kortom, in dit werk wordt aangetoond dat door het gebruik van een mid-infrarode pomp zeer efficiënte niet-lineaire interacties in kristallijn silicium mogelijk worden. Zo wordt er de versterking van een telecomsignaal met een mid-infrarode pomp aangetoond, maar ook de manipulatie van mid-infrarode signalen door een mid-infrarode pomp. Bovendien wordt er aangetoond dat in CMOS compatibele gehydrogeneerde amorfe silicium golfgeleiders efficiënte niet-lineaire interacties mogelijk worden in het telecommunicatievenster. Het materiaal heeft immers een lage twee-fotonabsorptie coefficiënt een sterke niet-lineaire respons in het telecommunicatie golflengtegebied.

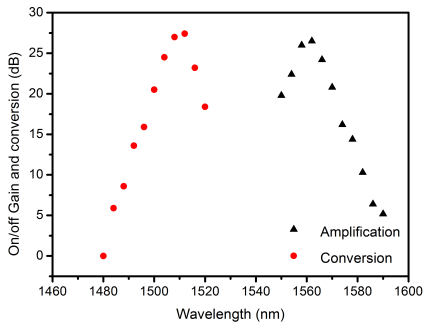

Figuur 3: De parametrische versterking in een amorfe silicium golfgeleider als functie van de signaalgolflengte.

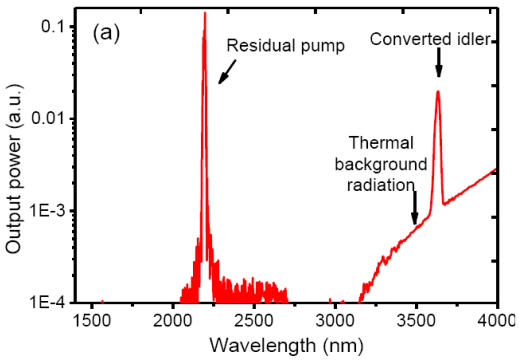

Figuur 4: Het uitgangsspectrum van een mid-infrarood lichtgenerator. Door het mixing van een krachige pomp (20 W piek vermogen, 2 ps lange pulsen) met een continu telecommunicatiesignaal bij 1565 nm wordt licht bij 3630 nm gegenereerd.

Referenties

[1] Pieter Dumon. *Ultra-compact Integrated Optical Filters in Silicon-on-insulator by Means of Wafer-Scale Technology*. PhD thesis, Ghent University, 2006.

[2] Mark a Foster, Amy C Turner, Jay E Sharping, Bradley S Schmidt, Michal Lipson, and Alexander L Gaeta. *Broad-band optical parametric gain on a silicon photonic chip.* Nature, 441(7096):960–3, June 2006.

[3] Hua Ji, Minhao Pu, Hao Hu, Michael Galili, Leif Katsuo Oxenlowe, Kresten Yvind, Jørn M Hvam, and Palle Jeppesen. *Optical waveform sampling and error-free demultiplexing of 1.28 Tb/s serial data in a nanoengineered silicon waveguide*. Lightwave Technology, Journal of, 29(4):426–431, 2011.

English summary

1 Silicon Photonics

On chip interconnects are envisioned to replace long, slow electrical interconnects to make future generations of chips faster. An enormous progress has been made in the past decade to integrate these so called photonic circuits with electronic integrated circuits. In particular silicon photonic circuits, circuits where the waveguides are made out of silicon have rapidly evolved from a scientific curiosity to a mature platform to make on chip interconnects. The photonic circuits can be made in a CMOS fab, using standard CMOS tools which has the enormous advantage that the circuits can leverage from this mature technology. As a consequence of the mature CMOS processing tools, silicon photonic circuits have the potential to lead to high yield, low cost, large volume devices. Furthermore the high density of integration of optical functions as well as the transparency of silicon at telecom wavelengths (1310 nm and 1550 nm) allows to use these chips for telecom and datacom applications as well. Another upcoming field where silicon photonic circuits are used is in the context of biosensing, where an analyte can be probed at the nanoscale. The sensitivity and accuracy of the latter category of chips can potentially be increased by several orders of magnitude by stepping away from the telecommunication wavelength window. At wavelengths beyond the telecom window, the absorption of many molecular bonds increases by orders of magnitude. Figure 5 shows the absorption of CO_2 as a function of wavelength. The absorption of the gas is much stronger at longer wavelengths than in the telecom window.

2 Integrated nonlinear optics

When the induced polarization in a material is a nonlinear function of the applied electric field, the optical system behaves nonlinear. The optical nonlinear effect used in this work is the Kerr effect. It is known to be very broadband and ultrafast. The Kerr effect is a so called third order nonlinearity. The nonlinear polarization is proportional to the third power of the electric field. Working with a nonlinear optical material, has two major consequences used in this work. The first one is that the superposition principle does not hold anymore such that the output of a nonlinear system generated by two signals, is not the superposition of the output of the signals going into the system separately: the signals interact in the material. The second consequence is that unlike in a linear system when a sine wave is

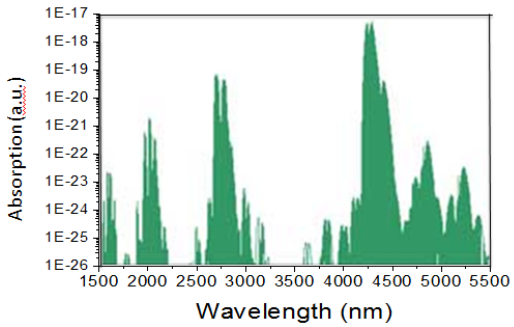

Figure 5: The absorption of CO_2 gas as a function of wavelength. The absorption at longer wavelengths is orders of magnitude higher than the absorption at 1550 nm.]

applied the output is not necessary a sine wave with the same frequency. These two properties are exploited to do ultra fast all optical signal processing of telecom signals as well as for the generation of coherent long wavelength light by mixing short wavelength sources. The nonlinear response of integrated waveguides can be very strong in silicon (and hydrogenated amorphous silicon) waveguides because of the high confinement leading to enormous intensities. Additionally the intrinsic material nonlinearity of silicon is very strong. Figure 6 shows the highly confined mode in a silicon waveguide. As a result nonlinear optical functionalities can be implemented in short waveguides at moderate powers.

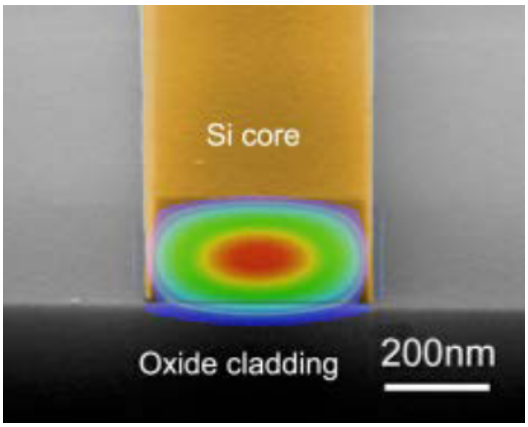

Figure 6: A scanning electron microscope image of a (crystalline) silicon photonic waveguide. The high index contrast between the silicon and its surrounding squeeze light into a very small area. The optical mode profile is superimposed on the picture.

3 Results

The main advantage of using silicon waveguides to integrate nonlinear optical functions as compared to other platforms such as chalcogenide planar circuits, silicon nitride planar circuits and hydex planar circuits is that silicon is a CMOS compatible material (while chalcogenide is not) and that the waveguides have a very high nonlinear response (two orders of magnitude higher than for hydex or silicon nitride waveguides). However, the two-photon absorption coefficient in silicon is very strong at telecommunication wavelengths. The two-photon absorption is a nonlinear absorption: the absorption is stronger when the optical intensities are higher. The two-photon absorption has limited the efficiencies of nonlinear optical functions in the telecommunication window enormously. In this work two solutions are presented to get around the problem of two-photon absorption.

The first solution is to use another CMOS compatible material with less tow-photon absorption to do nonlinear optics in the telecom wavelength range. In this work CMOS compatible hydrogenated amorphous silicon waveguides are proposed as an alternative platform for doing nonlinear optics at telecom wavelengths. It is demonstrated that the nonlinear absorption in the waveguides is much lower than in crystalline waveguides and that the Kerr nonlinearity is higher. Furthermore, an all-optical broadband amplifier is built using hydrogenated amorphous silicon waveguides, which is able to amplify short pulses by more than 26 dB. This result was an improvement of more than 20 dB over similar results obtained in crystalline silicon [1]. Figure 7 shows the optical amplification (and conversion efficiency) of a $\approx$ 3.8 ps signal pulse amplified by a 3.8 ps pump pulse at 1565 nm with a peak power of 5.3 W as a function of the wavelength of the signal pulse. The full potential of the platform is furthermore demonstrated in an all-optical signal processing setup, where a fast 320 Gbit/s data signal is optically sampled. Again this was an improvement of more than 20 dB as compared to similar experiments in crystalline silicon [2].

A second solution is to step away from the telecom wavelength window and use a pump wave with photon energies less than the half the band gap energy to eliminate the two-photon absorption in silicon. It is shown that by careful dispersion engineering the nonlinear four-wave mixing process can be phase matched for spectrally very distinct signal, idler and pump waves. The amplification of telecom signals by 13 dB by a mid-infrared pump is demonstrated in crystalline silicon waveguides.

In this work it is shown that efficient nonlinear optical functions in the mid-infrared are possible as well in these crystalline silicon waveguides. It is demonstrated that a high peak power mid-infrared wavelength pump pulse is able to amplify a mid-infrared wavelength pulse up to 50 dB in crystalline silicon waveguides. In another set of experiments a broadband light source spanning from 1535 nm up to 2550 nm is demonstrated by using the process of supercontinuum generation in a 2 cm long crystalline silicon photonic waveguide. The pump pulses used were narrow band 2 ps pulses centered at a wavelength of 2120 nm having a peak power of 12.7 W. Other experiments show that a telecom signal can be spectrally

translated, by using a long wavelength pump, up to 3630 nm. This is shown in figure 8. Furthermore a silicon based widely tunable optical parametric oscillator is demonstrated.

In short this work shows that nonlinear interactions in crystalline silicon can be very efficient when a mid-infrared pump is used. Both the amplification of telecom signals as well as the manipulation of mid-infrared signals is demonstrated. Additionally it is shown that hydrogenated amorphous silicon waveguides have a huge potential to integrate nonlinear optical functions for the telecom window on a chip. The material has a relatively low two-photon absorption coefficient, while it has a high nonlinear refractive index in the telecom wavelength range.

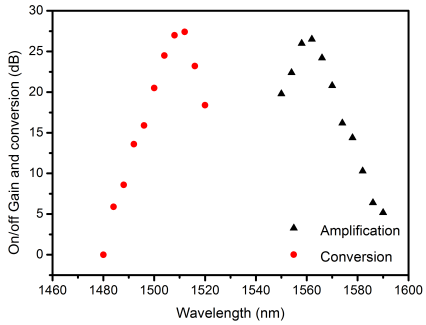

Figure 7: The amplification of the all-optical amplifier implemented in amorphous silicon. The amplificaton of the amplifier as a function of signal wavelength is shown.

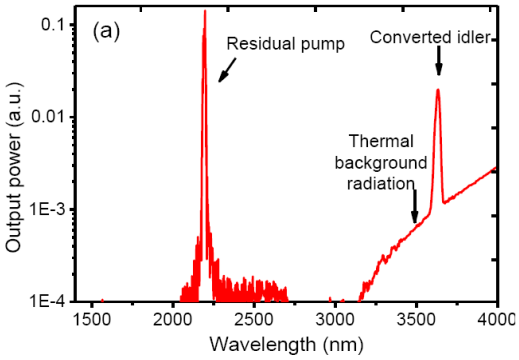

Figure 8: The recorded output spectrum showing the generated long wavelength light. By mixing a strong pump at 2190 nm (pulses with a peak power of 18.3 W) with a continuous wave signal at 1565 nm light at 3630 nm is generated.

References

[1] Mark a Foster, Amy C Turner, Jay E Sharping, Bradley S Schmidt, Michal Lipson, and Alexander L Gaeta. *Broad-band optical parametric gain on a silicon photonic chip.* Nature, 441(7096):960–3, June 2006.

[2] Hua Ji, Minhao Pu, Hao Hu, Michael Galili, Leif Katsuo Oxenlowe, Kresten Yvind, Jørn M Hvam, and Palle Jeppesen. *Optical waveform sampling and error-free demultiplexing of 1.28 Tb/s serial data in a nanoengineered silicon waveguide*. Lightwave Technology, Journal of, 29(4):426–431, 2011.

1 Introduction

1.1 The need for light on a chip

To increase the performance of computer chips, the amount of transistors, the digital building blocks of the electronic circuits on a chip, has to increase. This can be done by making these transistors smaller, such that more transistors can fit on a chip. Not long after the invention of the transistor, people have started trying to decrease the size of a transistor. This has been very successful: the amount of transistors on a chip has steadily increased. In fact, it was observed in 1965 that every two years the amount of transistors doubled. This empirical observation is now called Moore's law, after Gordon Moore [1]. Nowadays, because of the constant increase of the number of transistors on a chip, there can fit more than a billion transistors on one chip. This is in stark contrast with the thousands of transistors on a typical chip in the sixties. By clever engineering people overcame several hurdles in the past and newly designed chips were able to keep up with Moore's law. Nowadays one of the major hurdles is that the constant scaling of the transistors on a chip does not make the interconnections between these transistors any faster, in fact, it makes the average connections slower. Although contra intuitive, the speed of an electrical interconnect is not only dependent on its length. This can be understood when one looks in more detail at how an electrical signal is transferred by a connection. The electrical signals on a chip are encoded as a voltage. When one transistor wants to signal its output to another transistor's input it will rise the voltage on the electrical wire between the two.

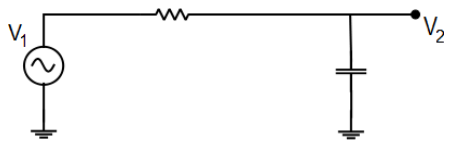

Figure 1.1: Lumped model of the interconnection between two transistors.

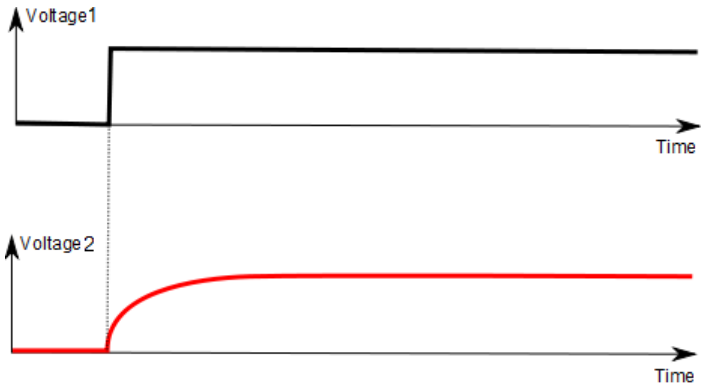

Figure 1.2: Evolution of the voltage measured by the second transistor.

The voltage as a function of time seen by the second transistor is not a step function. This is a result of the finite resistance of the wires (R) and the stray capacitance (C) to other wires, the substrate, etc. as schematically shown in figure 1.1. It takes a while for the second transistor to see the voltage swing induced by the first transistor (see figure 1.2). This delay will be proportional to the time constant of the circuit, which is $\tau = RC$. A simplified schematic can be drawn for the interconnect, it is shown in figure 1.3. Simply put, it can be imagined that the electrical signal is carried by one of the two wires shown in figure 1.3 a), the other wire can be carrying another signal or can for example be a ground track. Both the wires have a finite area defined by its thickness and its width (w), they have a finite length (l) and are separated by a distance (d). The resistance of the wire will be proportional to its length and inversely proportional to its area. The stray capacitance of the wire will be proportional to its length and inversely proportional to the distance d. When all the dimensions in plane are scaled down, for example by a factor of two, the capacitance and the resistance of the wire will not alter. The resistance stays the same because at the same time the area of the wire as well as the length of the wire goes down by a factor of two. The capacitance of the wire is not altered because both its length L as well as the distance d goes down by a factor two. Which means that after scaling the dimensions in plane, the time constant for the interconnect will be the same. However, since we wanted more transistors on the same chip, the total chip area is not scaled. In reality it is even worse, as seen

in figure 1.4 the chip area has the tendency to increase over time. When the area stays the same or becomes larger the average connection will be longer, making the average connection slower. These slow connections limit the performance of the electronic circuit. To overcome this problem it is envisioned that at least the long (and thus slowest) wires on a chip need to be replaced by photonic wires carrying photons to transfer the information. Photons do not have the RC time constant plaguing the electric circuits and as a result transfer information very fast.

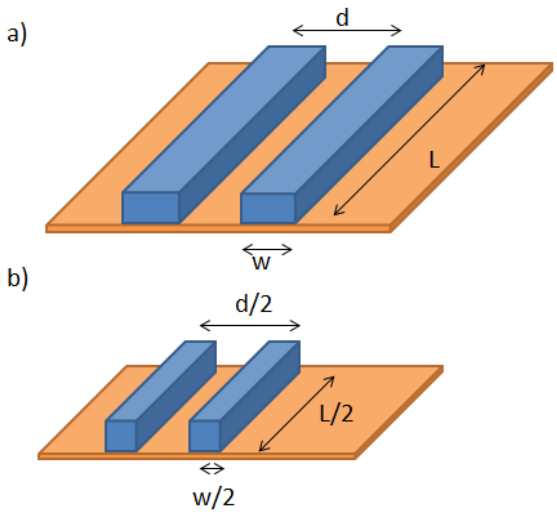

Figure 1.3: Easy model illustrating the effects on electric connections after scaling these down.

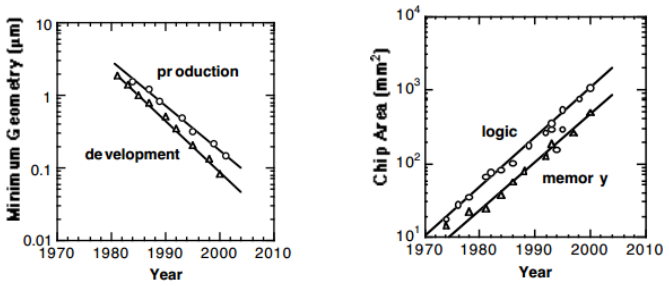

Figure 1.4: The average chip area of new chips as a function of time. Image from [2]

1.1.1 A photonic wire enabling optical interconnects

It turns out that it is possible to make photonic wires. These photonic wires can even be made in silicon. This is important, since this material is the basic material used in CMOS fabs to make standard electronic integrated circuits. A scanning electron microscope (SEM) image of such a photonic wire is shown in figure 1.5. In the picture the mode guiding the photons is superimposed. Light signals are guided because of total internal reflection as a result of the index contrast between the silicon core (n=3.4) of the waveguide and the surrounding silicon oxide cladding (n=1.45). These wires with sub-micron dimension and high confinement allow for photonic wires with very small bend radii [3]. Recently Germanium detectors [4] and fast small silicon modulators [5] were developed paving the path to real optical interconnects on chips. Figure 1.6 shows an artist impression used by IBM to show how such a photonic circuit can be integrated with a CMOS chip for on-chip communication but also for off-chip communication.

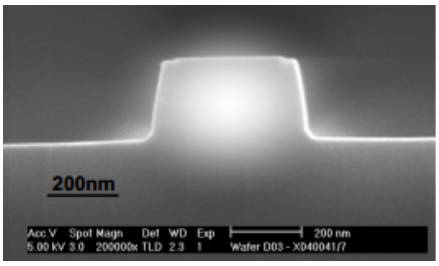

Figure 1.5: A SEM picture of a photonic wire in silicon. Picture from [6].

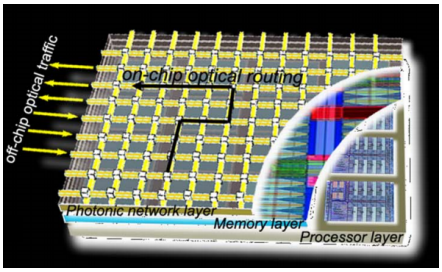

Figure 1.6: Artist impression for a chip with an integrated photonic layer. Picture from [7].

1.1.2 Alternative use of integrated silicon photonic circuits

1.1.2.1 Telecommunication and data communication applications

One of the most important aspects of silicon for photonic applications is that it is transparent at telecommunication wavelengths. The telecommunication wavelength window loosely defined around 1300 nm and 1550 nm is interesting because optical fibers have very good characteristics, most importantly they are low loss, at these wavelengths. Furthermore, the high density of integration as a result of the high refractive index contrast between silicon and the silicon cladding makes it possible to make very small footprint components for telecommunication applications. For example, complex wavelength multiplexers and demultiplexers [8] which can (de-)multiplex the different channels of data transmitted on slightly offset wavelengths have been designed. The main drawback with silicon, however, is that it has an indirect bandgap, which makes light generation in silicon very inefficient. Researchers have tried to overcome this problem, where the most promising methods so far are the integration of III-V materials with silicon by molecular [9] or benzocyclobutene bonding [10] at one side or by making a germanium lasers by engineering the bandgap of germanium [11]. These advancements give silicon photonic integrated circuits all the basic blocks needed in a photonic circuit.

1.1.2.2 Photonic sensors

Several photonic sensors such as bio sensors [12] and gas sensors [13] have been developed. At the moment these sensors are interrogated with light in the telecommunication wavelength range. However it is envisioned that similar sensors could potentially be orders of magnitude more sensitive when they use light at longer wavelengths. The silicon material used for the photonic wires is transparent up to 7 μm [14], although the silicon oxide is only transparent up to 4 μm. [14], still making the platform useful for wavelengths up to 4 μm. For example, Figure 1.7 shows the absorption of CO_2 gas as a function of wavelength. From the figure, it is clear that the absorption of CO_2 gas becomes many orders of magnitude stronger at longer wavelengths. Because of fundamental vibrational absorption of many molecular bonds in this wavelength range, many molecules have distinct absorption bands in the mid-infrared. Since the absorption bands are very wavelength specific and can act as a fingerprint of a molecular bond, this wavelength range is sometimes referred to as the molecular fingerprint range. Figure 1.8 shows graphically the molecular fingerprint region and the absorption bands of several interesting molecules.

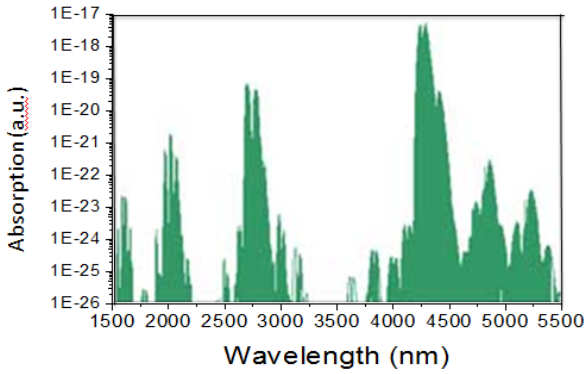

Figure 1.7: The absorption of CO_2 molecules as a function wavelength. Working at longer wavelengths has the enormous advantage that the absorption increases by orders of magnitude.

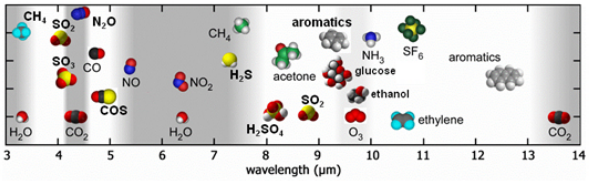

Figure 1.8: The absorption of a set of molecules in the mid-infrared wavelength range. The absorption is of the molecules is very wavelength selective. The wavelength selective absorption acts as a fingerprint for the molecule.Figure from [15].

1.2 Nonlinear optical functions

In a linear (time invariant) system signals can not interact with each other because the superposition principle holds in such systems, see figure 1.9. The eigenfunctions of these systems are complex exponentials. When a sine wave with an optical frequency ω is going through a time invariant linear optical medium, its frequency will not get altered, the medium can only change the amplitude and phase of the sine wave. When two optical signals travel through such a medium they will not feel each others presence. However, when a system has a nonlinear response, the superposition principle is not longer valid and two signals can interact in the system. This is shown in figure 1.10 for a third order nonlinear system. Complex exponentials are no longer eigenfunctions of the nonlinear system. When two sine waves are applied to the system a set of sine waves with not necessary the same frequency come out of the system. Furthermore, one optical signal can interact with another signal, for example in figure 1.10 at the output a cross term $3x(t)^2y(t)$ arises.

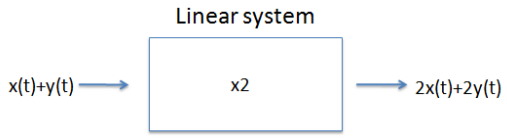

Figure 1.9: A linear system. In a linear system the output is a linear superposition of the outputs for the signals presented to the system

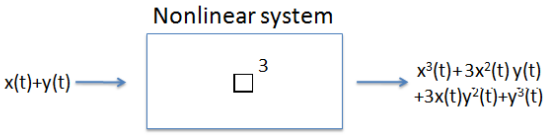

Figure 1.10: A nonlinear system. In a nonlinear system, the output is not a linear superposition of the outputs of signals presented to the system, some cross terms appear at the output as well.

For a nonlinear optical medium this means that it is possible to generate new optical frequencies, which are not applied to the system and let light beams interact.

1.3 Nonlinear optics in integrated circuits

In this work the nonlinear response coming from the nonlinear polarizability of the bound electrons is used. The nonlinear response from the bound electrons in a material is almost instantaneous [16] and broadband. The nonlinear optical polarization in, for example a third order nonlinear optical medium, can be written as

$$P_{NL} = \epsilon_0 \chi^{(3)} E^3 \tag{1.1}$$

The nonlinear response (P_{NL}) is stronger when the electric fields (E) are stronger. By using silicon waveguides in integrated circuits the electric fields can be very strong for rather low power beams because light in a silicon waveguide is confined to a very small area, giving rise to very strong intensities as shown in figure 1.11.

The combination of the broadband, fast nonlinearity in these waveguides at low powers is used to achieve optical functions useful for both telecommunication wavelengths (see 1.1.2.1) as well as for sensing applications in the mid-infrared (see 1.1.2.2). The very fast response can be used for doing all-optical signal processing at telecommunication wavelengths, which can not be done through con-

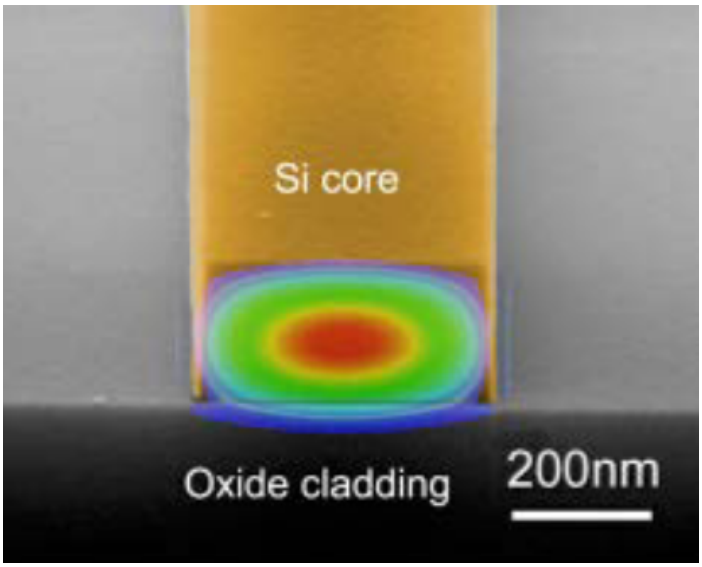

Figure 1.11: The mode profile in a silicon waveguide. The light is confined to a very small modal area. Courtesy of Dr. William Green from IBM T.J. Watson Research Center.

ventional electronic processing, while the generation of new optical frequencies is used to efficiently generate light at mid-infrared wavelengths using (short wavelength) infrared sources.

1.4 Non-silicon optical platforms with a nonlinear response

This section briefly describes waveguide platforms for nonlinear optical functions. For a nonlinear platform it is advantageous that the real part of the nonlinear parameter of the waveguide given by $\Re(\gamma) = \frac{n_2\omega}{Ac}$ is high. Here n_2 is the nonlinear refractive index of the material in the waveguide, A the effective mode area, ω the optical frequency and c the speed of light. The real part of the nonlinear parameter takes in account both the nonlinearity of the material as well as the confinement of the mode related to the mode area A and is as such a good parameter to quantify the nonlinear response of a waveguide. The imaginary part of the nonlinear parameter of the waveguide has to be as small as possible. The imaginary part of the nonlinear parameter is given by $Im(\gamma) = \frac{\beta}{2A}$. Here β is the nonlinear absorption coefficient and A the mode area. Since the nonlinear absorption scales with the intensity this parameter quantifies the (second order) nonlinear absorption. Additionally, it is also important to have control over the dispersion of the

waves traveling in a waveguide. By controlling the dispersion, it is possible to phase match the waves in the nonlinear optical process.

1.4.1 Fibers

1.4.1.1 Silica fibers

The loss of a standard single mode silica fiber can be very low such that long interaction lengths are possible. However, due to the relatively large modal area in the fiber and the low nonlinear refractive index of silica the nonlinear parameter γ of these fibers is very low: $\gamma = 1.5 \times 10^{-3} W^{-1} m^{-1}$. There is no nonlinear absorption in these fibers. A silica fiber with an increased nonlinear response is the so called highly nonlinear fiber (HNLF). By proper engineering of the refractive indices of the core and cladding layers, the modal area of these silica fiber is reduced. The fibers have a nonlinear parameter of about $\gamma = 20 \times 10^{-3} W^{-1} m^{-1}$. There is no nonlinear absorption observed in these fibers.

1.4.1.2 Non silica fibers

A whole set of non silica fibers such as chalcogenide ($\gamma = 1.2 W^{-1} m{-}1$ [17]) or Bismuth based fibers ($\gamma = 1.36 W^{-1} m{-}1$ [18]) exist. However, more interest is geared toward the silica based HNLF due to the low loss in these fibers, enabling long interaction lengths. Also more practical issues such as high durability, low splice losses to standard single mode fiber remain a problem for these fibers.

1.4.1.3 Micro structured fibers

The previous types of fiber consisted out of two glass cylinders of a more high index core and a lower index cladding. A whole new set of fibers was first proposed by [19] in the seventies. These micro structured fibers have a very complex refractive index profile. It was suggested that such micro structured fibers could guide the light by a photonic bandgap effect, and it is sometimes referred to as "a photonic crystal fiber". This new type of fiber allowed for much more degrees of freedom by designing the cladding of the photonic crystal fiber. This allowed for a very good control of the dispersion over a very broad wavelength range. Additionally, these fibers allowed for better confinement of the optical mode, which allowed for higher values for the nonlinear parameter ($\gamma \approx 1 W^{-1} m{-}1$). The combination of the control of the dispersion over a wide wavelength range while having a high nonlinear parameter has made this type fiber very attractive. It is the basic component of most commercial available supercontinuum sources.

1.4.2 Planar waveguide circuits

In the following sections a set of planar waveguide circuits used for nonlinear optics are discussed. The common characteristic for these technologies is that it is possible, by proper design of the cross sections of the waveguides, to control the (waveguide) dispersion of the optical modes on the chip. Additionally, the nonlinear parameters of these waveguides are much higher than in fiber because of the much higher refractive index contrast and thus higher confinement in the photonic circuits. In the following section the most relevant linear properties and nonlinear properties of these circuits are discussed.

1.4.2.1 Chalcogenide planar waveguide circuits

Chalcogenides glasses are a set of amorphous semiconductor materials which contain one or more chalcogen elements, such as sulphur, selenium and tellurium covalently bonded to network formers such as Ge, Sb, Ga, Si or P [20]. The relatively heavy atoms in the chalcogenide glasses makes the vibrational energies in the atomic bonds relatively low. Because of the low phonon energies in the material, chalcogenides are transparent up to very long wavelengths (10-20 um [20]). The chaclogenide glasses have a linear refractive index between 2 and 3 and a high nonlinear refractive index in the range of $10^{-17} - 10^{-18} W^{-1} m - 1$. The nonlinear parameters of these waveguides are in the range of $10 - 100 W^{-1} m^{-1}$ [21]. Two photon absorption is absent in these waveguides due to its high bandgap [20]. A whole set of nonlinear optical functions has been demonstrated in chalcogenide waveguides such as wavelength conversion [22] regeneration [23], demultiplexing [24], four-wave mixing gain [25] and supercontinuum generation [21]. Chalcogenide waveguides tend to have relatively low losses of about 1 dB/cm. The downside of chalcogenide glasses is that chalcogenide is not CMOS compatible.

1.4.2.2 Silicon nitride photonic circuits

Silicon nitride waveguides can be fabricated in a standard CMOS foundry [26]. The silicon nitride is deposited on a silicon oxide substrate by PECVD or LPVD deposition techniques [27]. The latter tends to produce lower loss layers, however the high temperatures used ($>$800 degrees Celsius) are hardly CMOS compatible. The nonlinear refractive index of silicon nitride is $2.5 \times 10^{-19} m^2/W$. The optical modes in a silicon nitride waveguide can be well confined as a result of the relatively high refractive index ($\approx$2) of the material such that the nonlinear parameter of a waveguide can be about $1 W^{-1} m^{-1}$ [28]. In the past couple of years a lot of progress has been made in reducing the optical propagation losses in these waveguides. This enables the long interaction lengths, necessary to compensate for the relative low nonlinearity in these waveguides. Indeed ring resonators with Q factors of about a million have been demonstrated [29] as well as low loss ($<$

0.2 dB/cm) waveguides. The absence of nonlinear loss combined with these low losses has lead to the demonstration of several nonlinear optical function in silicon nitride planar waveguides. The most striking example is the generation of a frequency comb spanning from $\approx$ 1200 nm to $\approx$2450 nm generated in a silicon nitride resonator [30]. Additionally an octave spanning supercontinuum was demonstrated in a 4 cm waveguide [31]. However, the power levels needed in all these experiments are relatively high due to the low nonlinear nonlinear response of the silicon nitride.

1.4.2.3 High index doped glass: hydex glass integrated circuits

High index glass circuits based on the commercial glass hydex have a very low linear propagation loss, making long interaction lengths possible. Furthermore the bandgap of the material is high which makes that nonlinear losses are absent in the material. Additionally working at 1550 nm, far from the band gap of the material makes that the material dispersion is relatively low. Similar as in silicon nitride circuits the nonlinear parameter of the waveguides is relatively small $(1/W^{-1}m^{-1})$. In straight waveguide a supercontinuum was obtained [32] spanning from $\approx$ 1200 nm to $\approx$ 1900 nm by pumping them with kw peak power 200 fs long pulses. Very impressive results were obtained in high Q dispersion engineered ring resonator. The high quality factors of these resonators allowed for high optical circulating powers as well as long interaction lengths and optical oscillation was demonstrated [33] in a hydex ring resonator.

1.5 Nonlinear optics in silicon waveguides: main contributions in this work

Silicon has a very high nonlinear refractive index ($n_2 = 6 \times 10^{-18} m^2/W$) [34] as well as a high linear refractive index. In silicon-on-insulator waveguides, where the waveguides have an oxide cladding, the large refractive index contrast enables very high confinement and thus waveguides with a very small modal area. The combination of the large refractive index with the high confinement leads to record values for the real part of the nonlinear parameter of these waveguides of 500 $W^{-1}m^{-1}$ [34] at telecommunication wavelengths. These record values for the nonlinear parameter combined with the CMOS compatible fabrication process make these waveguides very attractive as a nonlinear optical platform. However due to a relatively high two-photon absorption coefficient in the telecommunication band, the imaginary part of the nonlinear parameter of a silicon waveguide is also relatively high: $\approx 80 W^{-1}m^{-1}$ [34]. The high nonlinear absorption has hampered efficient nonlinear optical functions in the telecommunication band enormously. In this work two solutions are proposed to get around this problem.

The first solution is to step away from the telecom wavelength window and use a longer wavelength pump. If the pump photons have sufficiently low energy the two-photon absorption process will be reduced significantly or even be eliminated. To get efficient nonlinear interactions careful dispersion engineering is necessary to phase match the long wavelength pump with the telecom signal (and long wavelength idler) in the nonlinear optical process. In this work dispersion engineered silicon waveguides are used in experiments to demonstrate this principle. As shown in chapter 3, telecom wavelength signals can be amplified by $\approx 13dB$ in a pulsed experiment by using this technique, an improvement of about 10 dB over similar experiments in the telecommunication wavelength window [35]. In another experiment it is shown that an efficient supercontinuum can be generated spanning from the telecom window up to the mid-infrared (see chapter 4) by pumping the waveguides with mid-infrared picosecond pulses. The bandwidth of a supercontinuum generated in similar experiments in the telecom wavelength window were limited to about 300 nm.

The second solution is to use another CMOS compatible material with a high nonlinear refractive index. In this work hydrogenated amorphous silicon waveguides are fabricated and shown to have a nonlinear parameter with a high real part ($770W^{-1}m^{-1}$) and a relatively low imaginary part. In one experiment (see chapter 6), an all-optical broadband amplifier which can amplify telecom signals by using a telecom pump up to 26 dB is demonstrated. This is an improvement of more than 20 dB over similar experiments in crystalline silicon [35]. In another experiment, all-optical sampling of a 320 GBit/s signal with a record efficiency is demonstrated.

Furthermore in this work it is shown that by extensive dispersion engineering it is possible to generate long wavelength light. The most striking example is that by mixing a mid-infrared pump (at 2190 nm) with a telecom signal coherent light at 3635 nm can be generated. The efficient conversion over more than an octave of such a spectral translator in silicon clears the way for a whole new set of potential applications. The translator links the telecom window, where efficient, low power, very sensitive detectors as well as sources exist with the mid-infrared. In the mid-infrared, such sensitive detectors do not exist, nor do efficient sources exist. The spectral translator is able to generate coherent light in the mid-infrared as well as converting signals from the mid-infrared to the telecom band where they can be detected by mature telecom detectors.In another set of experiments a widely tunable mid-infrared silicon based optical parameteric oscillator is demonstrated. The latter shows how the high parametric gain in silicon can be used to construct tunable sources in the mid-infrared

1.5.1 Outline

As discussed above, one way of reducing the detrimental two-photon absorption in crystalline silicon is by stepping away from the telecom wavelength window. Chapter 2 discusses the issues that arise when one wants to develop components which operate in the mid-infrared. Chapter 3 explains how phase matching in the nonlinear four-wave mixing process is achieved between the signal, idler and pump. Parametric amplification of telecom signals as well as the generation of mid-infrared light is discussed. Chapter 4 discusses the process of supectoninuum generation in crystalline silicon. Chapter 5 shows that it is possible to use the high parametric gain in crystalline silicon waveguides to make a tunable source.

Chapter 6 shows that hydrogenated silicon waveguides have lower nonlinear absorption than crystalline silicon waveguides, while having a stronger nonlinear response. An all-optical sampling experiment shows the potential of these waveguides to do nonlinear optical functions in the telecom wavelength window.

Chapter 7 discusses how the nonlinear absorption in crystalline silicon can be lowered by reducing the effective carrier lifetime in the silicon waveguides

References

[1] Gordon E Moore. *Cramming more components onto integrated circuits*. Electronics, 38(8), 1975.

[2] Alvin Leng Sun Loke. *Process integration issues of low-permittivity dielectrics with copper for high-performance interconnects*. PhD thesis, Ghent University, 1999.

[3] Yurii Vlasov and Sharee McNab. *Losses in single-mode silicon-on-insulator strip waveguides and bends.* Optics Express, 12(8):1622–31, April 2004.

[4] Solomon Assefa, Fengnian Xia, and Yurii a Vlasov. *Reinventing germanium avalanche photodetector for nanophotonic on-chip optical interconnects.* Nature, 464(7285):80–4, March 2010.

[5] Qianfan Xu, Bradley Schmidt, Sameer Pradhan, and Michal Lipson. *Micrometre-scale silicon electro-optic modulator.* Nature, 435(7040):325–7, May 2005.

[6] Pieter Dumon. *Ultra-compact Integrated Optical Filters in Silicon-on-insulator by Means of Wafer-Scale Technology*. PhD thesis, Ghent University, 2006.

[7] Y Vlasov. *Silicon integrated nanophotonics: Road from scientific explorations to practical applications*. Proceedings of CLEO/QELS, San Jose, CA, USA, 2012.

[8] Wim Bogaerts, Pieter Dumon, Dries Van Thourhout, Dirk Taillaert, Patrick Jaenen, Johan Wouters, Stephan Beckx, Vincent Wiaux, Roel G Baets, and Senior Member. *Compact Wavelength-Selective Functions in Silicon-on-insulator Photonic Wires*. Selected Topics in Quantum Electronics, IEEE Journal of, 12(6):1394–1401, 2006.

[9] Alexander W Fang, Brian R Koch, Richard Jones, Erica Lively, Di Liang, Ying-hao Kuo, and John E Bowers. *A Distributed Feedback Evanescent Laser*. IEEE Photonics Technology Letters, 20(20):1667–1669, 2008.

[10] G Roelkens, D Van Thourhout, R Baets, R Nötzel, and M Smit. *Laser emission and photodetection in an InP/InGaAsP layer integrated on and coupled to a Silicon-on-Insulator waveguide circuit.* Optics Express, 14(18):8154–9, September 2006.

[11] Rodolfo E Camacho-Aguilera, Yan Cai, Neil Patel, Jonathan T Bessette, Marco Romagnoli, Lionel C Kimerling, and Jurgen Michel. *An electrically pumped germanium laser.* Optics Express, 20(10):11316–20, May 2012.

[12] Katrien De Vos, Irene Bartolozzi, Etienne Schacht, Peter Bienstman, and Roel Baets. *Silicon-on-Insulator microring resonator for sensitive and label-free biosensing.* Optics Express, 15(12):7610–5, June 2007.

[13] Jacob T Robinson, Long Chen, and Michal Lipson. *On-chip gas detection in silicon optical microcavities.* Optics Express, 16(6):4296–301, March 2008.

[14] Richard Soref. *Mid-infrared photonics in silicon and germanium*. Nature Photonics, 4(8):495–497, August 2010.

[15] *www.daylightsolutions.com*.

[16] R. M. Osgood, Jr., N. C. Panoiu, J. I. Dadap, Xiaoping Liu, Xiaogang Chen, I-Wei Hsieh, E. Dulkeith, W. M. Green, and Y. a. Vlasov. *Engineering nonlinearities in nanoscale optical systems: physics and applications in dispersion-engineered silicon nanophotonic wires*. Advances in Optics and Photonics, 1(1):162, January 2009.

[17] L Fu, M Rochette, V Ta'eed, D Moss, and B Eggleton. *Investigation of self-phase modulation based optical regeneration in single mode As2Se3 chalcogenide glass fiber*. Optics Express, 13(19):7637–7644, 2005.

[18] Naoki Sugimoto, Tatsuo Nagashima, Tomoharu Hasegawa, and S Ohara. *Bismuth-based optical fiber with nonlinear coefficient of 1360 W/sup-1/km/sup-1*. In Optical Fiber Communication Conference, 2004. OFC 2004, volume 2, pages 3–pp. IEEE, 2004.

[19] NGR Broderick, TM Monro, PJ Bennett, and DJ Richardson. *Nonlinearity in holey optical fibers: measurement and future opportunities*. Optics Letters, 24(20):1395–1397, 1999.

[20] Benjamin J Eggleton, Barry Luther-Davies, and Kathleen Richardson. *Chalcogenide photonics*. Nature Photonics, 5(3):141–148, 2011.

[21] Michael RE Lamont, Barry Luther-Davies, Duk-Yong Choi, Steve Madden, Benjamin J Eggleton, et al. *Supercontinuum generation in dispersion engineered highly nonlinear (y= 10/W/m) As2S3 chalcogenide planar waveguide*. Made available in DSpace on 2010-12-20T06: 05: 52Z (GMT). No. of bitstreams: 1 Lamont_Supercontinuum2008. pdf: 435052 bytes, checksum: 6f0cba3ba13997548025c6c2c756e5dd (MD5) Previous issue date: 2009-06-03T06: 09: 46Z, 2009.

[22] Mark D Pelusi, Vahid G Ta'eed, Libin Fu, Eric Magi, Michael RE Lamont, Steve Madden, Duk-Yong Choi, Douglas AP Bulla, Barry Luther-Davies, and Benjamin J Eggleton. *Applications of highly-nonlinear chalcogenide*

glass devices tailored for high-speed all-optical signal processing. Selected Topics in Quantum Electronics, IEEE Journal of, 14(3):529–539, 2008.

[23] Vahid G Ta'eed, Mehrdad Shokooh-Saremi, Libin Fu, Ian CM Littler, David J Moss, Martin Rochette, Benjamin J Eggleton, Yinlan Ruan, and Barry Luther-Davies. *Self-phase modulation-based integrated optical regeneration in chalcogenide waveguides*. Selected Topics in Quantum Electronics, IEEE Journal of, 12(3):360–370, 2006.

[24] TD Vo, Hao Hu, Michael Galili, Evarist Palushani, Jing Xu, Leif Katsuo Oxenløwe, SJ Madden, D-Y Choi, DAP Bulla, MD Pelusi, et al. *Photonic chip based transmitter optimization and receiver demultiplexing of a 1.28 Tbit/s OTDM signal*. Optics Express, 18(16):17252–17261, 2010.

[25] Michael RE Lamont, Barry Luther-Davies, Duk-Yong Choi, Steve Madden, Xin Gai, Benjamin J Eggleton, et al. *ANU-Digital Collections: Net-gain from a parametric amplifier on a chalcogenide optical chip*. Made available in DSpace on 2010-12-20T06: 02: 33Z (GMT). No. of bitstreams: 1 Lamont_Net2008. pdf: 1931396 bytes, checksum: 51c5b50c05018f732c9a07119f8521ad (MD5) Previous issue date: 2009-06-04T04: 01: 55Z, 2009.

[26] Ananth Subramanian, Shankar Selvaraja, Peter Verheyen, Ashim Dhakal, Katarzyna Komorowska, and Roel Baets. *Near-infrared grating couplers for silicon nitride photonic wires*. 2012.

[27] Jeffrey A Babcock, Scott G Balster, Angelo Pinto, Christoph Dirnecker, Philipp Steinmann, Reiner Jumpertz, and Badih El-Kareh. *Analog characteristics of metal-insulator-metal capacitors using PECVD nitride dielectrics*. Electron Device Letters, IEEE, 22(5):230–232, 2001.

[28] DTH Tan, K Ikeda, PC Sun, and Y Fainman. *Group velocity dispersion and self phase modulation in silicon nitride waveguides*. Applied Physics Letters, 96(6):061101–061101, 2010.

[29] Alexander Gondarenko, Jacob S Levy, and Michal Lipson. *High confinement micron-scale silicon nitride high Q ring resonator.* Optics Express, 17(14):11366–70, July 2009.

[30] Yoshitomo Okawachi, Kasturi Saha, Jacob S Levy, Y Henry Wen, Michal Lipson, and Alexander L Gaeta. *Octave-spanning frequency comb generation in a silicon nitride chip*. Optics Letters, 36(17):3398–3400, 2011.

[31] Robert Halir, Yoshitomo Okawachi, Jacob S Levy, Mark A Foster, Michal Lipson, and Alexander L Gaeta. *Octave-spanning supercontinuum generation in CMOS-compatible silicon nitride waveguides*. In CLEO: Applications and Technology. Optical Society of America, 2011.

[32] David Duchesne, Marco Peccianti, Michael R E Lamont, Marcello Ferrera, Francois Légaré, Roberto Morandotti, Sai Chu, Brent E Little, and J Moss. *Supercontinuum generation in a high index doped silica glass spiral waveguide*. Optics Express, 18(2):391–393, 2010.

[33] Marcello Ferrera, David Duchesne, L Razzari, Marco Peccianti, Roberto Morandotti, Alessia Pasquazi, Yong-woo Park, Jose Azan, Brent E Little, Sai T Chu, and David J Moss. *Advanced Integrated Photonics in Doped Silica Glass*. 2012.

[34] R. M. Osgood, Jr., N. C. Panoiu, J. I. Dadap, Xiaoping Liu, Xiaogang Chen, I-Wei Hsieh, E. Dulkeith, W. M. Green, and Y. a. Vlasov. *Engineering nonlinearities in nanoscale optical systems: physics and applications in dispersion-engineered silicon nanophotonic wires*. Advances in Optics and Photonics, 1(1):162, January 2009.

[35] Mark a Foster, Amy C Turner, Jay E Sharping, Bradley S Schmidt, Michal Lipson, and Alexander L Gaeta. *Broad-band optical parametric gain on a silicon photonic chip.* Nature, 441(7096):960–3, June 2006.

2

Silicon waveguides beyond the telecom window

When one moves to longer wavelengths, new problems such as absorption in the cladding materials as well as substrate leakage arise. Furthermore new components such as grating couplers and ring resonators need to be designed. This chapter briefly describes the properties of silicon photonic circuits which operate outside the telecom window.

2.1 Introduction

Silicon is transparent from 1.1 μm up to 8 μm, while silicon oxide is transparent up to ≈ 4 μm [1] as shown in figure 2.1. As a result, the silicon-on-insulator platform can be used to integrate optical circuits from 1.1 μm up to 4.0 μm. Although most research is focused on the development of circuits in the telecom window, recently researchers have started to focus on the development of circuits for longer wavelengths. Their main rationale being the development of circuits for the mid-infrared fingerprint region, see section 1.1.2.2, which would have the potential to increase the sensitivity of current sensors several orders of magnitude.

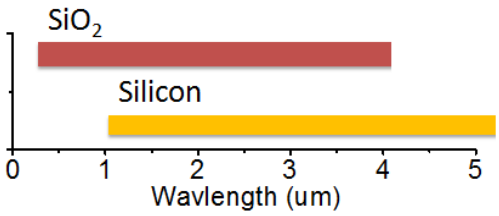

Figure 2.1: The transparency of silicon oxide and silicon as a function of wavelength.

2.2 Optical loss of silicon waveguides at longer wavelengths

A photonic component designed for 1550 nm can work at longer wavelengths when all its dimensions are linearly scaled with the wavelength. The processing of the silicon-on-insulator chips in this work is done in the cleanroom of imec. These processes are more or less standardized, such that it is not possible to change all the dimensions of a component, which are optimized for the telecommunication window. More specifically the height of a waveguide is fixed at 220 nm, while the oxide buffer layer is a fixed at 2 μm. For a standard waveguide operating around 1550 nm, which is typically 450 nm wide, this does not result in any substrate leakage. However, when a (wider) waveguide with the same thickness is designed to work at longer wavelengths the mode will be less confined and leak to the substrate. The substrate leakage has been simulated for a 900 nm wide waveguide with an air cladding and is shown in figure 2.2. The figure shows that the 900 nm wide waveguide can be used up to a wavelength of about 2900 nm, without having too much substrate leakage. When we want to work at longer wavelengths, we need thicker waveguides. In a dedicated run in the cleanroom of imec, waveguides with a thickness of 400 nm were processed. The substrate leakage for a waveguide with a thickness of 400 nm and a width of 1300 nm and 1500 nm is shown in figure 2.3. The substrate leakage is very low up to 4 μm. The substrate leakage was simulated with CAMFR as in [2].

Another problem is the optical absorption loss of the oxide cladding of the waveguides. In several situations it is advantageous to clad the waveguides with an oxide cladding for protection from the environment, but also when an electrical connection to drive optical modulators and or lasers has to come on top of the optical circuit. The deposited oxide through plasma enhanced chemical vapor deposition is not very pure and has several absorption peaks at longer wavelengths. For example, figure 2.4 shows the measured optical propagation loss of an oxide clad waveguide obtained by using a cut-back measurement on a set of 0.35 cm, 0.88 cm, 1.74 cm, and 3.31 cm long waveguides. Due to the absorption in the

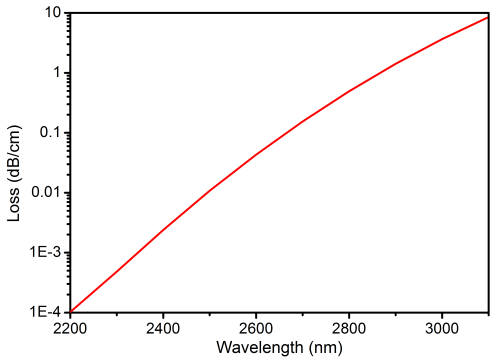

Figure 2.2: The substrate leakage for a 220 nm high and 900 nm wide waveguide.

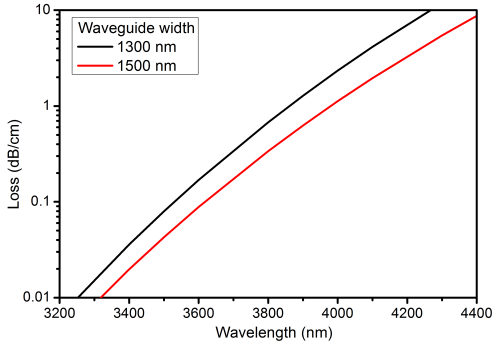

Figure 2.3: The substrate leakage for a 400 nm high and 1300 nm wide waveguide as well as a 1500 nm wide waveguide.

oxide cladding the waveguide loss is high in a band around 2250 nm.

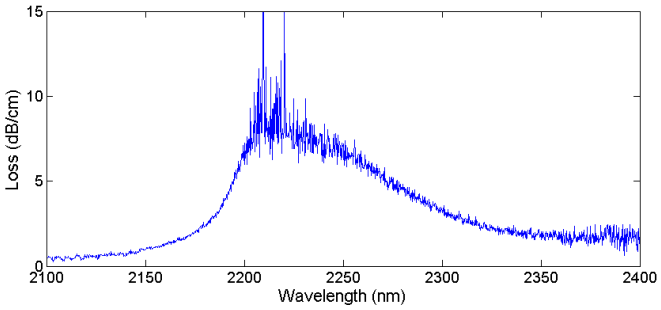

Figure 2.4: The propagation loss of a silicon waveguide with an oxide top cladding.

2.3 Coupling in and out silicon waveguides

The coupling in and out of a silicon chip can be done with grating couplers [3], or by using lensed fibers or a lens to couple the light through a cleaved facet of a silicon waveguide. As long as one wants to work at wavelengths shorter than 2500 nm it is possible to use standard SMF-28. The loss of a standard SMF-28 fiber is shown in figure 2.5 and the losses in the shown range are relatively low. However when longer wavelengths are used, the light needs to be coupled in free space, or with specialty fiber [4].

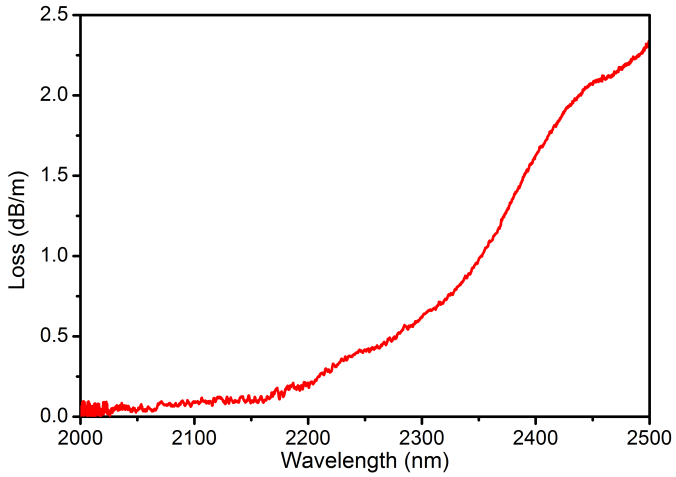

Figure 2.5: The propagation loss of a standard single mode fiber as a function of wavelength

2.3.1 Grating couplers

This section summarizes the results obtained in "Highly efficient broadband silicon-on-insulator grating couplers for the short wave infrared wavelength range" [5]. A grating as shown in figure 2.6 was designed. The grating coupler enables efficient coupling to a cleaved single mode fiber. The fabricated grating is shown in figure 2.7. The coupling efficiency with a SMF-28 fiber was found to be -5.2 dB at 2150 nm, while the 3 dB bandwidth was 160 nm.

2.3.2 Coupling through a cleaved facet of a silicon waveguide

Another method of coupling light in a photonic chip is by using edge coupling. A silicon chip is cleaved through a waveguide. From the side light is coupled in the waveguide with a lensed fiber. A lensed fiber can focus light on a tight Gaussian

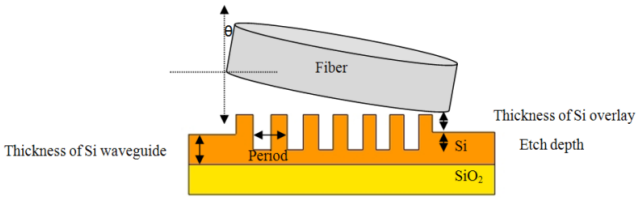

Figure 2.6: A schematic the designed grating coupler.

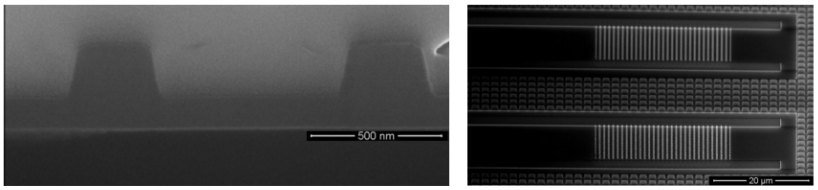

(a) (b)

Figure 2.7: A scanning electron microscope image of the fabricated grating coupler.

spot of approximately 2.5 μm in diameter. The coupling efficiency to a waveguide of 220 nm high and a varying width with an air cladding is shown in figure 2.8. The coupling efficiency to the fundamental optical mode is simulated in Fimmwave ©. As shown in the figure the best coupling is achieved for waveguides with a width of about 3 μm. In the experiments however it is found that the coupling efficiency is worse than the value found in the simulation: it is about -7 dB per facet [6]. Another method is to use inverted tapers and a polymer overlay [7]. In this work, this approach was explored by using a nitride overlay in stead of a polymer overlay, however the absorption of the deposited nitride is too high at wavelengths beyond 2000 nm to be useful in an experiment.

2.4 Long-wavelength silicon photonic components

This section summarizes very briefly some components fabricated for the wavelength range 2000 nm - 2500 nm. The left panel of figure 2.9 shows the propagation loss of a 900 nm wide silicon-on-insulator waveguide with a height of 220 nm and an air cladding. The propagation loss can be as low as 0.6 dB/cm. The right panel shows the transmission spectrum of a ring resonator notch filter. The Q factors of the ring can be as high as 100000. More information can be found in [8].

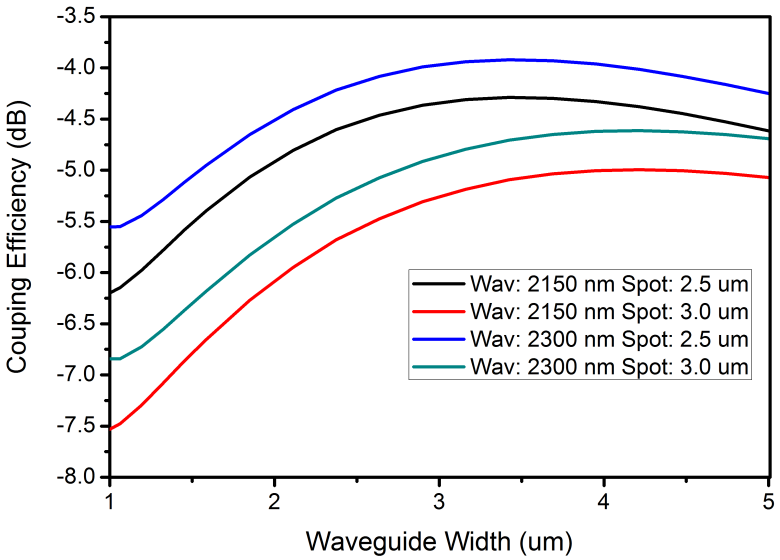

Figure 2.8: The simulated coupling efficiency of a lensed fiber to the fundamental mode of a waveguide. The coupling efficiency is calculated for two wavelengths: 2150 nm and 2300 nm. It is assumed that the spot produced by the lensed fiber is a Gaussian beam with a diameter between 2.5 μm and 3 μm.

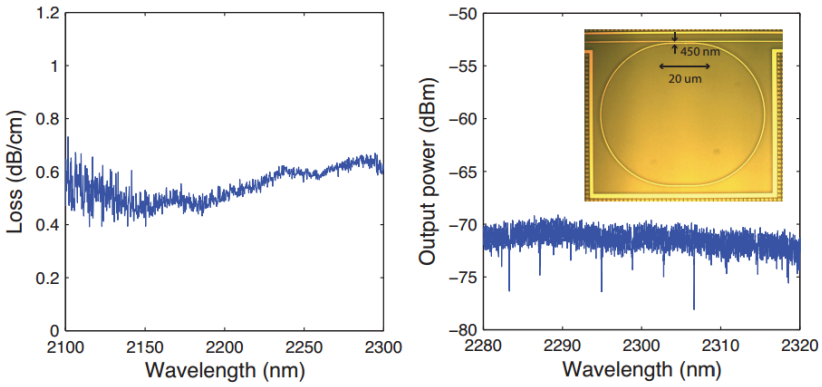

Figure 2.9: The propagation loss of a 900 nm wide waveguide and the transmission spectrum of a ring resonator with a radius of 50 μm.

2.5 Conclusion

In this chapter the linear properties of some silicon photonic components were discussed. It is shown that the technology designed for the telecommunication

window can be extended to longer wavelengths. Although some issues such as absorption in the oxide cladding and substrate leakage can be a problem.

2.6 Highly Efficient Broadband Silicon-on-Insulator Grating Couplers for the Short Wave Infrared Wavelength Range

The content of this section was published in the proceedings of the IPR conference 2011 [5]

Over the last decade the silicon-on-insulator platform has become the leading platform for integrated photonics. The progress was mainly driven by applications for telecom, since silicon is transparent at telecommunication wavelengths. It has lead to a whole range of integrated photonics devices for telecom applications such as arrayed waveguide gratings, planar concave gratings and sharp add/drop filters [9]. However, the platform is transparent up to 3.5 m, limited by the absorption of the oxide buffer layer [1] and has recently been proposed as a platform for these longer wavelengths. This region is of enormous interest for spectroscopic applications, since many molecules have distinct absorption bands in this region. Moreover, this wavelength range will not only enable a whole set of new optical sensing components, but it has also shown to be of great interest in a nonlinear optics context. Working at these longer wavelengths reduces the parasitic nonlinear absorption in silicon, the two photon absorption, enormously. Without the two photon absorption we can fully benefit from the record nonlinear parameters obtained through the combination of the high linear index leading to high confinement and the high nonlinear index of silicon. Indeed recent demonstrations have shown highly efficient nonlinear optical devices enabling high parametric gain , wavelength conversion and efficient supercontinuum generation. However, interfacing with chips containing these new mid-infrared devices has been very limited so far, as it is mostly achieved by coupling lensed fibers directly to the waveguides. Low coupling efficiencies of around -10dB are achieved as a result of the bad overlap between the spot of these lensed fibers and the waveguide mode. In this paper we propose diffractive grating couplers optimized for this new wavelength region. We achieve coupling losses as low as -5.2 dB and a 3 dB bandwith of 160 nm. The central wavelength of the grating couplers is 2150 nm, a wavelength at the edge of the two-photon absorption cut-off wavelength and well covering the finger print absorption bands of many molecules (e.g. glucose). The Bragg condition describes the relation of the incident and diffracted waves as shown in equation:

$$k_z = \beta - \tag{2.1}$$

where $\beta = \frac{2\pi}{\lambda} n_e f f$ is the propagation constant of the guided mode and $= \frac{2\pi}{\Lambda}$,

with Λ the period of the grating. $k_z = \frac{2\pi}{\lambda} sin(\theta)$ is the projected diffracted wave vector, with ? the angle of the phase fronts of the diffracted field with respect to the silicon surface (and hence the angle of the optical fiber with respect to the surface normal for optimal fiber coupling). From the Bragg condition, the period of the grating coupler is calculated for a given peak wavelength. However, the coupling efficiency depends mostly on the directionality which is a function of waveguide thickness; etch depth and thickness of the silicon overlay. The coupling efficiency also depends on the matching of the coupling strength of the grating coupler and the fiber mode. A schematic cross-section of the grating coupler is shown in Fig. 2.10.

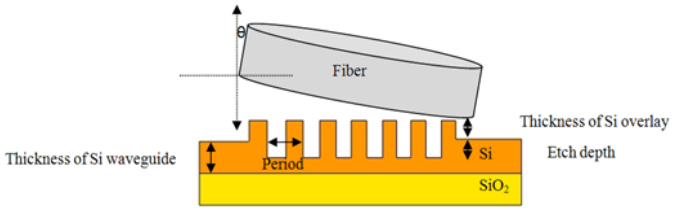

Figure 2.10: Schematic cross-section of the fiber-chip grating coupler interface

In the simulation, a 15 degree angle of the fiber is used to avoid 2nd order reflection back into the waveguide. The etch depth is fixed at 70 nm, the thickness of the Si overlay is 160 nm and the thickness of Si waveguide is 220 nm. The period corresponding to a peak in the coupling efficiency at a wavelength of 2.15 m is 1.025 m. The simulation itself is done in 2D using CAMFR, a full-vectorial solver based on eigen mode expansion. The simulated coupling efficiency is shown in Figure 2.11(a). It shows a maximum coupling efficiency around -3.2dB and a 3 dB bandwidth of 200 nm. Figure 2.11 (b) shows an electric field plot obtained by simulation in Camfr (for TE polarized light at x nm).

The fabrication of the highly efficient grating couplers is done in the 200 mm CMOS pilot line at imec with 193nm DUV lithography. On top of a 200 mm SOI wafer consisting of a 220 nm thick crystalline silicon layer on top of a 2 μm thick buried oxide layer, 160 nm of poly-crystalline silicon is deposited. To form the slits of the grating coupler, this stack is etched through the top poly-silicon layer and 70 nm through the crystalline silicon layer. Except at the location of the grating couplers the poly-silicon layer is removed with a chlorine/fluorine-based and bromine-based chemistry. We designed grating couplers with a period of 1.050 μm to obtain a peak coupling efficiency around 2.15 μm. The fabricated couplers are shown in Figure 2.12. The grating duty cycle is 35%. To determine the coupling efficiency, the fiber-to-fiber insertion loss of two grating couplers was measured. These grating couplers were connected by a low-loss waveguide of 300 μm long and 12 μm wide. We have characterized the gratings using standard single

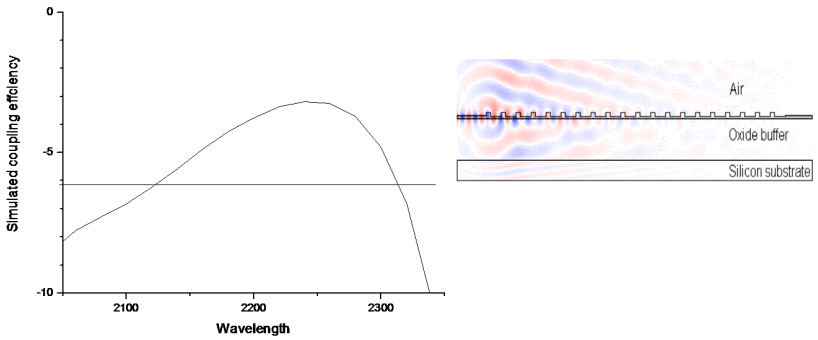

Figure 2.11: (a) Simulated coupling efficiency of the grating coupler. (b) Simulated field plot obtained from Camfr.

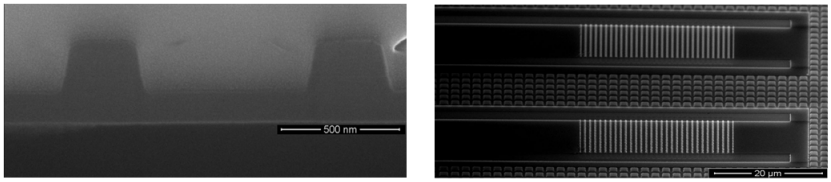

Figure 2.12: (a) A cross-section of the grating (left) and (b) a bird eye top view of the fabricated raised grating (right)

mode fibers under an angle of 15 degrees. The results are shown in figure 2.13. The small reflections at the grating couplers cause Fabry-Perot fringes which can be seen, especially for the longer wavelengths, since we come closer to vertical diffraction, which induces a second order back reflection. The maximum coupling efficiency is found to be -5.2 dB and the 3dB bandwidth is 160 nm. The lower than expected efficiency is believed to be a result of the lateral size of the grating. The grating is 12 μm wide, which makes the overlap with the fiber suboptimal. The mode diameter in the fiber is calculated to be 13.6 μm, which causes an extra loss of 1.5 dB compared to the optimal situation of where a 20 μm wide grating coupler is used.

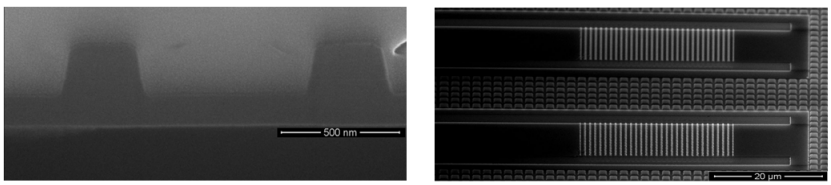

Figure 2.13: The fiber-chip coupling efficiency as a function of wavelength

We have demonstrated for the first time efficient grating couplers for the short-wave infrared wavelength range. A coupling efficiency of -5.2 dB was obtained with a 160 nm 3dB bandwidth. The gratings open the path to new silicon photonic chips for the mid-infrared enabling new nonlinear optical functions as well as new spectroscopic lab on-a-chip approaches. Further optimalization to improve the efficiency further will be discussed at the conference.

References

[1] Richard Soref. *Mid-infrared photonics in silicon and germanium*. Nature Photonics, 4(8):495–497, August 2010.

[2] P. Bienstman, S. Selleri, L. Rosa, H. P. Uranus, W. C. L. Hopman, R. Costa, a. Melloni, L. C. Andreani, J. P. Hugonin, P. Lalanne, D. Pinto, S. S. a. Obayya, M. Dems, and K. Panajotov. *Modelling leaky photonic wires: A mode solver comparison*. Optical and Quantum Electronics, 38(9-11):731–759, January 2007.

[3] Dirk Taillaert, Peter Bienstman, and Roel Baets. *Compact efficient broadband grating coupler for silicon-on-insulator waveguides.* Optics Letters, 29(23):2749–51, December 2004.

[4] Zhenzhou Cheng, Xia Chen, C Y Wong, Ke Xu, Christy K Y Fung, Y M Chen, and Hon Ki Tsang. *Mid-infrared grating couplers for silicon-on-sapphire waveguides*. Photonics Journal, IEEE, 4(1):104–113, 2012.

[5] Bart Kuyken, Nannicha Hattasan, Diedrik Vermeulen, Shankar K. Selvaraja, Wim Bogaerts, William Green, Roel Baets, and Gunther Roelkens. *Highly Efficient Broadband Silicon-on-Insulator Grating Couplers for the Short Wave Infrared Wavelength Range*. Advanced Photonics, page IMB6, 2011.

[6] Bart Kuyken, Xiaoping Liu, Richard M Osgood, Roel Baets, Günther Roelkens, and William M J Green. *A silicon-based widely tunable short-wave infrared optical parametric oscillator.* Optics Express, 21(5):5931–40, March 2013.

[7] Minhao Pu, Liu Liu, Haiyan Ou, Kresten Yvind, and Jørn M. Hvam. *Ultra-low-loss inverted taper coupler for silicon-on-insulator ridge waveguide*. Optics Communications, 283(19):3678–3682, October 2010.

[8] F Leo, B Kuyken, N Hattasan, R Baets, and G Roelkens. *Passive SOI devices for the Short-wave-infrared*. 2012.

[9] W. Bogaerts, V. Wiaux, D. Taillaert, S. Beckx, B. Luyssaert, P. Bienstman, and R. Baets. *Fabrication of photonic crystals in silicon-on-insulator using 248-nm deep UV lithography*. IEEE Journal of Selected Topics in Quantum Electronics, 8(4):928–934, July 2002.

3

Optical Parametric Amplification

By using the nonlinear four-wave-mixing process, a strong pump beam can amplify a weak signal beam while at the same time generate a converted idler signal in a nonlinear medium. The amplification is called parametric amplification, no energy is transferred to the medium itself. The nonlinear process is phase sensitive, which means that the phase relation between the waves traveling throughout the medium has to be conserved: the interaction between the waves can only be efficient when the waves are phase matched. This chapter demonstrates how phase matching of signals with very different optical frequencies can be achieved in a silicon waveguide to obtain efficient amplification and conversion of these signals.

3.1 Introduction

Section A shows that phase matching in the degenerate four wave mixing process is achieved when

$$\kappa = \Delta k + 2\gamma P = 0 \tag{3.1}$$

Here, P is the power of the pump, γ the nonlinear parameter of the waveguide, while Δk (the linear phase mismatch) is given by

$$\Delta k = [n_i\omega_i + n_s\omega_s - 2n_p\omega_p]/c = \beta_i + \beta_s - 2\beta_p \tag{3.2}$$

where n_i, n_s, n_p and $\beta_i, \beta_s, \beta_p$ are the refractive index and the propagation constant of the idler, signal and pump wavelength respectively. To get a grip on the

phase matching equation, it is useful to use a Taylor expansion of the propagation constant in the vicinity of the pump frequency.

$$\beta(\omega_p + \Delta\omega) = \beta_p + \beta_1\Delta\omega + \frac{\beta_2\Delta\omega^2}{2} + \frac{\beta_3\Delta\omega^3}{6} + \frac{\beta_4\Delta\omega^4}{24} \tag{3.3}$$

Here β_p is the propagation constant at the pump wavelength and $\beta_1, \beta_2, \beta_3, \beta_4$ are the first, second, third and fourth order of dispersion at the pump wavelength respectively. These are given by

$$\beta_n = \frac{d^n\beta}{dw^n}(\omega = \omega_p) \tag{3.4}$$

When the idler and signal frequencies are separated by $\Delta\omega$ from the pump frequency: $\omega_i = \omega_p - \Delta\omega$ and $\omega_s = \omega_p + \Delta\omega$, β_p and β_i are given by:

$$\beta(\omega_i) = \beta(\omega_p) - \beta_1\Delta\omega + \frac{\beta_2\Delta\omega^2}{2} - \frac{\beta_3\Delta\omega^3}{6} + \frac{\beta_4\Delta\omega^4}{24} \tag{3.5}$$

$$\beta(\omega_s) = \beta(\omega_p) + \beta_1\Delta\omega + \frac{\beta_2\Delta\omega^2}{2} + \frac{\beta_3\Delta\omega^3}{6} + \frac{\beta_4\Delta\omega^4}{24} \tag{3.6}$$

Which leads to a phase mismatch

$$\kappa = \Delta k + 2\gamma P = \beta_2\Delta\omega^2 + \frac{\beta_4\Delta\omega^4}{12} + 2\gamma P \tag{3.7}$$

Achieving perfect phase matching is possible when $\kappa = 0$ or when

$$-(\beta_2\Delta\omega^2 + \frac{\beta_4\Delta\omega^4}{12}) = 2\gamma P \tag{3.8}$$

The equation has several solutions depending on the sign of β_2 and β_4. This is graphically shown in figure 3.1 for the four possible combinations. In the following sections, waveguides with specific signs for the second and fourth order dispersion coefficients to get broadband amplification (section 3.2) as well as for amplification and conversion of signals with a very different wavelength as compared to pump wavelength (section 3.3.2.1 and 3.3.3) are discussed.

3.1.1 Alternative approach to the phase matching equation

Starting from

$$\beta_i + \beta_s - 2\beta_p + 2\gamma P = 0 \tag{3.9}$$

We can rearrange the equation as follows:

$$\frac{\beta_i + \beta_s}{2} = \beta_p - \gamma P \tag{3.10}$$

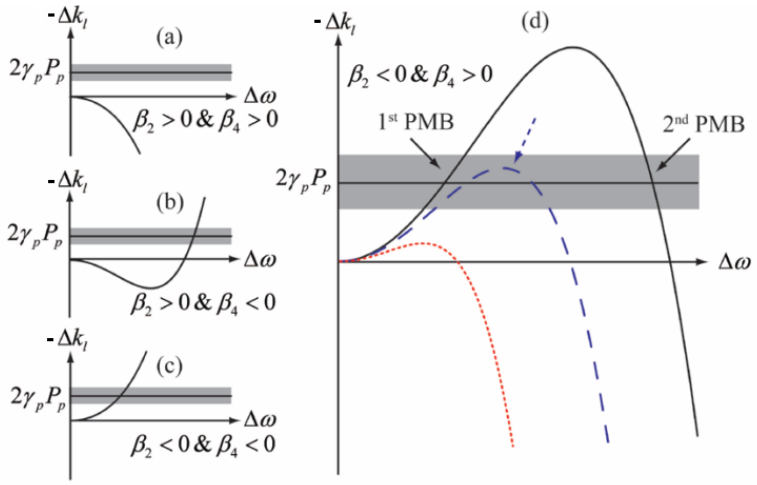

Figure 3.1: The phase mismatch as a function of detuning frequency. Depending on the sign of β_2 and β_4 the phase matching equations has several solutions. a) $\beta_2 > 0$ and $\beta_4 > 0$, b) $\beta_2 > 0$ and $\beta_4 < 0$, c) $\beta_2 < 0$ and $\beta_4 < 0$, d) $\beta_2 < 0$ and $\beta_4 > 0$

This equation shows that the average of the propagation constants at the idler and signal frequency has to be slightly smaller than the propagation constant at the pump frequency to get phase matching in the degenerated four-wave-mixing process. In the following sections this approach will be used as well.

3.2 Optical parametric amplification in the vicinity of the pump

3.2.1 Introduction

When broadband phase matching in the vicinity of the pump wavelength is needed, (see appendix A) it is necessary that for a wide frequency detuning: $-4\gamma P < \Delta k < 0$. Within this detuning range, a signal will experience gain. In the vicinity of the pump the Taylor expansion of the dispersion can be limited to a second order polynomial. Which means that in order to have gain: $-4 < \beta_2 \Delta\omega^2 < 0$, such that the second order dispersion in the waveguide has to be small and anomalous ($\beta_2 < 0$). This result can also be understood with the reasoning of section 3.1.1. In figure 3.2 the propagation constant as a function of optical frequency is plotted for a waveguide with anomalous dispersion at the pump frequency. The idler, signal and pump frequency are shown in the figure. The average of the propagation constant at idler and signal frequency is given by the intersection of the red line with the line $\omega = \omega_p$. When the average propagation constant is γP smaller

than the propagation constant at the pump frequency phase matching is achieved. This can only be satisfied when the curvature of the function $\beta(\omega)$ is negative at the pump frequency. This means that the second derivative of the propagation constant with respect to the frequency at the pump, β_2 has to be negative. The group velocity dispersion has to be anomalous.

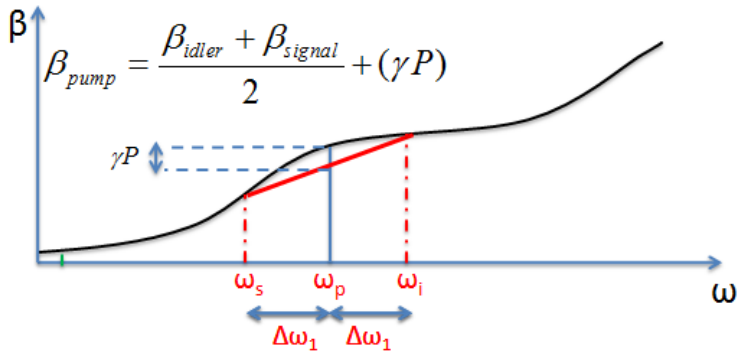

Figure 3.2: Phase matching in the vicinity of the pump. The figure shows a phase matched pump, idler and signal.

3.2.2 Modulation Instability

When a pump, signal and idler wave are phase matched in a nonlinear waveguide, a signal can get amplified efficiently. However, even in the absence of a probe signal which needs to be amplified, a strong pump can amplify the background noise (coming from the pump, vacuum fluctuations, etc...) present in the system. This process is called modulation instability. The amplification of noise in bands which are phase matched in the nonlinear process leads to strong sidebands in the spectrum of a pump after traveling through a waveguide. In the time domain, this means that the optical signal gets modulated. An example is shown in figure 3.3: the autocorrelation trace and the output spectrum of a high power 100 ps pulse are shown after traveling through an optical fiber.

3.2.3 A broadband mid infrared optical parametric amplifier

This section discusses the most important results obtained in “50 dB parametric on-chip gain in silicon photonic wires” [2]

3.2.3.1 Group velocity dispersion in a 900 nm wide silicon waveguide

The group velocity dispersion of a 900 nm wide silicon waveguide with an air cladding is shown in figure 3.4. The dispersion of the waveguide is anomalous and

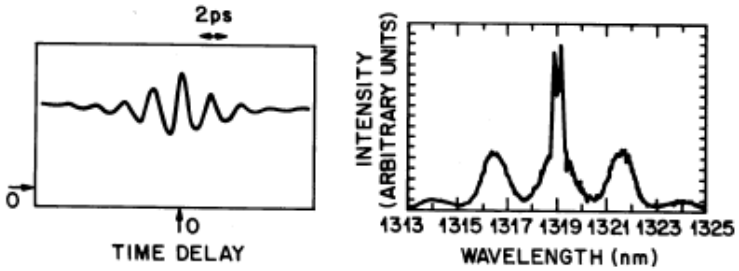

Figure 3.3: Modulation instability in an optical fiber. The figure shows the output spectrum of the pulse (right) when a 100 ps pulse with a peak power of 7.2 W has traveled through a fiber. The left panel shows the autocorrelation trace of the 100 ps pulse at the output. Figure from [1]

low in a region between 1800 nm and 2400 nm. This makes the waveguide a good candidate for doing experiments on all optical parametric amplification.

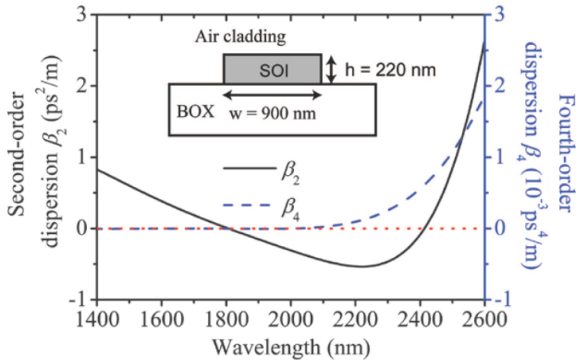

Figure 3.4: The group velocity dispersion and the fourth order dispersion as a function of wavelength.

3.2.3.2 Experimental Results

A set of 900 nm wide waveguides with different lengths (1, 2 and 3 cm) were fabricated in the 200 mm pilot line at imec. Figure 3.5 shows a picture of such a waveguide which is wrapped in a spiral to reduce its footprint. By doing a cutback measurement, the propagation loss as well as the insertion loss is measured as a function of wavelength. Broadband light, the amplified spontaneous emission of a mid-infrared CW laser (IPG photonics SFTL Cr^2:ZnSe polycrystal with erbium-fiber laser pump source) is coupled in and out of the chip with lensed fibers. The polarization is controlled by a polarization controller such that only the quasi TE

mode of the waveguide is excited. The measured propagation loss is shown in figure 3.6.

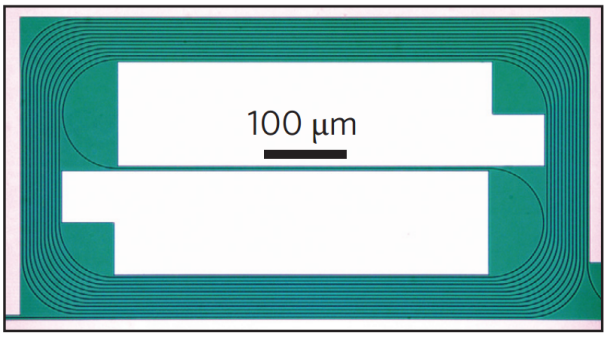

Figure 3.5: A microscope image showing a 2 cm long spiral wrapped in a tight spiral to obtain a small footprint.

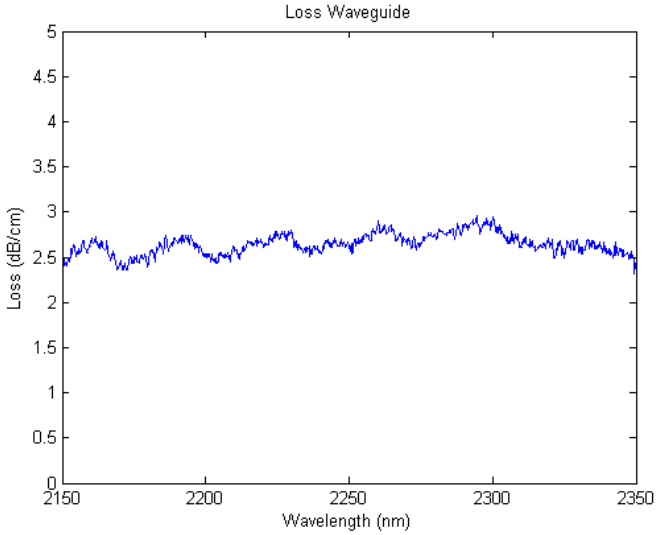

Figure 3.6: The propagation loss in a 900 nm wide silicon waveguide. The loss is found to be around 2.5 dB/cm.

In a next experiment, high peak power 2 ps long pulses are coupled into the chip. This picosecond pulse train (repetition rate 76 MHz) is derived from a tunable optical parametric oscillator (mode-locked Ti:sapphire-pumped Coherent Mira-OPO) which is coupled to a fiber. The pulses are coupled in and out of the chip using lensed fibers, the polarization of the pulses is controlled by a polar-

ization controller such that only the quasi TE mode of the waveguide is excited. The output spectrum is shown in figure 3.7. Panel b) shows the output spectrum of these pulses for several peak power levels. At all peak power levels the broadband amplification of background noise, the so called modulation instability can be seen. The amplification of background noise by the Raman effect can be seen as well. For low peak power pulses, phase matching is achieved in a broad band close to the pump wavelength (labeled broadband MI) as well as in a band spectrally further from the pump (labeled discrete band MI). At a higher peak pump power these bands merge. This can be understood by looking at figure 3.1 d). The second order dispersion in the waveguide is positive, while the fourth order dispersion coefficient is negative (see [2]). This leads to two solutions in detuning frequency where phase matching is achieved as well as a band around these points where the phase mismatch is small and thus amplification is obtained. However, when the peak power of the pump pulses is increased, these bands merge in one broad band as shown in figure 3.1 d).

In a next experiment, the high peak power pulses are combined with a small cw signal in a 90/10 coupler, polarization controllers make sure that both the pulses and the cw signal excite the quasi TE mode of the waveguide. The pump pulses are centered at 2173 nm and the coupled peak power of the pulses is 13.5 W. The wavelength of the cw laser is tuned in steps of $\approx$ 20 nm and the output spectrum is recorded. These output spectra can be seen in figure 3.8. The amplification and conversion can be calculated from these spectra, similar as in [3]: the output spectrum around the laser tone is numerically integrated. By taking in account the duty cycle of the pulses and the cw laser power at the input, the amplification can be calculated. A similar procedure is used to calculate the conversion efficiency. The result is shown in figure 3.8 b).

3.3 Phase matching of signals in a discrete band at a large detuning from the pump wavelength

This section briefly discusses the results of [4]

3.3.1 Introduction

It is possible to shift the second point of detuning in figure 3.1 d) where phase matching occurs to a larger detuning value. This can be achieved in the same 900 nm wide waveguide by tuning the pump wavelength. The location of the second phase matching point is dependent on the higher order dispersion coefficients and these coefficients are dependent on the pump wavelength.

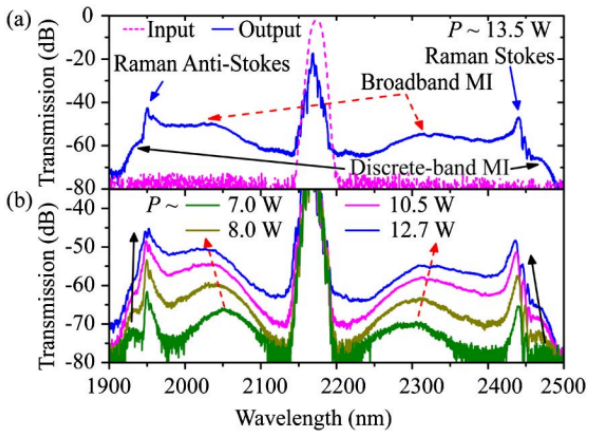

Figure 3.7: The output spectrum of the pulses after traveling through the waveguide. The dispersion in the waveguide enables broadband phase matching such that high peak power pulses will amplify background radiation noise. This so called process of modulation instability is shown in the figure.

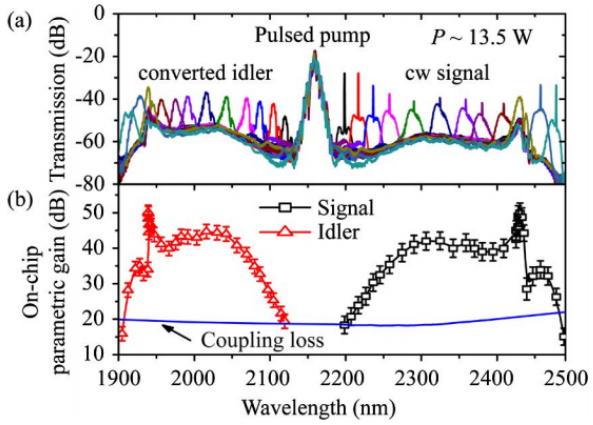

Figure 3.8: a) The output spectrum of the pulses and the amplified cw signal. b) The measured amplification of the pulses as a function of the wavelength.

3.3.2 Pump wavelength dependent phase matched signal and idler frequencies

To find a set of phase matched signal and idler wavelengths as a function of pump wavelength, the 900 nm waveguide was pumped with high peak power pulses. The output spectra for pump pulses with a different input wavelength are recorded. The peak power of the pulses is $\approx$ 15 W. From these spectra, the peak of the modulation instability at the discrete band is extracted. These points are the wavelengths which

are perfectly phase matched. The result is shown in figure 3.9.

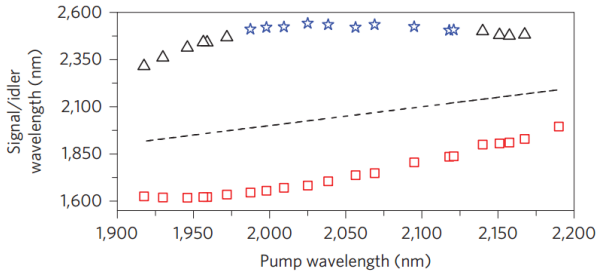

Figure 3.9: Experimental phase matched signal and idler wavelengths as a function of the pump wavelength.

3.3.2.1 Telecom-to-mid-infrared spectral translator

As seen in figure 3.9 phase matching between a signal, an idler and a pump with a very distinct wavelength can be achieved. Phase matching for a signal wavelength at around 1620 nm and an idler wavelength at around 2440 nm is achieved when the pump pulses are centered at $\approx$ 1950 nm. This feature is exploited to amplify a mid-ir signal around 2440 nm and converting it to 1620 nm. To measure the amplification, the pump pulses are combined with a mid-ir cw laser. The output spectrum is recorded and the amplification as well as the conversion efficiency are calculated. The conversion efficiency and amplification are plotted in figure 3.11. As shown in the figure, it is possible to achieve an amplification of almost 20 dB when the pump pulses have a central wavelength of 1947 nm and an on-chip peak power of 37.5 W. Since phase matching is obtained in a discrete band (see also section 3.1) the band where there is amplification is not as broadband as before.

The phase matching achieved by expanding the Taylor series up to the fourth order dispersion coefficient can be understood from the alternative approach explained in section 3.1.1 as well. When looking at figure 3.10, and comparing it with figure 3.2 it can be seen that an additional set of idler and signal frequencies enables phase matching. Here again, the average of their propagation constants is a factor γP smaller than the propagation constant at the pump frequency. This is only possible when the fourth order derivative of $\beta(\omega)$ at the pump wavelength is positive.

3.3.3 Octave spanning mid-infrared spectral translator

3.3.3.1 Introduction

In the previous section 900 nm wide waveguides were used to show that phase matching spectrally close to the pump as well as in a narrow band further from

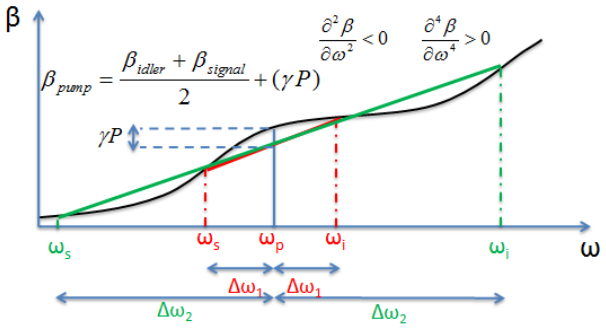

Figure 3.10: Experimental phase matching points vs pump wavelength.

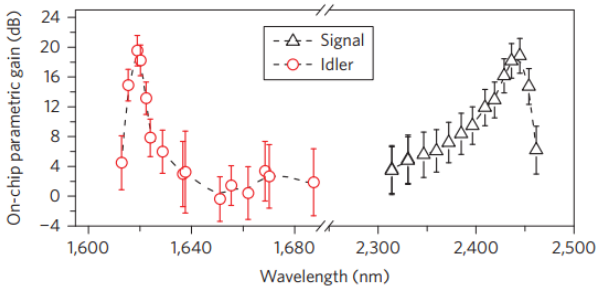

Figure 3.11: The amplification (signal) and conversion (idler) of a mid infrared signal in the 900 wide 2 cm long silicon-on-insulator waveguide.

the pump is possible. When a signal in the discrete band, were phase matching is achieved, is translated from the mid-infrared to the telecom wavelength in the 900 nm wide waveguide, the signal to noise ratio will decrease. This a result of the efficient amplification of background noise close to the pump. In a worst case, the amplification of the noise in these broad bands can even deplete the pump. A design of a waveguide, where the second order dispersion is positive while the fourth order dispersion is negative would therefor be more appealing. Such a waveguide would only have a phase matching point far from the pump (see figure 3.1). This section shows that it is possible to make such waveguides.

3.3.3.2 Design of waveguides with one phase matching point

Silicon waveguides with a height of 400 nm and a varying width were fabricated in the 200 mm pilot line at imec. A schematic cross-section of such a waveguide is shown in 3.12. The 400 nm silicon waveguide is resting on a 2 μm thick oxide. For certain pump wavelengths, these waveguides have only one detuning frequency for which phase matching occurs because the group velocity dispersion is normal and

the fourth order dispersion of such waveguides is negative. The linear phase mismatch for such waveguides is shown in figure 3.1 b). The propagation constant as a function of a wavelength is simulated to find signal and idler wavelengths which are phase matched with a certain pump wavelength. For every pump wavelength the signal and idler wavelength for which that $\beta_i + \beta_s - 2\beta_p + 2\gamma P = 0$ are calculated. For a set of waveguide widths the curves showing the phase matched idler and signal wavelength as a function of the pump wavelength are shown in 3.13. As seen on the figure, signal and idler wavelength can be separated over more than an octave. A nonlinear parameter of 15 $W^{-1}m^{-1}$ and a peak power of 1 W is assumed in the simulation.

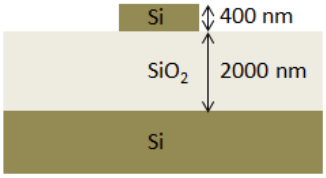

Figure 3.12: Schematic cross-section of a 400 nm high waveguide with an air cladding.

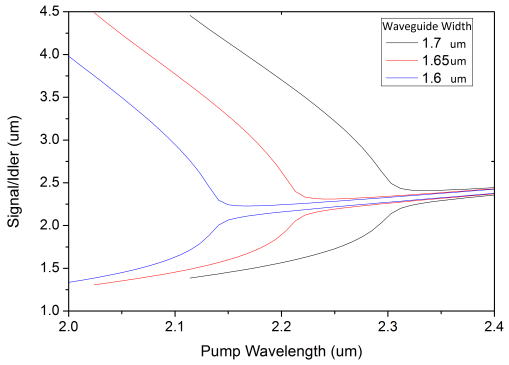

Figure 3.13: The phase matched idler and signal wavelength as a function of the pump wavelength for a set of waveguides with a height of 400 nm and a width of 1.6 um, 1.65 um and 1.7 um.

3.3.3.3 Results

A chip with 1 cm long waveguides is cleaved at both ends and lensed fibers are used to couple light in and out of the waveguides on the chip. The coupling loss at the facet is found to be 8.5 dB. In a first experiment the pump wavelength is tuned to a center wavelength of 2190 nm and coupled to the quasi-TE mode of the waveguide.

The output spectrum of the pulses is shown in figure 3.14. As can be seen in the figure, there is a modulation instability sideband around 1600 nm, however there is no modulation instability band close to the pump. Figure 3.15 shows for a set of pump wavelengths a zoom of the modulation instability in the telecom window. As shown in the figure, the location of the phase matched telecom wavelength is highly dependent on the pump wavelength. In a next experiment a telecom continuous wave signal is combined with the pulses to measure the amplification. The amplification as a function of wavelength for different pump wavelengths is shown in figure 3.15. The converted long wavelength idler cannot be seen with the optical spectrum analyzer because it extends beyond the operating wavelength range of the equipment. A Fourier Transform Infrared spectrometer (FTIR) is used to record the long wavelength light. To avoid the absorption in the single mode fiber, the light was coupled out of the chips with a high NA (NA =0.6) chalcogenide black diamond lens. The recorded spectrum is shown in figure 3.16. The light at 1565 nm is down converted over more than an octave to 3635 nm. In a last experiment the light is again coupled out of the chip with a lensed fiber and directed to a fast photodiode. The optical trace is recorded and is shown in figure 3.17. The peak power of the 2 ps pulses centered at 2190 nm is 19 W. The 1565 nm cw signal gets amplified when it temporarily overlaps with the pump pulses. The amplified pulse has a FWHM of 44 ps, much broader than the pump pulse. This is a result of both the limited bandwidth (60GHz) of the photodiode as well as the broadening of the pulse in the fiber after the chip as a result of the dispersion in the fiber. By integrating the energy underneath the pulse and comparing it with the energy in the cw signal over a timespan of 2 ps the amplification is calculated to be 13 dB.

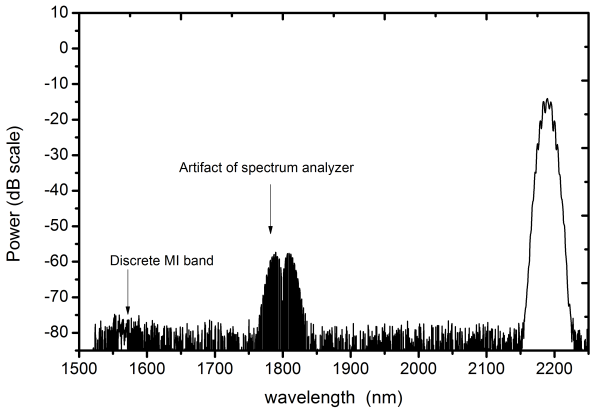

Figure 3.14: The output spectrum of a pulse with a coupled peak power of 20 W centered at 2190 nm after passing the 1650 nm wide waveguide.

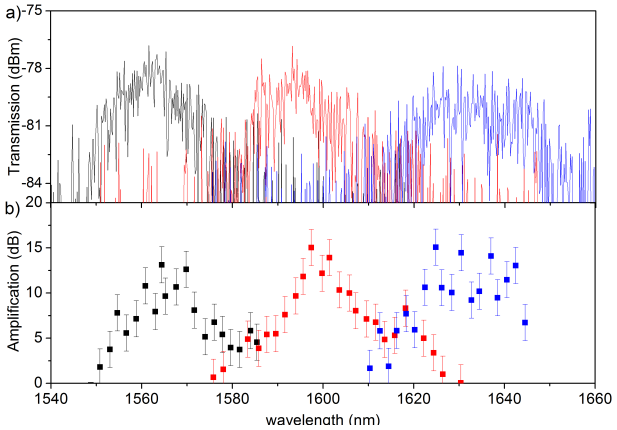

Figure 3.15: The modulation instability sidebands for a set of pump wavelengths centered at 2190 nm (black), 2200 nm (red) and 2210 nm (blue) respectively with a coupled peak power of 19.2 W, 18.3 W and 16.7 W.

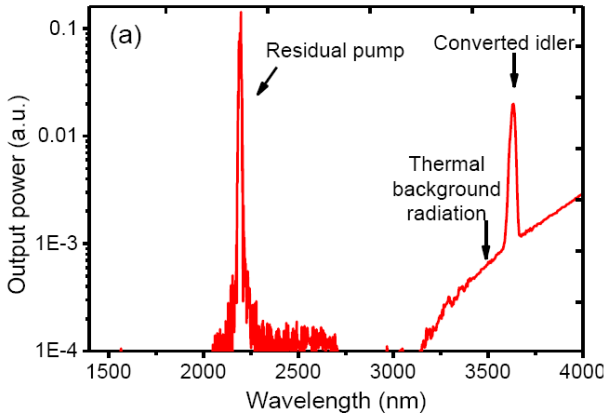

Figure 3.16: Octave spanning frequency conversion. The spectra recorded with an FTIR of the light coming out of the silicon chip. When the central wavelength of pump is tuned to 2190 nm and the peak power is 18.3 W it is possible to convert light at 1565 nm down to 3635 nm.

3.3.4 Future work

3.3.4.1 Fine tuning the group velocity dispersion

Several approaches have been suggested to fine tune the dispersion. They are mostly focused on adding a thin layer on top of a waveguide, for example Liu et al. [5] used a thin silicon nitride overlay to make the dispersion more normal and flatter in the telecommunication wavelength range. However, for the standard tele-

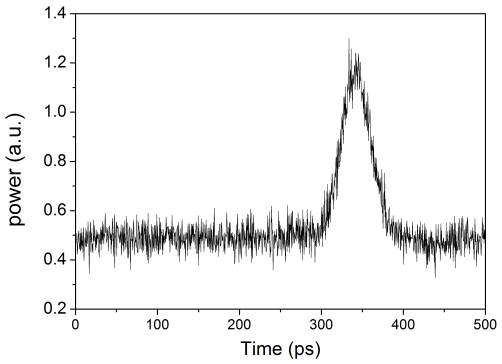

Figure 3.17: A trace showing the temporal evolution of the cw laser at 1565 nm. When the laser overlaps temporarily with the 19 W peak power pulses at 2190 nm, the cw signal gets amplified.

com waveguides with a height of 220 nm, we would like to make the dispersion more anomalous and shift the zero dispersion wavelength to longer wavelengths, which is not possible by changing the width of the waveguide. Having anomalous dispersion at longer wavelengths allows to use longer wavelength pulses and as such converting shorter wavelength signals to even longer wavelengths. This can be done by etching the silicon oxide buffer layer underneath the silicon waveguides. Figure 3.19 shows the simulated dispersion for a 900 nm wide waveguide. By etching the silicon oxide underneath the waveguide the dispersion becomes more anomalous. This can also be useful to fine tune the dispersion, when for example the waveguide height is not exactly 220 nm but a bit thinner. The oxide can be etched by immersing the chip in a HF/water solution. The HF will only etch the oxide and not the silicon. Figure 3.20 shows the resulting waveguide, after the chip has been immersed for 2 hours in a 1 % HF/water solution. The amount of silicon oxide removed by the etch can be well controlled by timing the immersion. Figure 3.21 shows the difference measured by a DEKTAK profilometer in height between the top of the silicon waveguide and the silicon oxide layer as a function of time. The etch rate is sufficiently slow to get nm precision.

Ir. Utsav Dave and Dr. Francois Leo are in the process of measuring the dispersion in a interferometric setup [6] to confirm the simulations experimentally. The initial results look promising, however this is outside the scope of this work.

3.3.4.2 Wavelength translation in silicon-on-sapphire waveguides

The silicon-on-insulator platform is not transparent anymore beyond 4 μm as a result of the absorption in silicon oxide. However when silicon-on-sapphire waveguides are used [7], these are silicon waveguides resting on a sapphire substrate,

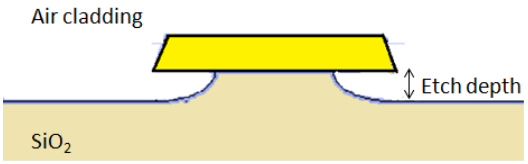

Figure 3.18: Schematic of a waveguide where the oxide has been etched by a HF/water solution.

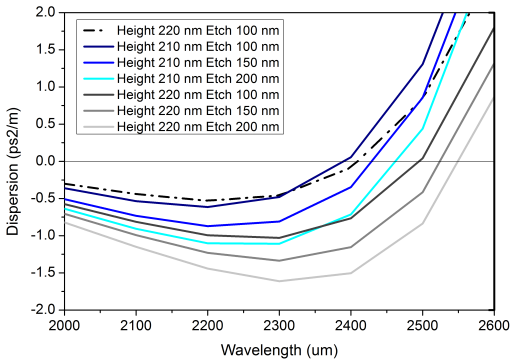

Figure 3.19: The dispersion for a 900 nm waveguide with a height of 210 and 220 nm and an air cladding when the oxide is removed by a HF/water solution. The broken line shows the dispersion for a waveguide which is not under etched.

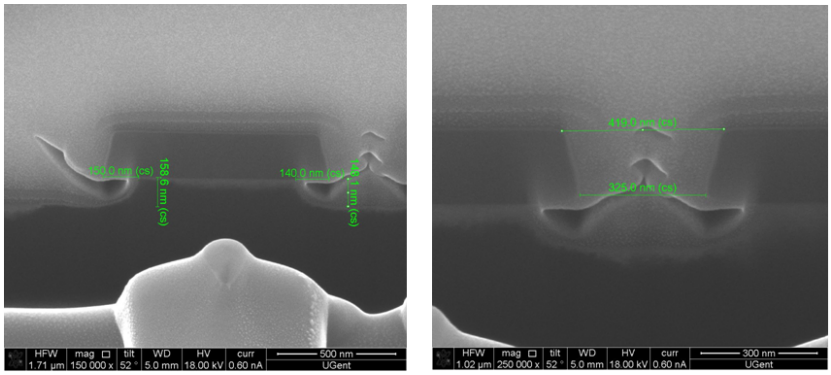

Figure 3.20: A silicon waveguide on top of a partially etched silicon oxide layer. The left panel shows a cross-section of a 900 nm wide silicon waveguide. The right panel shows a cross-section of a coupling section at a ring. Although the two waveguides have a small gap between them, the etch is very uniform and the oxide is removed uniformly.

this is no longer the case. The sapphire substrate is transparent beyond 5 μm. In

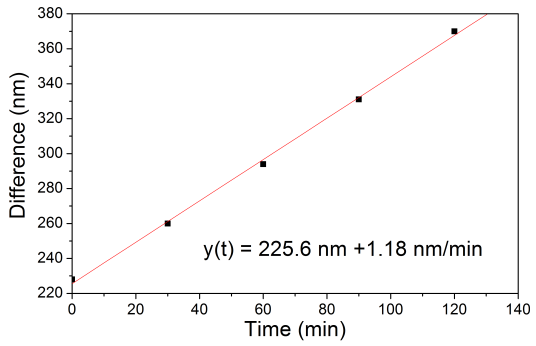

Figure 3.21: Controlling the amount of oxide removed. The solution is very diluted which makes the etching process slow and the amount of oxide removed is very linear as a function of the time it has been in contact with the HF solution.

a collaboration with the University of Sydney silicon waveguides able to convert signals beyond 4 μm are being fabricated. These waveguides are air clad 500 nm thick strip waveguides, resting on a sapphire substrate. The propagation constant as a function of the optical frequency is simulated in Fimmwave ©for a set of waveguides with a varying width. The phase matched idler and signal wavelength as a function of pump wavelength are calculated as in section 3.3.3. The phase matched idler and signal wavelength as a function of pump wavelength are shown in figure 3.22. As seen on the figure, it is possible to down convert signals to 5 mum.

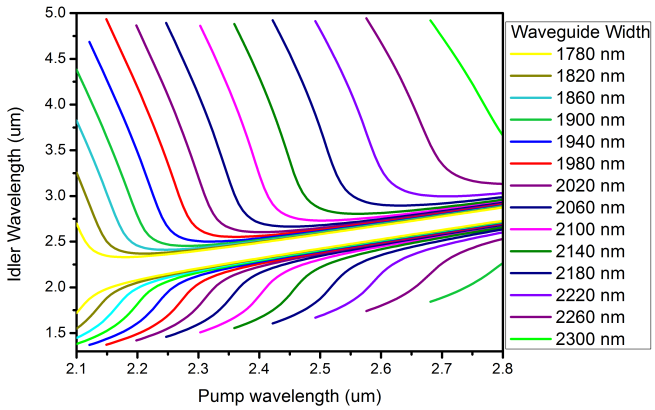

Figure 3.22: The phase matched idler and signal wavelength as a function of the pump wavelength for a set of silicon waveguides with a varying width and a height of 400 nm resting on a sapphire substrate.

3.3.4.3 Conversion of continuous wave signals

The experimental results obtained so far were performed using bright pulses as a pump. This section describes the design of silicon waveguides which can act as spectral translators for moderate cw powers. The proposed waveguide can be seen in figure 3.23. The calculated phase matched idler and signal wavelengths as a function of pump wavelength are shown in figure 3.24. At a pump wavelength of 2200 nm, the pump is phase matched with a signal at 1590 nm and a idler at 3550 nm. The conversion efficiency of a low power 3550 nm signal to the telecom band can be calculated by integrating the coupled wave equations governing the four wave mixing process [8]. Depending on the linear loss and length of such a waveguide the pump power needed to achieve efficient conversion can be as low as 65 mW. Figure 3.25 shows the conversion efficiency for a set of waveguides with optimized lengths when they have a loss of 0.1 dB/cm, 0.3 dB/cm and 0.6 dB/cm respectively. The parameters used in the simulation can be found in the supplemental information of [4].

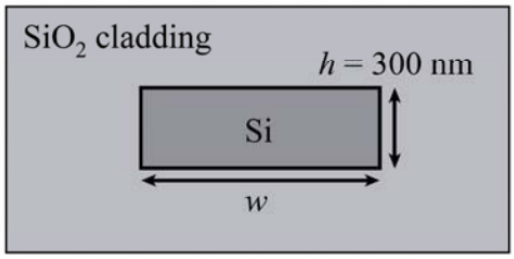

Figure 3.23: A cross-section of a silicon waveguide which can act as a spectral translator for continuous wave signals.

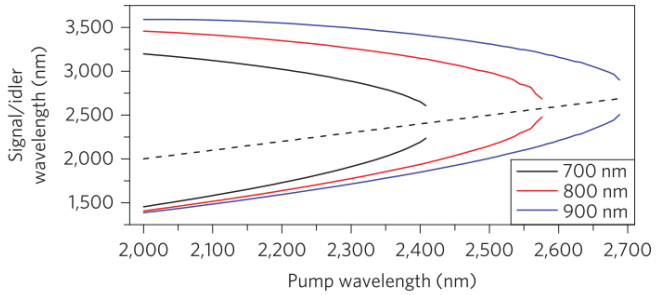

Figure 3.24: The phase matched idler and signal wavelength as a function of the pump wavelength in the spectral translator.

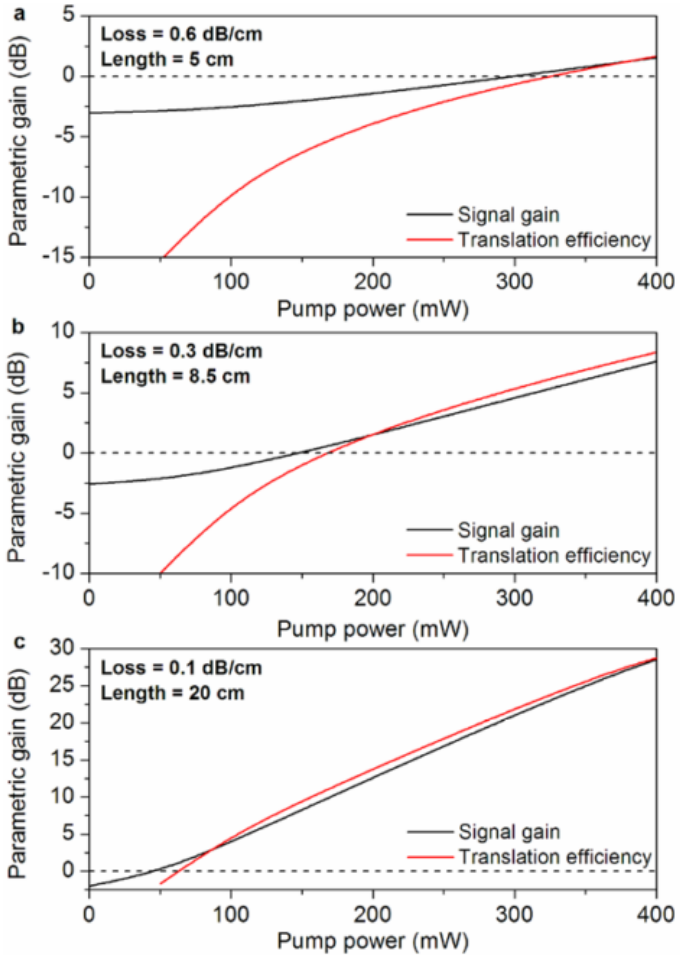

Figure 3.25: Simulated parametric spectral translation efficiency and signal gain versus continuous-wave pump power, for an oxide-clad silicon nanophotonic wire with w = 900 nm and h = 300 nm. Using a pump wavelength of 2200 nm, a mid-IR input signal at 3550 nm is spectrally translated to an L-band idler at 1590 nm. Silicon wires with linear propagation losses of a, 0.6 dB/cm, b, 0.3 dB/cm, and c, 0.1 dB/cm are considered, which have optimal lengths of 5 cm, 8.5 cm, and 20 cm respectively for a pump power of 300 mW. The pump power required to reach a translation efficiency of 0 dB (dashed black line) is 320 mW, 170 mW, and 65 mW for the 0.6 dB/cm, 0.3 dB/cm, and 0.1 dB/cm silicon wires, respectively

3.4 Conclusion

This chapter discusses optical parametric amplification in silicon waveguides. Broadband amplification of signals with a wavelength close to the pump wavelength of $\approx$ 2200 nm has been demonstrated. Next the amplfication and conversion of signals in the telecommunication band by a mid-ir pump at $\approx$ 2200 nm is shown. Telecommunication signals can be converted over more than an octave to a wavelength of 3630 nm. At the same time it is possible to amplify the telecom signals up to 13 dB. It is also shown that efficient continuous wave conversion is within reach on the silicon-on-insulator platform.

3.5 50 dB Parametric On-chip Gain in Silicon Photonic Wires

The content of this section is published in Optics Letters [2]

Two-photon absorption (TPA) in Si vanishes at wavelengths approaching λ = 2200 nm, while its nonlinear Kerr refractive index n_2 stays comparatively constant [9]. Hence, the nonlinear figure of merit (FOM) ($\frac{n_2}{\beta\lambda}$) increases dramatically near silicon's TPA threshold. The large intrinsic nonlinearity of Si, when patterned into high-index-contrast dispersion-engineered silicon photonic wires, produces an ideal platform for the exploration of highly efficient, broadband, coherent nonlinear optical processes [10]. This platform can serve as an ideal host for chip-scale mid-IR applications [11–14] including molecular spectroscopy, free-space communication, and environmental monitoring. Previously we reported a mid-IR optical parametric amplifier (OPA) with on-chip gain over a 220 nm bandwidth in a 4-mm long silicon wire [11]. Using an improved design, here we demonstrate broadband mid-IR modulation instability (MI), having a bandwidth greater than 580 nm centered at a 2173 nm pump wavelength. The intense MI spectrum correlates with unprecedented values of on-chip parametric gain, exceeding 40 dB. Moreover, we demonstrate that on-chip gain exceeds 50 dB in narrow Raman-scattering-assisted bands. To achieve an efficient degenerate four-wave-mixing (FWM) process (i.e. $2\omega_p = \omega_s + \omega_i$, where ω_p, ω_s, and ω_i are the pump, signal, and idler angular optical frequencies), the phase matching condition [1] restricts the frequency detuning of signal/idler from pump $\Delta\omega = \|\omega_p - \omega_s\| = \|\omega_p - \omega_i\|$ to values that satisfy $\|\Delta k_l + 2\gamma P\| \leq (4\gamma PL)^{1/2}/L$ or $2\gamma P - (4\gamma PL)/L^{1/2} \leq \Delta k_l \leq 2\gamma P + (4\gamma PL)^{1/2}/L$. Here, Δk_l is the linear phase-mismatch in propagation constants between signal/idler and pump, $\Delta k_l = (k_s + k_i) - 2k_p$, γ is the waveguide's effective nonlinearity parameter, P is the input pump peak power and L is the waveguide length. Graphically, when the $-\Delta kl$ curve falls into a band bounded between $2 - (4\gamma PL)/L^{1/2}$ and $2 + (4\gamma PL)/L^{1/2}$ (i.e. the horizontal hatched bands in Fig. 3.26, efficient phase

matching is achieved. Using a Taylor-series, Δk_l can be related to $\Delta\omega$ through $-\Delta k_l \approx -\beta_2\Delta\omega^2 - \beta_4\Delta\omega^4/12$, where β_2 and β_4 are the waveguide's second-order and fourth-order dispersion coefficients, respectively. Fig. 3.26 schematically illustrates a typical phase-matching relationship for β_2 <0 and β_4 0. The solid black curve depicting Δk_l initially increases, reaches a peak, and then decreases with increasing frequency detuning from the pump. At low power levels, there exist two phase-matched regions (i.e., intersecting with the horizontal black hatched band in Fig. 3.26, as shown by the solid black and the dashed black arrow. At small frequency detuning, a broadband gain region typically seen in parametric amplification [10, 11] is found. At large frequency detuning, the gain has a narrower bandwidth, termed here a discrete-band [15] due to the relatively large slope of Δk_l. When the pump power is increased (i.e., from black to the red hatched bands), the broadband and discrete phase-matched bands shift closer together. At high pump power levels these two regions eventually merge together to create a single ultra-broadband phase-matched region, depicted by the dotted blue arrow and blue hatched band.

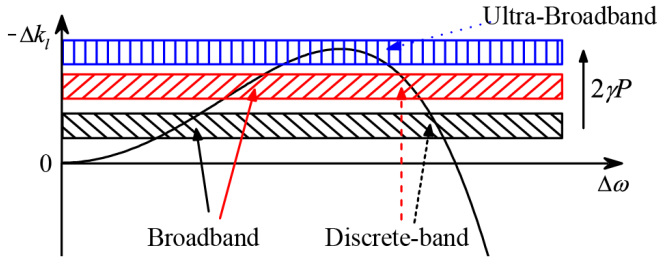

Figure 3.26: Schematic illustration of pump-detuning-dependent broadband, discrete-band, and ultra-broadband phase-matched regions for FWM. The horizontal black, red and blue hatched bands correspond conditions with increasing pump power.

We performed a series of FWM experiments to investigate the bandwidth and magnitude of parametric gain and wavelength conversion when operating within the ultra-broadband phase-matching region. Our Si wire is fabricated on a 200 mm silicon-on-insulator wafer in a CMOS pilot line and is 2 cm long, with cross-sectional dimensions of 900 nm 220 nm. The top/bottom cladding consist of air/2μm buried oxide, respectively. The waveguide operates in the fundamental quasi-TE mode, with propagation losses of $<$ 2.8 dB/cm for $\lambda \approx$ 2000-2500 nm, and has a γ parameter $\approx$ 150 $(Wm)^{-1}$. The Si wire is pumped with a picosecond pulse train at λ = 2173 nm (FWHM $\approx$ 2 ps, repetition rate = 76 MHz) from an OPA. The polarization of the pump and probe are controlled to co-excite the Si wire's quasi-TE mode using in-line fiber polarization controllers. Pump and probe are multiplexed with a 90/10 fused-fiber coupler. Coupling into/out of the Si wire is via lensed fibers, with coupling losses of $\approx$ 10 dB/facet. An optical spectrum

analyzer is used to record the input/output spectra at 1 nm resolution bandwidth.

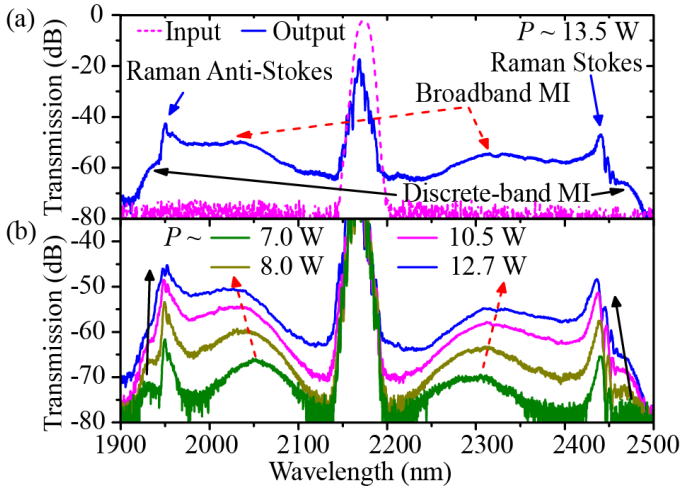

Figure 3.27: (a) Input (dashed magenta) and output (solid blue) pump spectrum, taken with an input peak power P ≈ 13.5 W and λ = 2173 nm, illustrating ultra-broadband MI, and Raman Stokes/anti-Stokes peaks. (b) MI spectra with four different pump peak power levels at pump wavelength λ = 2173 nm.

The dashed magenta trace in Fig. 3.27 (a) depicts the pump spectrum at the input of the Si wire. The pump has an instrumentation-limited signal-to-noise ratio $>$ 75 dB, and a peak on-chip power of P $\approx$ 13.5 W. The pump's transmission spectrum obtained at the wire output (solid blue curve in Fig. 3.27 (a)) exhibits features commonly observed for pulse propagation through Si waveguides, these being self-phase modulation-induced (SPM) spectral oscillations on the original pump spectrum, and a blue-shift due to residual free-carrier dispersion [16, 17]. The transmitted pump spectrum also exhibits additional modifications, several of which are observed here for the first time in Si wires. Most notably, the output spectrum is characterized by the emergence of a strong ultra-broadband modulation instability (MI) background [1], extending from 1911 nm to 2486 nm. Furthermore, a prominent Raman Stokes peak, down-shifted from the pump by 15.6 THz [14], rides on top of the MI spectrum at λ = 2411 nm. Finally, a coherent Raman anti-Stokes peak is visible at a wavelength of 1950 nm. Strong Raman interaction occurs within the Si waveguide after SPM-induced spectral narrowing significantly compresses the -3 dB bandwidth of the negatively-chirped input pulse from $\approx$740 GHz to $\approx$ 140 GHz [15], a value comparable to the spectral bandwidth of Raman scattering in Si. Sharp interference fringes occur near the Raman peaks, where the dispersion and phase shift due to the Raman susceptibility disrupts the broadband FWM phase-matching condition [18]. Fig. 3.27 (b) shows a series of

pump-power dependent MI spectra. With increasing pump power, the centers of the broadband MI peaks move away from the pump (dashed red arrows), while the narrower discrete MI peaks move closer to the pump (solid black arrows), an observation consistent with the schematic in Fig. 3.26. Using the observed detuning $\Delta\omega$ of MI peaks from pump, along with the values of the pump power-dependent nonlinear phase shift 2, we generate an experimental fit describing the Si wire's dispersion coefficients (as outlined in [19]). At the pump wavelength of 2173 nm,β_2 and β_4 are estimated to be $-0.6ps^2/m$ and $5.110^{-4}ps^4/m$, respectively. While the β_2 value is reasonably close to the value of $-0.52ps^2/m$ obtained from simulations, the β_4 is an order of magnitude larger than numerically predicted. This deviation is primarily due to the fact that the simulations do not capture the nanometer-scale fabrication tolerances in the wire's cross-sectional dimensions [19], which have a significant impact on higher-order dispersion.

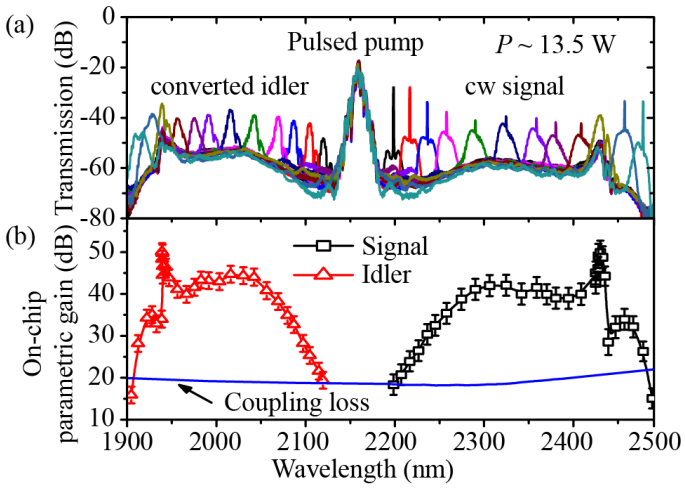

Figure 3.28: (a) Series of FWM spectra with the pulsed pump co-propagating with a cw mid-IR signal at various wavelengths. The pulsed pump is centered at λ = 2173 nm, and has P ≈ 13.5 W. (b) Spectrum of on-chip parametric signal gain (black squares) and idler conversion gain (red triangles). Fiber-waveguide coupling loss measured with cut-back method is shown by the blue trace.

The visibility of a strong noise-seeded spontaneous emission/MI background suggests that the on-chip mid-IR parametric gain available here is far larger than that demonstrated in previous studies [11], where no such MI was observed. As shown by the overlaid spectra in Fig. 3.28 (a), the parametric amplification is probed using a cw signal with wavelengths varying from 2209 nm - 2498 nm (8 nm step size), thus generating the corresponding idler terms from 2129 nm - 1914 nm. The cw signal power coupled into the waveguide is kept low (¡ 0.06 mW) to prevent pump depletion, yet high enough to achieve visibility of the idler

above the MI spectrum. The pedestal around the cw signals in Fig. 3.28(a) is formed by the amplified pulsed signal, and its height relative to the cw signal on the spectra is roughly proportional to the on-chip gain [11]. Fig. 3.28(b) plots the measured on-chip amplification and conversion gain, defined as the ratio between the peak power of pulsed signal/idler at the end of the waveguide and the coupled input cw signal power (see [11] for details). The mid-IR-pumped Si wire OPA exhibits on-chip optical parametric amplification over a bandwidth exceeding 580 nm. Within the Raman Stokes/anti-Stokes bands, the OPA reaches a maximum value of Raman-assisted parametric signal/idler gain of $\approx$ 50 dB. Note that the gain profile also contains interference patterns near the Raman-assisted peaks, at wavelengths of $\approx$ 2445 nm and $\approx$ 1950 nm. These features are related to those seen in the MI spectrum of Fig. 3.27(a). However, the number of interference fringes observed in Fig. 3.28(b) is reduced, because the cw probe's linewidth is broadened by cross-phase modulation , in combination with the limited resolution of the 8-nm probe tuning step. After compensating for all fiber-chip coupling losses ($\approx$ 20 dB), the OPA shows a net off-chip gain bandwidth of $\approx$ 550 nm, with$\approx$ 30 dB Raman-assisted peak off-chip gain for both signal and idler. The off-chip parametric amplification resulting solely from FWM can be $>$ 20 dB. Large values of on-chip parametric amplification can lead to pump depletion [1] and even gain saturation at high input signal power. This is seen in a plot of output pulsed signal/idler peak power v.s. input cw signal power shown in Fig. 3.29 (a). Here the input pump peak power is P $\approx$ 13.5 W. The signal wavelength is positioned near the FWM parametric gain maximum (λ_s = 2356 nm), but outside the Raman band. At low signal-power levels, the power of the amplified signal and converted idler increase linearly with signal power, resulting in a signal and idler on-chip parametric gain of 39.5 and 42.3 dB, respectively. The output signal/idler power saturates at $\approx$ 20 dBm, for input signal powers $>$ -19 dBm. This gain saturation can be useful for limiting all-optical regeneration of signals.

Fig. 3.29(b) plots the signal/idler on-chip parametric gain vs. input peak pump power while keeping the signal wavelength at λ_s = 2356 nm and its power at 23.3 dBm. After compensating for the 20 dB coupling loss, off-chip optical transparency can be achieved for a peak pump power about 8 W, which can be further reduced by improving upon the cleaved-facet input coupling mechanism used here. The differential gain is about 10.4 dB/W at low peak power $\approx$ 6.5 W but decreases to 2.7 dB/W for a peak power $>$ 10 W. This decrease is in part due to the residual nonlinear loss. However, as shown in Fig. 3.29 (b) even at the highest peak power, the on-chip parametric gain does not fully saturate, but rather continues to grow with a reduced differential gain. The results obtained here represent a substantial improvement over those reported previously for mid-IR parametric amplification in a 4 mm-long silicon wire waveguide. The peak operating pump power is reduced to less than half in the present device. At the same time, the maximum

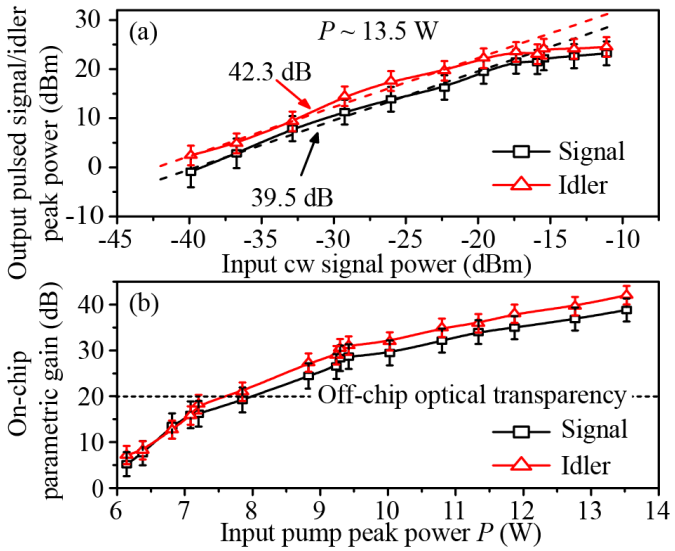

Figure 3.29: (a) Output pulsed signal/idler peak power v.s. input cw signal power at λ_s = 2356 nm, with input pump peak power P ≈ 13.5 W. (b) On-chip parametric gain as a function of P. Off-chip optical transparency is achieved with a peak power of ≈ 8 W.

on-chip gain obtained using this 2 cm-long wire here shows an improvement of more than 25 dB, while the on-chip gain bandwidth is increased by more than 2.5. These results were achieved by leveraging judicious dispersion engineering and reduced propagation loss in the silicon wires, to achieve dramatic increase in parametric gain and its bandwidth, including phase-matching of the Raman scattering process.

3.6 Bridging the mid-infrared-to-telecom gap with silicon nanophotonic spectral translation

The content of this section is published in Nature Photonics [4]

Expanding far beyond traditional applications in optical interconnects at telecommunications wavelengths, the silicon nanophotonic integrated circuit platform has recently proven its merits for working with mid-infrared (mid-IR) optical signals in the 2-8 mum range. Silicon's broadband transparency [14, 20], strong optical confinement, and potential for co-integration with CMOS electronic are but a few of the many characteristics making the silicon platform ideal for development of high-performance, densely-integrated mid-IR optical systems. These systems are capable of addressing applications including industrial process and environmental monitoring, threat detection, medical diagnostics, and free-space communication.

Rapid progress has led to the demonstration of various silicon components designed for the on-chip processing of mid-IR signals, including waveguides [21], vertical grating couplers, microcavities, and electrooptic modulators. Even so, a notable obstacle to the continued advancement of chip-scale systems is imposed by the narrow-bandgap semiconductors, such as InSb and HgCdTe, traditionally used to convert mid-IR photons to electrical currents. The cryogenic or multi-stage thermo-electric cooling required to suppress dark current noise, exponentially dependent upon the ratio Eg/kT, can limit the development of small, low-power, and low-cost integrated optical systems for the mid-IR. However, if the mid-IR optical signal could be spectrally translated to shorter wavelengths, for example within the near-infrared telecom band, photodetectors using wider bandgap semiconductors such as InGaAs or Ge could be used to eliminate prohibitive cooling requirements. Moreover, telecom band detectors typically perform with higher detectivity and faster response times when compared with their mid-IR counterparts. Spectral translators employing sum or difference frequency generation in nonlinear crystals, including LiNbO3 and KTP, have been studied. However, such systems can be impeded by low conversion efficiencies, their significant size, and limited integrability of their component parts. Here we address these challenges with a silicon-integrated approach to spectral translation, by employing efficient four-wave mixing (FWM) and large optical parametric gain in silicon nanophotonic wires [12, 22]. Using an optical pump near silicon's two-photon absorption (TPA) threshold [9], we excite nanophotonic wires uniquely engineered to use higher-order waveguide dispersion to facilitate spectral translation of a mid-IR input signal at 2440 nm to the telecom band at 1620 nm, across a span of 62 THz. The converted signal simultaneously experiences a translation gain of more than 19 dB, an efficiency enhancement which can dramatically improve the detection sensitivity for weak mid-IR signals. Moreover, this single silicon device also performs as a transmitter, by converting telecom band signals to the mid-IR with a translation gain of 8.0 dB. Finally, an 8.4 dB optical parametric amplification of telecom band signals is demonstrated when using a mid-IR pump, reinforcing the wide-ranging technological role silicon nanophotonic wires can serve within both the mid-IR and telecom bands.

Mid-IR to telecom band spectral translation in silicon wires can be accomplished using efficient FWM with discrete band phase-matching [15]. In this process, the pump is placed away from the zero dispersion wavelength, and higher-order waveguide dispersion is used to phase-match a discrete pair of bands at spectrally distant frequencies, located symmetrically on either side of the pump. Discrete band phase-matching can be achieved in a waveguide with anomalous 2nd-order dispersion ($\beta_2 < 0$) and small positive 4th-order dispersion ($\beta_4 > 0$), conditions which are engineered through manipulating the cross-sectional dimensions and cladding materials of the silicon nanophotonic wire. Figure 3.30 a shows

an optical microscope image of the 2 cm long silicon nanophotonic wire used here for spectral translation, as fabricated on a 200 mm silicon-on-insulator (SOI) wafer at imec, through the multi-project-wafer service ePIXfab (www.ePIXfab.eu). The entire length of the wire is coiled into a compact spiral, occupying an on-chip footprint of only 625 μm by 340 μm. The wire has cross-sectional dimensions of w = 900 nm by h = 220 nm, as shown in Fig. 3.30. The cladding consists of air above and a 2 μm buried oxide (SiO2) below the silicon core. Numerical simulations indicate that the dispersion conditions $\beta_2 < 0$ and $\beta_4 > 0$ are satisfied over the spectral range from 1810-2410 nm (see Supplementary Figure 2). Over a similar range, a large effective nonlinearity parameter of $\gamma \approx 130(Wm)^{-1}$ and a low propagation loss of 2.6 dB/cm also serve to facilitate highly efficient FWM for this compact device.

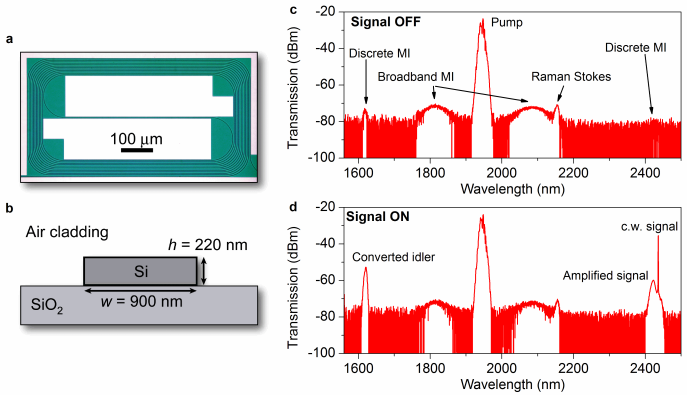

Figure 3.30: Structural design and transmission characteristics of the silicon nanophotonic wire spectral translation device. a) Optical microscope image of the spiral-coiled silicon wire. The wire has a total length of 2 cm, and occupies an on-chip footprint of only 625 μm x 340 μm. Bends with a conservative 60 μm radius are used. b) Cross-sectional schematic, illustrating a silicon core with a width of w = 900 nm and a height of h = 220 nm, which lies upon a 2 μm thick SiO2 buried oxide layer. The silicon core is air-clad from above. c) Output transmission spectrum with pump operating at λ = 1946 nm and input signal OFF. The observed modulation instability spectrum generated by amplification of background noise serves as a marker of the spectral bands in which phase-matching conditions are met. The location of the broadband MI peaks adjacent to the pump at 1810 nm and 2090 nm is primarily determined by β_2, while the discrete MI bands at 1620 nm and 2440 nm occur as a result of higher-order phase-matching dictated by the values of both β_2 and β_4. A Raman Stokes peak is also observed at 2155 nm. d) Transmission spectrum with input signal ON. A c.w. mid-IR signal is tuned to coincide with the discrete MI band at 2440 nm. Parametric amplification of the signal occurs with simultaneous spectral translation across 62 THz, to an idler at 1620 nm.

The nonlinear mixing and spectral translation characteristics of the silicon nanophotonic wire are illustrated in Figs. 3.30 c-d. Figure 3.30 c) shows the

recorded output spectrum when the wire is excited by a pump pulse-train at 1946 nm having a peak coupled input power of 37.3 W . While this pump wavelength is not yet beyond silicon's TPA threshold of 2200 nm23, the TPA coefficient is nevertheless a factor of 2-3x lower than that at 1550 nm, resulting in small nonlinear loss and efficient FWM. For example, in the absence of any probe signal (Signal OFF), the pump transmission spectrum already exhibits clear signatures of the desired phase-matched FWM processes. Specifically, strong broadband modulation instability (MI) peaks22 appear adjacent to the pump at 1810 nm and 2090 nm. Moreover, two additional discrete MI bands with much larger detuning from the pump appear at 1620 nm and 2440 nm, and serve as direct evidence of higher-order phase-matching. The absolute power of the MI band at 2440 nm appears lower than that of the MI band at 1620 nm, due to a 1.8 dB asymmetry expected from the Manley-Rowe power division relations, as well as from 3-4 dB larger losses in the output fibre optical collection path at longer wavelengths.

The visibility of the MI bands, associated with the parametric amplification of background noise, suggests that the pumped silicon nanophotonic wire should exhibit significant parametric gain as well as a large conversion efficiency when probed by input signals at these wavelengths. Figure **??** d) illustrates the output spectrum in one such case, when the long-wavelength discrete MI band is probed (Signal ON) by a low-power (Psig $<$ 35 W) continuous-wave mid-IR signal at 2440 nm. When the signal is tuned into resonance with this spectral band, it experiences strong parametric amplification through degenerate FWM (evidenced by the appearance of the large spectral pedestal), and is simultaneously up-converted to a prominent telecom band idler at 1620 nm. This large spectral translation over more than 62 THz illustrates that the higher-order dispersion design methodology applied here may be used to efficiently convert optical information on a mid-IR carrier into the telecom band, where it can be detected and processed using uncooled, high-speed, high-sensitivity III-V and group-IV semiconductor detector technologies.

By recording transmission spectra for a range of signal wavelengths near 2440 nm and 1620 nm, the wavelength dependence of spectral translation efficiency and parametric gain within the discrete phase-matching bands can be determined. Figure 3.31 a illustrates that for mid-IR input signals, the silicon wire device attains optical transparency (on-chip gain exceeding 0 dB) across a bandwidth of 150 nm near the signal and 45 nm near the idler. The data also demonstrates that spectral translation of mid-IR signals to the telecom band idler near 1620 nm takes place with a peak conversion gain of 19.5 dB. Therefore, not only could such a spectral translator facilitate detection of mid-IR signals without cumbersome cooling requirements, the associated optical gain could also dramatically improve the sensitivity of such a receiver system, particularly for weak mid-IR input levels. At the same time, the mid-IR input signal experiences a peak on-chip parametric

amplification of 18.8 dB.

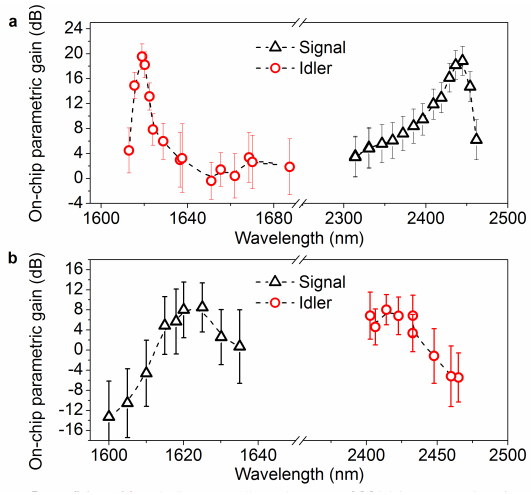

Figure 3.31: Wavelength-resolved on-chip spectral translation efficiency and parametric signal gain. a) Injection of a mid-IR input signal (Psig $<$ 35 W), with translation to a telecom band output idler. The peak on-chip translation efficiency is 19.5 dB, while the signal gain is 18.8 dB. The transparency bandwidth exceeds 45 nm near the idler, and 150 nm near the signal. b) Reversed scenario, with injection of a telecom band input signal (Psig $<$ 50 W) and translation to a mid-IR output idler. The peak on-chip translation efficiency is 8.0 dB, and the signal gain is 8.4 dB. Transparency is reached over a bandwidth of 40 nm near the idler and 20 nm near the signal. In all of the above measurements, the silicon nanophotonic wire is pumped at 1946 nm with a peak power of 37.3 W. The small shift in the spectral position of the mid-IR gain peak between Fig. a and Fig. b (2440 nm versus 2420 nm, respectively) occurs as a result of pump wavelength drift. The dashed curves are included as a guide to the eye.

Figure 3.31 b shows the result of a similar set of experiments, in which a telecom band input signal is tuned across the MI peak near 1620 nm. In this case, the on-chip transparency bandwidth is approximately 20 nm for the signal and 40 nm for the idler. The telecom band signal is spectrally translated to the mid-IR with a peak gain of 8.0 dB, a process which can be applied to generating and transmitting arbitrary mid-IR signals using commercially-available telecom components. In addition to performing the spectral translation function, Fig. 3.31 b illustrates that the telecom band input signal is simultaneously amplified by 8.4 dB. The demonstration of a silicon wire amplifier which utilizes a mid-IR pump to provide substantial parametric gain to a telecom band signal is of particular technological significance, as such an amplifier could find applications within the CMOS-integrated silicon nanophotonic platforms currently being developed for high-speed optical interconnect systems3.

The spectral translation of the telecom band signal to the mid-IR shown in Fig.

3.31 b occurs with an approximately 11 dB gain reduction when compared with the reversed scenario illustrated in Fig. 3.31 a. As the energetic combination of a 1620 nm signal photon with a pump photon lies significantly above silicon's bandgap, the observed asymmetry is expected due to the effects of non-degenerate TPA in the silicon wire. Non-degenerate TPA produces larger attenuation of an input signal near 1620 nm as compared to one near 2440 nm, when each is combined with the strong pump at 1946 nm. Therefore, larger gain values could be expected for the telecom band signal if the pump wavelength were increased.

An optimization of the silicon nanophotonic wire dispersion design, focusing upon increasing $|\beta_2|$ while simultaneously decreasing $|\beta_4|$, can facilitate translation of even longer wavelength mid-IR signals into the telecom band. For example, Fig. 3.32 b) plots numerical calculations of the phase-matched discrete signal and idler wavelengths of a design tailored for translating a range of mid-IR signals from 3000-3550 nm into the L-band. This spectrum is targeted for its overlap with a mid-IR low-loss window in SiO21. This design consists of a silicon wire with a thickness of 300 nm and a width in the range of 700-900 nm, completely surrounded by an oxide cladding. In the specific case of a wire with w = 900 nm and h = 300 nm, Fig. 3.32 b illustrates that an input signal at 3550 nm could be spectrally translated to an L-band idler at 1590 nm (and vice versa), using a pump wavelength of 2200 nm. This corresponds to a span of 104 THz, more than an octave in optical frequency.

In conclusion, we have shown that judicious engineering of FWM processes in silicon nanophotonic wires can facilitate amplified bi-directional spectral translation of signals between the mid-IR and the telecom band, across a 62 THz span in optical frequency. Telecom band detection of translated mid-IR signals can eliminate the burdensome cooling requirements traditionally associated with mid-IR photodetectors, and can be performed by on-chip photodetectors integrated via heterogeneous or monolithic techniques. Moreover, these spectral translation devices can be integrated with additional mid-IR and/or telecom band silicon nanophotonic components such as modulators, wavelength (de-)multiplexers, and switches, which together have the potential to produce flexible, chip-scale optical systems for mid-IR applications.

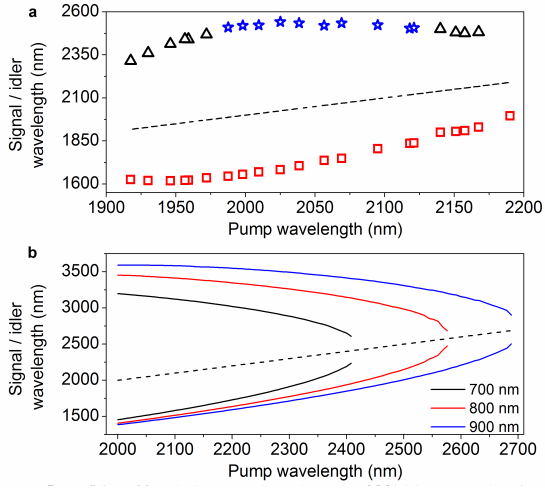

Figure 3.32: Phase-matched signal and idler wavelengths linked by the silicon nanophotonic spectral translation process. a) The symbols mark the spectral locations of the discrete MI bands as a function of pump wavelength, for the experimentally demonstrated silicon wire having w = 900 nm, h = 220 nm. The MI bands indicated by blue stars were not measured directly, as they were located beyond the 2500 nm maximum wavelength limit of the spectrum analyzer used. The positions of these bands were therefore inferred from energy conservation. b) Design calculations describing the phase-matched discrete band locations versus pump wavelength, for the fundamental quasi-TE mode of an SiO2-clad silicon wire with h = 300 nm and widths w = 700 nm, 800 nm, and 900 nm. The wires are tailored for spectral translation across more than an octave in optical frequency, between the 3000-3550 nm mid-IR range and the L-band. The calculations assume c.w. pumping with 300 mW pump power. In both panels, the dashed line marks the pump wavelength.

References

[1] Govind P Agrawal. *Nonlinear fiber optics*. Springer, 2000.

[2] Bart Kuyken, Xiaoping Liu, Günther Roelkens, Roel Baets, Richard M Osgood, and William M J Green. *50 dB parametric on-chip gain in silicon photonic wires.* Optics Letters, 36(22):4401–3, November 2011.

[3] Xiaoping Liu, Richard M Osgood, Yurii A Vlasov, and William MJ Green. *Mid-infrared optical parametric amplifier using silicon nanophotonic waveguides*. Nature Photonics, 4(8):557–560, 2010.

[4] Xiaoping Liu, Bart Kuyken, Gunther Roelkens, Roel Baets, Richard M Osgood Jr, and William MJ Green. *Bridging the mid-infrared-to-telecom gap with silicon nanophotonic spectral translation*. Nature Photonics, 6(10):667–671, 2012.

[5] Xiaoping Liu, William M J Green, Xiaogang Chen, I-Wei Hsieh, Jerry I Dadap, Yurii a Vlasov, and Richard M Osgood. *Conformal dielectric overlayers for engineering dispersion and effective nonlinearity of silicon nanophotonic wires.* Optics Letters, 33(24):2889–91, December 2008.

[6] Ji Yong Lee and Dug Young Kim. *Versatile chromatic dispersion measurement of a single mode fiber using spectral white light interferometry.* Optics Express, 14(24):11608–15, November 2006.

[7] Fangxin Li, Stuart D Jackson, Christian Grillet, Eric Magi, Darren Hudson, Steven J Madden, Yashodhan Moghe, Christopher O Brien, Andrew Read, Steven G Duvall, Peter Atanackovic, Benjamin J Eggleton, and David J Moss. *Low propagation loss silicon-on-sapphire waveguides for the mid-infrared*. Optics Express, 19(16):15212–15220, 2011.

[8] Q Lin, Oskar J Painter, and Govind P Agrawal. *Nonlinear optical phenomena in silicon waveguides: modeling and applications.* Optics Express, 15(25):16604–44, December 2007.

[9] Alan D. Bristow, Nir Rotenberg, and Henry M. van Driel. *Two-photon absorption and Kerr coefficients of silicon for 8502200nm.* Applied Physics Letters, 90(19):191104, 2007.

[10] Mark a Foster, Amy C Turner, Jay E Sharping, Bradley S Schmidt, Michal Lipson, and Alexander L Gaeta. *Broad-band optical parametric gain on a silicon photonic chip.* Nature, 441(7096):960–3, June 2006.

[11] Xiaoping Liu, Richard M. Osgood, Yurii a. Vlasov, and William M. J. Green. *Mid-infrared optical parametric amplifier using silicon nanophotonic waveguides*. Nature Photonics, 4(8):557–560, May 2010.

[12] Sanja Zlatanovic, Jung S Park, Slaven Moro, Jose M Chavez Boggio, Ivan B Divliansky, Nikola Alic, Shayan Mookherjea, and Stojan Radic. *Mid-infrared wavelength conversion in silicon waveguides using ultracompact telecom-band-derived pump source*. Methods, 4(August):561–564, 2010.

[13] Ryan K W Lau, Michaël Ménard, Yoshitomo Okawachi, Mark a Foster, Amy C Turner-Foster, Reza Salem, Michal Lipson, and Alexander L Gaeta. *Continuous-wave mid-infrared frequency conversion in silicon nanowaveguides.* Optics Letters, 36(7):1263–5, April 2011.

[14] Varun Raghunathan, Ramesh Shori, Oscar M. Stafsudd, and Bahram Jalali. *Nonlinear absorption in silicon and the prospects of mid-infrared silicon Raman lasers*. Physica Status Solidi (a), 203(5):R38–R40, April 2006.

[15] Q. Lin, T. J. Johnson, R. Perahia, C. P. Michael, and O. J. Painter. *A proposal for highly tunable optical parametric oscillation in silicon micro-resonators*. Optics Express, 16(14):10596, July 2008.

[16] J I Dadap, N C Panoiu, Xiaogang Chen, I-Wei Hsieh, Xiaoping Liu, Cheng-Yun Chou, E Dulkeith, S J McNab, Fengnian Xia, W M J Green, L Sekaric, Y a Vlasov, and R M Osgood. *Nonlinear-optical phase modification in dispersion-engineered Si photonic wires.* Optics Express, 16(2):1280–99, January 2008.

[17] Xiaoping Liu, Jeffrey B Driscoll, Jerry I Dadap, Richard M Osgood, Solomon Assefa, Yurii a Vlasov, and William M J Green. *Self-phase modulation and nonlinear loss in silicon nanophotonic wires near the mid-infrared two-photon absorption edge.* Optics Express, 19(8):7778–89, April 2011.

[18] Michael R Lamont, Barry Luther-Davies, Duk-Yong Choi, Steve Madden, and Benjamin J Eggleton. *Supercontinuum generation in dispersion engineered highly nonlinear (gamma = 10 /W/m) As2S3) chalcogenide planar waveguide.* Optics Express, 16(19):14938–44, September 2008.

[19] Bart Kuyken, Xiaoping Liu, Richard M Osgood, Roel Baets, Günther Roelkens, and William M J Green. *Mid-infrared to telecom-band supercontinuum generation in highly nonlinear silicon-on-insulator wire waveguides.* Optics Express, 19(21):20172–81, October 2011.

[20] Richard a Soref, Stephen J Emelett, and Walter R Buchwald. *Silicon waveguided components for the long-wave infrared region*. Journal of Optics A: Pure and Applied Optics, 8(10):840–848, October 2006.

[21] Goran Z Mashanovich, Milan M Milošević, Milos Nedeljkovic, Nathan Owens, Boqian Xiong, Ee Jin Teo, and Youfang Hu. *Low loss silicon waveguides for the mid-infrared.* Optics Express, 19(8):7112–9, April 2011.

[22] Xiaoping Liu, Richard M. Osgood, Yurii a. Vlasov, and William M. J. Green. *Mid-infrared optical parametric amplifier using silicon nanophotonic waveguides*. Nature Photonics, 4(8):557–560, May 2010.

4

Supercontinuum generation in silicon

This chapter discusses the process of supercontinuum generation. First, the process of supercontinuum is explained. Next, supercontinuum generation in silicon waveguides is discussed. Experimental data shows that a broadband supercontinuum can be generated in a short silicon waveguide centered around a wavelength of $\approx$ 2100 nm, extending over more than 1000 nm. The chapter ends with an outlook which discusses some experimental results of supercontinuum generation at a wavelength of 3000 nm as well as simulations describing how an even more broadband supercontinuum can be obtained. All the simulations in the chapter are based on the split step code available and discussed in [1].

4.1 Introduction

4.1.1 Supercontinuum generation

Nonlinear interactions can generate new optical frequencies or broaden optical pulses spectrally through the process of self phase modulation. In this paragraph, supercontinuum generation, the dramatic broadening of narrow band pulses to yield a broadband spectrally continuous output is discussed. Supercontinuum light sources can be much brighter and more broadband than other broadband light sources, while being spatially single mode as can be seen on figure 4.1 and have found numerous applications in the field of spectroscopy [2]. In a telecommunications context, the spectral slicing of broadband supercontinuum spectra has also been proposed as a simple way to create multi wavelength optical sources for

dense wavelength division multiplexing applications [3]. The introduction of photonic crystal fibers was a breakthrough in the field of supercontinuum generation. Specific properties of these waveguides such as broadband single mode operation, tight optical confinement leading to higher power densities and the ability to engineer the group velocity dispersion [4] have contributed to this breakthrough and have enabled the commercialization of these sources [1]. To understand the process of supercontinuum generation it is useful to go look into some examples of successful supercontinuum generation in photonic crystal fibers. Since the generation of a supercontinuum is fundamentally different for femtosecond pulses (100 fs) and longer pulses, both these cases are discussed.

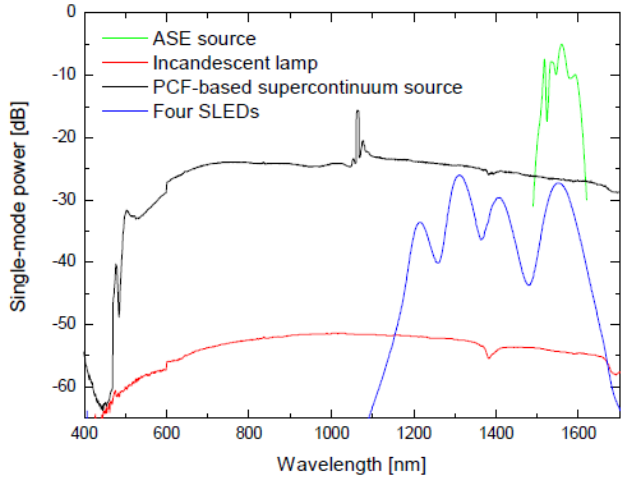

Figure 4.1: The output spectrum of different kinds of broadband light sources. A supercontinuum generated in a photonic crystal fiber is a very bright and broadband source compared to other solutions. Figure from [5]

4.1.1.1 Supercontinuum generation by pumping waveguides with ultrashort (fs) pulses

Solitons are special pulses which are known to preserve their shape when traveling through a nonlinear medium [6]. For a fundamental soliton the acquired nonlinear phase shift experienced by the pulse balances the linear phase shift it acquires because of the (anomalous) dispersion of the waveguide. However, it can be shown that higher order solitons also exist and it can be shown that these will propagate in a periodic manner in a nonlinear medium with second order anomalous dispersion [7]. This can be seen in figure 4.2. The graph has two panels, on the left the spectrum of the pulse can be seen as a function of propagation distance in the fiber and on the right panel its temporal profile can be seen as a function

of propagation distance. When pumping a fiber or waveguide with high power femtosecond pulses these pulses will propagate throughout the fiber or waveguide as if they are higher order solitons. It can be shown however, that higher order solitons are not stable when there is some perturbation such as additional third order dispersion or Raman scattering. When this is the case the higher order soliton will break up into fundamental solitons as can be seen in figure 4.3, where a third order soliton is propagating through a nonlinear photonic crystal fiber when there is higher order dispersion. After a propagation over several centimeters the soliton breaks into three fundamental solitons. It can be shown [7] that the so called fission length is given by $L_{fiss} = \frac{L_D}{N}$, here is $L_D = \frac{T_0^2}{\beta_2}$ the dispersion length of the soliton with pulse duration T_0 in a medium with group velocity dispersion β_2 and $N = \sqrt{L_D \gamma P}$ the soliton number of the soliton with peak power P. This can be seen in the time domain, but also in the frequency domain in figure 4.3. Every soliton in the time domain is a pulse, and has a specific frequency spectrum and is thus represented by a pulse in the frequency domain as well. These three solitons all have different central frequencies and travel for this at a different speed. This will introduce a delay between the pulses as can be seen in the time domain. In the frequency domain the solitons are further frequency shifted due to Raman scattering. The soliton spectrum is so broadband that the Stokes lines from the blue components of the same soliton are within the same soliton spectrum. For this reason blue light in a specific soliton will get converted to red light in the same soliton. This process will redshift the soliton through propagation and can be used as a way to extend a continuum to the red. The combination of these effects can be so dramatic that it can lead to a broad supercontinuum as can be seen in figure 4.4 where the fiber is pumped close to the zero dispersion wavelength. It can also be seen that the break up happens when the pulse is at the point where it is temporally very wide.

4.1.1.2 Supercontinuum generation from short (ps) pulses

Although picosecond pulses can be seen as very high order solitons they will not fall apart in multiple fundamental solitons because their oscillation period (and thus the distance to get to the point where the soliton is long in the time domain) is very long, in most cases longer than the length of the photonic crystal fiber. In this case another process will cause the generation of the supercontinuum. Next to some Raman amplification of noise it is merely modulation instability and four wave mixing that are the main causes of the broadening [7]. In fact it has been shown that for the characteristic length of modulation instability, the nonlinear length $L_{NL} = \frac{1}{\gamma P}$ for a pulse with peak power P propagating in a nonlinear waveguide with nonlinear parameter γ has to be much smaller than the fission length L_{fiss} in order for the supercontinuum to be based on modulation instability:

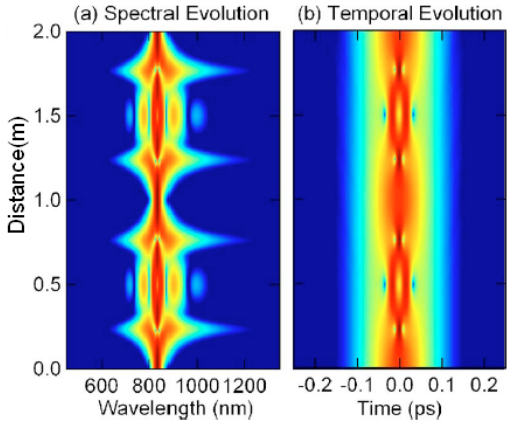

Figure 4.2: Periodic evolution of the spectral and temporal characteristics of the higher-order (N=3) soliton in a nonlinear material pumped in the anomalous regime. The peak power of the pulse is 1250 W, its duration is 200 fs, while the nonlinearity of the photonic crystal fiber is assumed to be 0.11 $W^{-1}m^{-1}$. The length unit has been normalized to the period of the higher order soliton. Figure from [7]

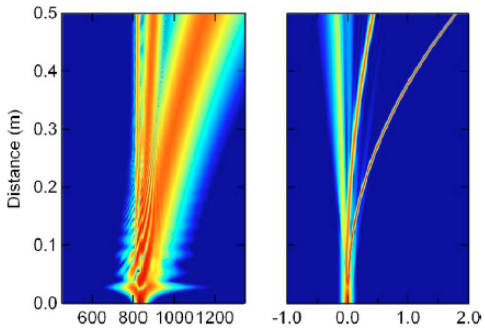

Figure 4.3: Results from numerical simulations showing spectral and temporal evolution for Raman induced fission of an incident N=3 soliton. The pulse properties are similar as in the previous figure. Figure from [7]

$$L_{NL} << L_{fiss} \tag{4.1}$$

With the help of the definition of these quantities this means that the soliton number needs to be large. More specifically it has been shown [7] that the soliton number needs to be larger than 16, to get in the regime where modulation instability is dominant. When generating a supercontinuum from long pulses, it is very important to have some small anomalous dispersion at the pump frequency to make sure that the sidebands that are generated through modulation instability are

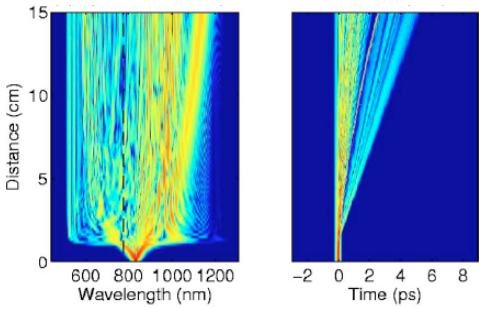

Figure 4.4: Results from numerical simulations showing density plots of the SC spectral and temporal evolution generated by pulses with duration 100 fs FWHM. The input pulse peak power is 10 kW and is centered at a wavelength of 835 nm. The dashed line shows the fiber ZDW. The nonlinear parameter is assumed to be 0.11/Wm. Figure from [7]

spectrally broad and far from the pump (distance to the pump frequency is given by $\Delta\omega = \sqrt{\frac{2\gamma P}{\beta}}$, see section 3.1). Figure 4.5 shows picosecond pulses generating a supercontinuum by first generating sidebands after propagating for 10 cm in the photonic crystal fiber through the amplification of noise. These sidebands generate, through four wave mixing with the pump, new side bands after a propagation of 20 cm and this process is continued through further propagation. Most commercially available supercontinuum sources generate the continuum by spectrally broadening picosecond pulses in a dispersion engineered photonic crystal fiber. These sources are inherently noisy and the spectrum of the supercontinuum generated by subsequent pulses differs because it is highly dependent on the background noise [8].

4.2 Supercontinuum generation in other planar waveguide circuits

In this section the state of the art of supercontinuum generation in planar waveguide circuits is discussed.

4.2.1 Chalcogenide planar waveguide circuits

There have been several demonstrations of supercontinuum generation in chalcogenide planar waveguides. In 2008 Lamont et al. [9] demonstrated the generation of a supercontinuum in a 6 cm As_2S_3 chalcogenide waveguide with a nonlinear parameter of 10 $W^{-1}m^{-1}$. The supercontinuum was generated by pumping the low anomalous dispersive waveguide with 610 fs pulses with a peak power of 68 W. The -30 dB bandwidth of the generated supercontinuum extended 750 nm around

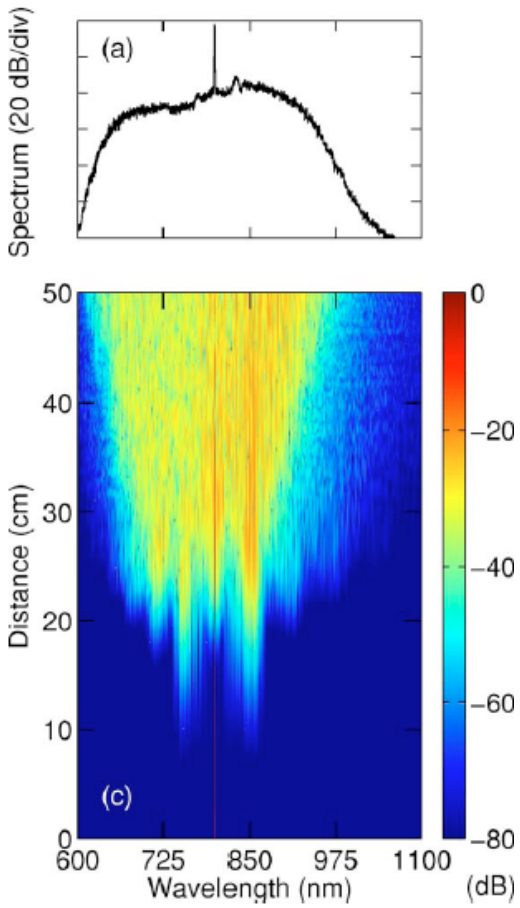

Figure 4.5: SC obtained with 20 ps pulses of 500 W peak power at a 800 nm pump wavelength in a 50-cm-long fiber. Figure from [7]

1550 nm. As a result of the combination of low group velocity dispersion and the relatively long pulses used in the waveguide the main process driving the process was modulation instability. In 2012 Gai et al. [10] demonstrated a supercontinuum extending from 2900 nm up to 4200 nm by pumping a 6.6 cm waveguide by 1.7 kW peak power, 7.5 ps long pulses. The supercontinuum was limited at the long wavelength side by absorption in the waveguides' silica substrate as well as by OH contamination in the chalcogenide.

4.2.2 Silicon nitride waveguide circuits

An 1.6 octave spanning supercontinuum was demonstrated in 2012 by Halir et al. [11] by pumping a 4.3 cm silicon nitride waveguide by 200 fs pulses with a peak power of about 800 W at a central wavelength of 1300 nm.

4.2.3 High index doped glass waveguide circuits

By pumping around 1300 nm as well as around 1550 nm Duchesne et al [12] demonstrated in 2010 a supercontinuum in a 35 cm long doped glass waveguide. The generated supercontinua extended over about 300 nm and 500 nm (-30 dB bandwidth) around these pump wavelengths respectively. The 100 fs long pump pulses, had a peak power of 1700 W.

4.2.4 Lithium Niobate waveguides

It is worth noting that in periodically poled lithium niobate waveguides broadband supercontinuum generation has been reported by Phillips et al. in 2011 [13]. The -40 dB bandwidth spanned from 1350 to 2800 nm when the 18.5 mm long waveguide was pumped by 100 fs pulses having a peak power of 70 kW and centered at 1950 nm.

4.3 Supercontinuum generation in silicon waveguides

A number of theoretical papers have suggested the idea of the generation of a supercontinuum in a silicon photonic waveguide as early as 2007 [14]. Numerically it was suggested that a supercontinuum spanning from 1250 nm up to 1730 nm could be obtained in a 1.2 cm silicon wire when it is pumped by 50 fs pulses with a peak power of 25 W. In 2007, a supercontinuum was demonstrated in a silicon waveguide by pumping a 4.7 mm silicon waveguide [15]. The resulting supercontinuum is shown in figure 4.6. The supercontinuum spans from 1100 nm to 1450 nm when the waveguide is pumped with 1 W peak power, 100 fs long pulses centered at 1310 nm. It seemed impossible to increase the bandwidth more by using more powerful pulses due to the high nonlinear absorption in the silicon waveguides. Using pump pulses centered at longer wavelengths it is possible to reduce the nonlinear absorption enormously and have a more broadband supercontinuum. This approach is followed in this work.

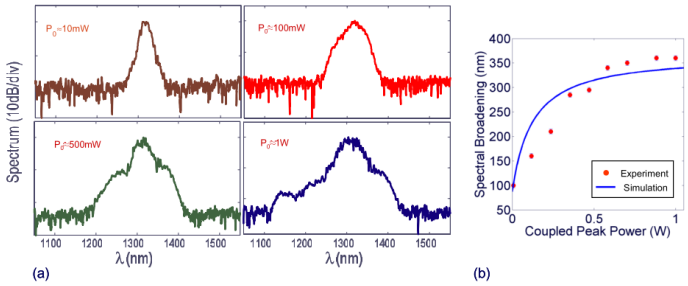

Figure 4.6: The supercontinuum obtained in [15]. Figure a) shows the pump power dependence of the output spectra while b) is showing the spectral broadening as a function of the coupled peak power. The bandwidth of the supercontinuum is limited to 350 nm or 0.56 octave

4.3.1 Supercontinuum generation in silicon-on-insulator waveguides at longer wavelengths

4.3.1.1 Considerations for broadband supercontinuum generation in a silicon waveguide

The pulsed source that is available for the experiments is a Coherent MIRA optical parametric oscillator which generates 2 ps pulses at a repetition rate of 76 MHz. The source is tunable from about 1800 nm to about 2300 nm. The source is coupled to a single mode fiber. The peak power of the pulses in the fiber is about 150-200 W. Since the coupling loss to a silicon wire waveguide at facet of a chip is about 7-10dB, it allows one to have 20 W peak power pulses on a chip. Since the nonlinear parameter of a sub-micron silicon waveguides is about 100 $W^{-1}m^{-1}$ the soliton number of these pulses is > 100 when we assume that the magnitude of the dispersion of the waveguide is lower than 1 ps^2/m. As discussed in the introduction this means that the process dominating the generation of the supercontinuum will be modulation instability and cascaded four wave mixing. To generate a broadband supercontinuum, it is good to have a low anomalous dispersive waveguide such that the offset frequency of the bands to the pump frequency where phase matching is achieved (see section 3.1), given by $\Delta\omega = \sqrt{\frac{2\gamma P}{\beta_2}}$, is large. The total dispersion (including both the material as the geometrical dispersion) of deeply etched waveguides with an air cladding and a height of 220 nm and a varying width were simulated in Fimmwave ©. The 220 nm height is a fixed process parameter, such that the width was the only degree of freedom in the design. The simulated dispersion of the long wavelength silicon-on-insulator waveguides is shown in figure 4.7. As can be seen in figure 4.7, the dispersion of a 900 nm waveguide is low, while at the same time being anomalous over a broad wavelength region. The anomalous dispersion in a broad region allows for efficient

cascaded four wave mixing of sidebands generated by modulation instability, extending the supercontinuum further. It was this waveguide which was chosen to generate a supercontinuum.

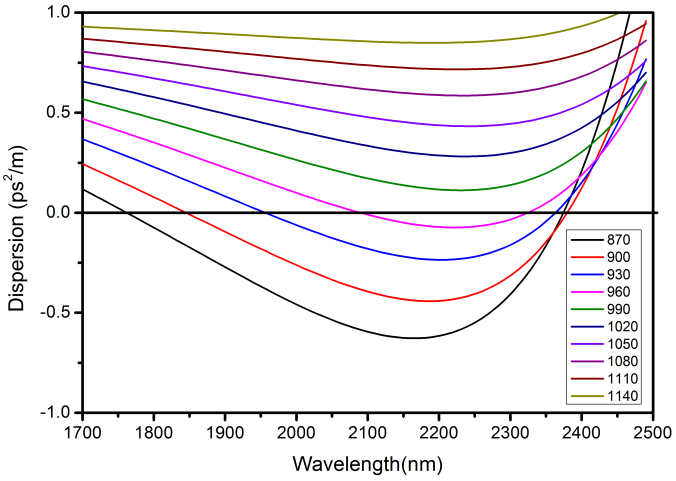

Figure 4.7: The simulated dispersion of waveguides with a varying width as a function of the wavelength. The waveguides have a height of 220 nm, are deeply etched and have an air cladding.

4.3.1.2 Results

This section summarizes the results of [16]. In a 2 cm long, 900 nm wide waveguide the generated supercontinuum spanned from 1535 nm to 2525 nm when it was pumped with 2 ps pulses centered at 2120 nm with a peak power of 12.7 W. The supercontinuum is shown in figure 4.8. It is useful to look more closely to the output spectrum of the pulses after they have passed through the waveguide as a function of input peak power. From these spectra it is clear that the supercontinuum as expected is generated through the amplification of background noise. The waveguide is pumped in the anomalous region so there is phase matching in a band close to the pump wavelength, where noise gets amplified (labeled MI (1) in the graph). Further from the pump wavelength there is an additional band where phase matching is achieved due to higher order phase matching, as discussed in chapter 3.1, this band is labeled MI(2) in the graph. At a wavelength around 2400 nm noise gets amplified by the Raman effect. To confirm that the light is generated by amplification, an additional experiment was performed where the supercontinuum was probed by a continuous wave laser. The amplification as a function of wavelength can be seen in figure 4.9.

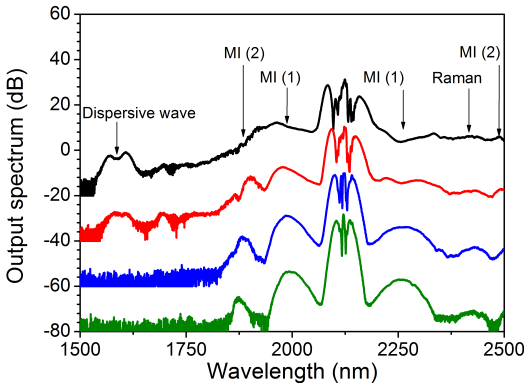

Figure 4.8: Measured output spectrum for increasing values of coupled input peak power: 3.1 W (green), 4.3 W (blue), 7.9 W (red) and 12.7 W (black). The spectra are vertically offset by multiples of 20 dB for clarity.

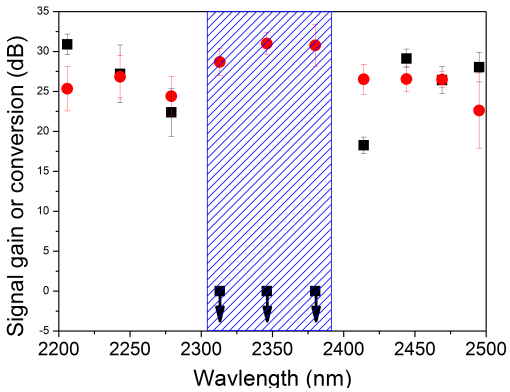

Figure 4.9: On-chip signal gain (red dots) and wavelength conversion efficiency (black squares) at a peak power of 12.7 W as measured through seeding the supercontinuum at various wavelengths. The hatched areas label the pumps Raman Stokes and matching anti-Stokes bands.

4.3.2 Future work

There are two possible routes to extend a supercontinuum generated in a silicon waveguide. The first one is to use shorter fs pulses, the other is to use waveguides which have a small anomalous group velocity dispersion over a longer wavelength range and which do not have substrate leakage at longer wavelengths. These two routes are briefly discussed in the following section. It is of course also possible to combine these two approaches.

4.3.2.1 Supercontinuum generation in silicon waveguides with shorter pulses

As discussed in section 4.1, a supercontinuum generated by short pulses is dominated by soliton fission when the soliton number of the input pulses is smaller than 16. These supercontinua are not generated by the amplification of background noise and are much more coherent than the supercontinua generated by the amplification of background noise via the process of modulation instability [7]. From pulse to pulse the generated spectra are very similar since the soliton fission is not noise driven. For example when short 150 fs pulses with a peak power of 5W and 10 W in a standard 900 nm wide 220 nm high waveguide are injected the soliton number is given by

$$N = \sqrt{\frac{\gamma P \tau^2}{\beta_2}} \cong 3 - 5 \tag{4.2}$$

when assuming a nonlinear parameter of $120/W/m$ and a group velocity dispersion $\beta_2 = -0.5ps^2/m$. Figure 4.10 shows the simulation of a supercontinuum in a 2 cm long, 900 nm wide photonic wire when pumped at 2200 nm by 150 fs pulses with a peak power of 5 W. In the simulation it is assumed that there was no nonlinear absorption. This is a reasonable assumption because of the limited peak powers. For example even for a peak power of 10W in an silicon photonic wire waveguide with an area of about $0.3um^2$ the intensity is about 3.3 GW/cm^2. The three photon absorption coefficient in silicon is estimated to be 0.025 cm^3/GW^2 [17], which means that the absorption is only 0.2 /cm at the highest peak power. Figure 4.11 shows the supercontinuum generated when the same waveguide is pumped with pulses with a peak power of 10W. In both simulations, the nonlinear parameter was assumed to be 120 $W^{-1}m^{-1}$, while the dispersion was assumed to be $\beta_2 = -0.44ps^2/m$,$\beta_3 = -5.5 \times 10^{-4}ps^3/m$,$\beta_4 = 1.12 \times 10^{-4}ps^4/m$. These dispersion coefficients are found by simulating the propagation constant β as a function of frequency and getting the derivatives from a polynomial fit to the simulated curve. The linear loss of the waveguide was assumed to be $0.6dB/cm$. This assumption is not valid for wavelengths longer than $\approx$ 2900 nm (see figure 2.2), where the substrate leakage becomes large. However this could be overcome by under etching the waveguides to increase the confinement of the mode, and as such reduce the substrate loss. As can be seen on the figures, a broadband supercontinuum is generated through the process of soliton fission. The fission length can be calculated as [7]

$$L_{Fiss} = \frac{L_D}{N} = 5.9mm(5W), 4.1mm(10W). \tag{4.3}$$

Indeed as seen on the figure, soliton fission occurs for the 5W pulses launched in the waveguide after a propagating for 6 mm, while the fission is clearly visible at around 4 mm for the 10 W pulses. The generated supercontinuum is in both cases

octave spanning and the broadening could in principle be used to do f-2f [18] self-referencing for a fs pulsed source. We can conclude that octave spanning supercontinua can be generated with very low peak power pulses.

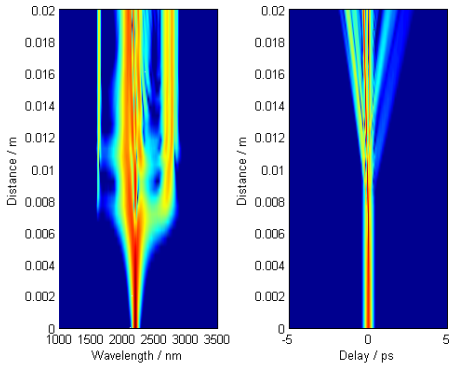

Figure 4.10: The process of supercontinuum generation for 5 W peak power, 150 fs pulses in a silicon photonic wire waveguide as a function of propagation length. The left panel shows the spectrum as a function of length, while the right panel shows the pulse shape as a function of propagation length.

4.3.2.2 Silicon-on-insulator waveguides for the mid-infrared wavelength range

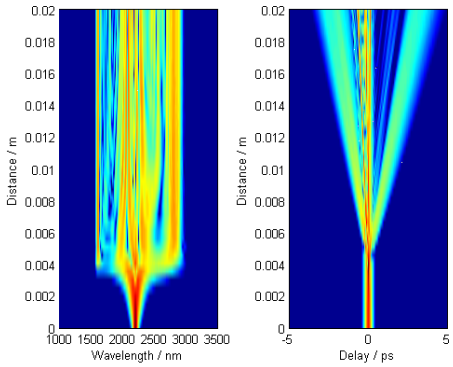

Figure 4.11: The process of supercontinuum generation for 10 W peak power 150 fs pulses in a silicon photonic wire waveguide as a function of propagation length. The left panel shows the spectrum as a function of length, while the right panel shows the pulse as a function of propagation length.

The substrate leakage increases the loss at long wavelengths for waveguides with a height of 220 nm at around 2900 nm (see figure 2.2). To extend the super-

continuum to longer wavelengths another set of waveguides with lower substrate leakage are needed. A new set of air clad waveguides with a height of 400 nm was fabricated. A cross section SEM of a fabricated waveguide is shown in figure 4.12. Although the oxide buffer layer was 2 um, the substrate leakage is very low up to 4000 nm (see figure 2.3). Additionally these waveguides have a very low anomalous dispersion at long wavelengths which allows them to be used for the generation of a supercontinuum at longer wavelengths. Some initial measurements were performed during a visit in February 2013 of the Australian National University, in a collaboration with the group of Prof. Barry Luther Davies. At the time of writing additional measurements are still performed, however some preliminary results are discussed in this section.

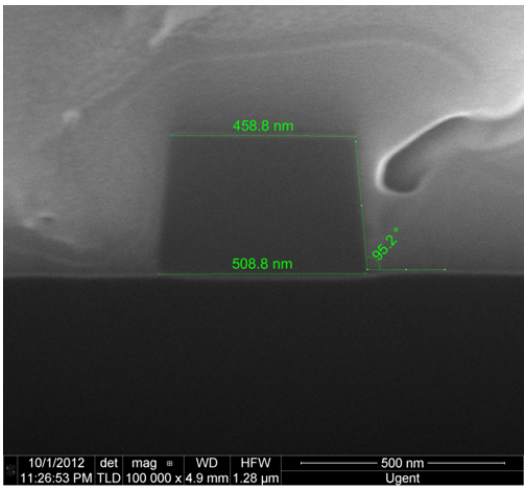

Figure 4.12: A cross section of a 400 nm high, 500 nm wide waveguide resting on a silicon oxide substrate. The side wall angle is almost 90 degrees. The clouds surrounding the waveguide are parts of the platina used while making the cross section

Experimental setup. The group velocity dispersion of the 1850 nm wide waveguide with a height of 400 nm and an air cladding is plotted in figure 4.13. The nonlinear parameter was estimated to be 15 /Wm at 3500 nm. In the experiment, the 1850 nm wide waveguide was tapered to a 8 μm wide waveguide at the facets. Coupling in and out of the chip was done with molded high NA (NA=0.85) chalcogenide lenses. The light was generated by an optical parametric amplifier (details can be found in [19]). The OPA consisted out of a PPLN crystal containing a graded grating and it is pumped by 18 ps long pulses from a modelocked$Nd:YVO_4$ laser and seeded with CW emission from a Photonetics Tunics Purity laser tunable from 1450 to 1590 nm. By simultaneously tuning the seed

laser and the grating period, a mid-IR output between 3000 and 4000 nm could be generated in transform-limited pulses with a duration of 7.5 ps and a repetition rate of 1.5 MHz. The insertion loss of a 1850 nm wide waveguide is plotted as a function of wavelength for low peak powers in figure 4.14. Absorption dips are visible, probably resulting from contaminants on top of the waveguide.

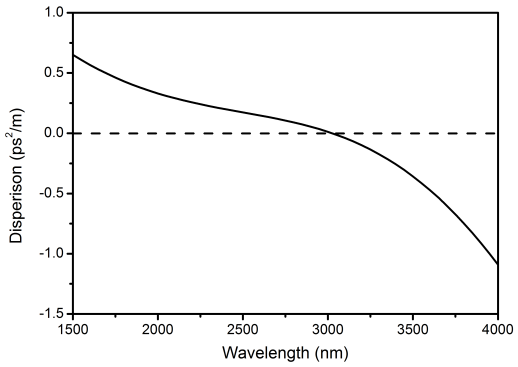

Figure 4.13: The group velocity dispersion of the 1850 nm wide waveguide. The group velocity dispersion is very flat over a broad wavelength range while the zero dispersion wavelength is around 3100 nm.

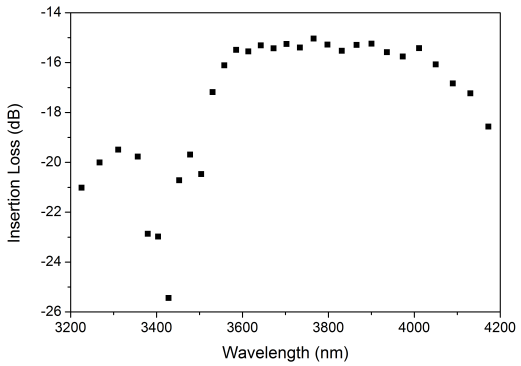

Figure 4.14: The transmission of a 1850 nm, 1 cm long wide waveguide as a function of the wavelength.

Supercontinuum generation in the waveguide. The 1 cm long, 1850 nm wide waveguide was pumped both at 3220 nm and 3550 nm at high peak powers. The resulting spectra are shown in figure 4.15 and 4.16. As can be seen in the figures, the best result is obtained by pumping the 1 cm long waveguide at 3550 nm. In this region the insertion loss of the waveguide was lower while the dispersion at

this wavelength is rather low. However, at highest peak power, the output spectrum is not a satisfactory supercontinuum. The amplification of the background noise can be seen as the driving factor and it is the onset to a supercontinuum. However, at higher peak powers the facets of the waveguides get burned. It is believed that by using longer waveguides where a longer interaction length is available a good supercontinuum can be obtained.

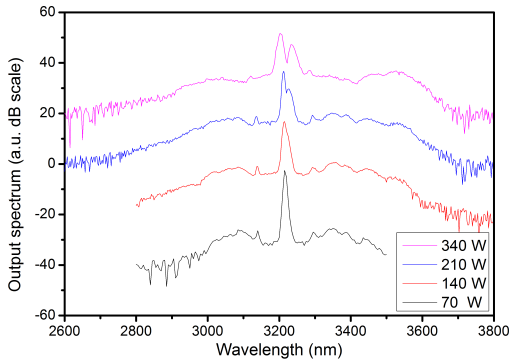

Figure 4.15: The output spectra of the 1 cm long, 1850 nm wide waveguide as a function of peak power when pumped at 3220 nm. At higher peak powers the facets of the waveguides got damaged.

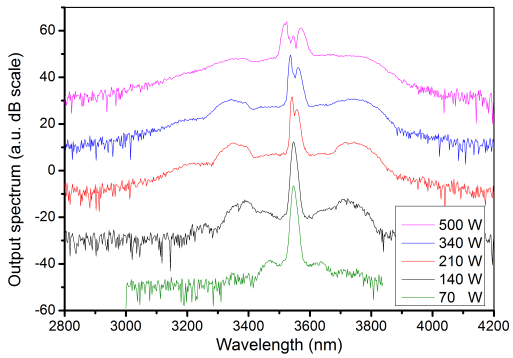

Figure 4.16: The output spectra of the 1 cm long, 1850 nm wide waveguide as a function of peak power when pumped at 3550 nm. At higher peak powers the facets of the waveguides got damaged.

Additional simulations for short pulse supercontinuum generation in long wavelength waveguides To conclude the chapter some additional simulations have been done when the 1850 nm wide waveguide would get pumped at 3300 nm

with short pulses (150 fs). A nonlinear parameter of 15 $W^{-1}m^{-1}$ was assumed while the peak power of the pulses was assumed to be 80 W, while the dispersion coefficients are assumed to be $\beta_2 = -0.13 \times ps^2/m$, $\beta_3 = 3.9 \times 10^{-4} ps^3/m$, $\beta_4 = 1.6 \times 10^{-4} ps^4/m$. These values are found by simulating the propagation constant of the 1850 nm wide waveguide as a function of frequency. The linear loss is assumed to be 0.6 dB/cm The waveguide becomes very lossy at wavelengths longer than 4000 nm, this is not incorporate in the simulations and is outside of the scope of this work. Therefor, the supercontinuum will in reality not extend much further than 4000 nm. This simulation is merely a demonstration of long wavelength supercontinuum generation. However by under etching a silicon waveguide [20] and thus removing the absorbing oxide bottom, it is theoretically possible to achieve a wide supercontinuum beyond 4000 nm.

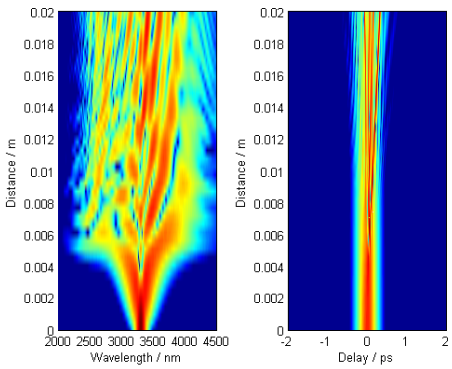

Figure 4.17: The simulated output spectra of the 400nm wide and 1850 nm wide waveguide.

4.4 Conclusion

In this chapter experimental results demonstrate that a broadband supercontinuum can be generated in a silicon waveguide at relatively low powers. Several simulations show that it is possible to generate an octave spanning supercontinuum in a silicon waveguide when short (150 fs) pulses are used.

4.5 Mid-infrared to telecom-band supercontinuum generation in highly nonlinear silicon-on-insulator wire waveguides

The content of this section was published in Optics Express [16]

The silicon photonic wires used are fabricated in a CMOS pilot line, using 200 mm SOI wafers consisting of a 220 nm silicon waveguide layer on a 2 μm buried oxide layer. The wires are 900 nm wide with no top cladding, as shown in the inset of Figure 4.18. The strong optical confinement resulting from the upper air cladding results in a high effective nonlinearity parameter, and also contributes to anomalous dispersion in the mid-IR. By averaging the nonlinear susceptibility of bulk Si over the electric field of the fundamental TE-polarized waveguide mode, the real part of the nonlinearity parameter is estimated to be γ_{Re} = 150 $(Wm)^{-1}$ [11]. The group velocity dispersion β_2 of the fundamental TE mode is calculated using a commercial finite element mode solver (RSoft FemSim). As shown in Figure 4.18, the wire exhibits anomalous dispersion ($\beta_2 < 0$) between 1810 nm and 2410 nm.

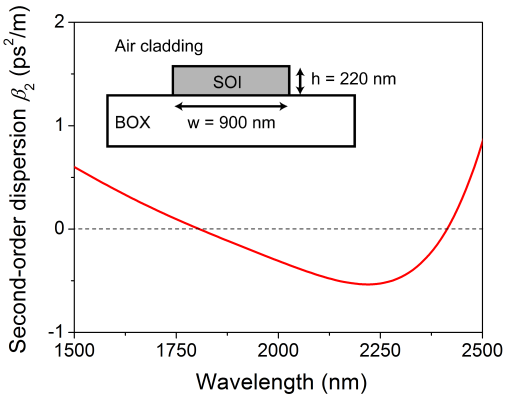

Figure 4.18: Group velocity dispersion of the silicon wire waveguide as a function of the wavelength, exhibiting anomalous dispersion ($\beta_2 < 0$) between 1810 nm and 2410 nm. The inset shows the fabricated wire waveguide dimensions.

The supercontinuum generation experiments are conducted using a picosecond pulse train at a center wavelength of 2120 nm as the pump (Coherent Mira-OPO, FWHM = 2 ps, repetition rate = 76 MHz). Using a cut back technique the TE mode waveguide propagation loss is found to be approximately 2.5 dB/cm, across the mid-IR wavelength range from 2050-2450 nm, as well as at wavelengths near 1550 nm. The waveguide used in the supercontinuum experiments is 2 cm in length. The coupling loss at the cleaved input/output facets is 10 dB/facet. The

spectrum at the waveguide output is characterized with a mid-IR optical spectrum analyzer (OSA) at a 1 nm resolution.

Figure 4.19 illustrates the evolution of the waveguide output spectrum as the input coupled peak pump power is gradually increased from 3.1 W (green trace) to 12.7 W (black trace). These spectra reveal that a number of different nonlinear processes ultimately combine to produce the broadband supercontinuum. At an input power of 3.1 W, a series of sidebands are generated in the vicinity of the pump at 2120 nm. Closest to the pump, two broad sidebands (labeled as MI(1)) are generated near wavelengths of 1990 nm and 2250 nm. Further away from the pump, a pair of narrowband peaks (labeled as MI(2)) appear at wavelengths of 1870 nm and approximately 2510 nm. Both the broad and narrow sideband pairs originate from modulation instability [21, 22], i.e. the amplification of background noise at wavelengths for which the phase matching condition in Eq. below is satisfied.

$$-(\beta_2 \Delta\omega^2 + \frac{\beta_4 \Delta\omega^4}{12}) = 2\gamma P \tag{4.4}$$

Here, β_2 and β_4 are the second- and fourth-order waveguide dispersion respectively, $\Delta\omega$ is the detuning of the idler and signal from the pump, $Re(\gamma)$ is the real part of the effective nonlinearity parameter, and P is the peak pump power. The modulation instability sidebands appear where the linear phase mismatch and the nonlinear phase mismatch cancel one another. Finally, Figure 4.19 shows that a Raman Stokes peak appears near 2400 nm, red-shifted by ≈15.6 THz from the pump as expected [23].

Even at the lowest input power, the pump pulse train's spectrum is broadened significantly by self phase modulation (SPM), as illustrated by the numerous interference fringes appearing near 2120 nm. In turn, this causes associated broadening of the sidebands generated through modulation instability and Raman scattering. When the coupled peak pump power is increased to 4.3 W, the spectral intensity of the generated sidebands is observed to increase with respect to the pump, and the degree of pump and sideband broadening increases. At a pump power of 7.9 W, several new spectral components are observed, peaked near 1700 nm and 1600 nm respectively. The term at 1700 nm is generated through cascaded four-wave mixing (FWM), where the original MI(2) peak at 1890 nm serves as the degenerate pump and the input pulse at 2120 nm acts as the signal. The peak around 1600 nm is believed to be the result of Cherenkov radiation referred to as dispersive wave generation. At first sight this is unexpected when we compare the different length scales in our experiment. The nonlinear length is approximately L_{nl} = 500 μm at a coupled peak power of 12.7 W, whereas the soliton fission length is 6.3 cm [7], significantly longer than the wire waveguide's length. Therefore, generation of a dispersive wave through soliton fission is unlikely. However, recent research has

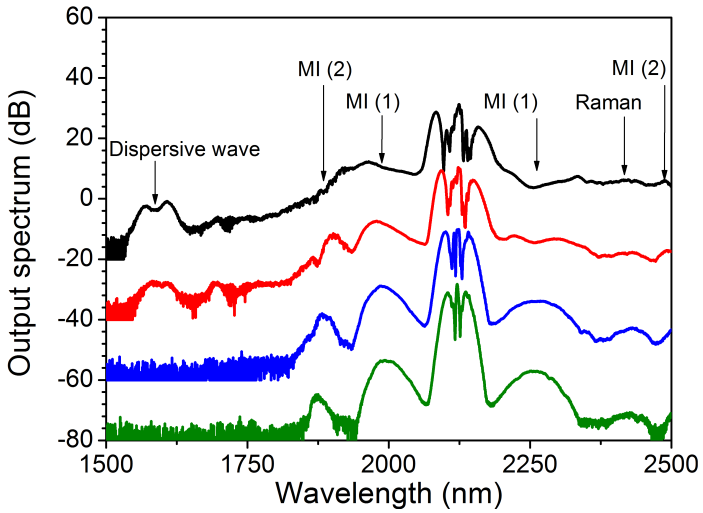

Figure 4.19: Measured output spectrum for increasing values of coupled input peak power: 3.1 W (green), 4.3 W (blue), 7.9 W (red) and 12.7 W (black). The spectra are vertically offset by multiples of 20 dB for clarity.

shown that in the long pulse regime where modulation instability is the main driving force behind supercontinuum generation, dispersive waves can also be generated through the simultaneous formation of pre-solitonic breathers along the pump pulse. There are several facts supporting this finding. First, the 1600 nm peak lies within the normal dispersion regime of the silicon wire, as expected for the generation of dispersive waves. In addition, there is no combination of the observed modulation instability and/or Raman peaks that can generate the 1600 nm component through cascaded FWM. Moreover, seeding the supercontinuum using a CW laser at 1600 nm does not reveal any parametric gain at this wavelength. This lack of gain excludes the possibility that the 1600 nm component is generated through the process of modulation instability phase-matched through even higher-order dispersion terms (e.g. β_6, β_8), which become important at large detuning from the pump. Finally, at the highest pump power of 12.7 W, Figure 4.19 shows that the spectral broadening of all generated peaks leads to the merging of the MI(1), MI(2), and Raman peaks, and to increased flatness of the output spectrum on both the red and blue sides of the pump. Under these conditions, the supercontinuum output from the mid-IR pumped SOI wire waveguide extends from 1540 nm to beyond 2500 nm, the maximum wavelength resolved by the OSA used. To characterize the presence of any additional spectral components beyond 2500 nm, a Fourier Transform Infrared spectrometer (FTIR) equipped with a liquid nitrogen-cooled InAs detector is used. As shown in Figure 4.20, the FTIR measurements

reveal that the supercontinuum extends to a maximum wavelength of 2525 nm on the red side of the pump. Generation of light at longer wavelengths through modulation instability is not expected because the phase-matching condition in Eq. (1) has no solutions beyond 2525 nm, even when higher-order dispersion terms of the wire waveguide are taken into account (discussed below in Figure 4.23). While additional weak spectral components could potentially be generated by cascaded FWM, these are not likely to be visible due to the high noise floor of the InAs detector, as well as the limited 38 dB dynamic range of the FTIR A/D converter.

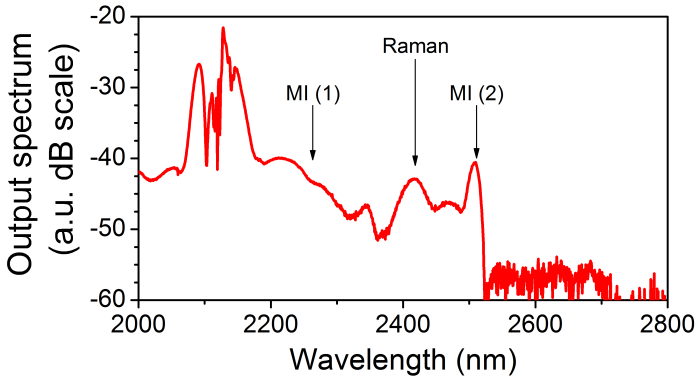

Figure 4.20: Output spectrum on the red side of the pump, as measured by FTIR at a coupled input peak power of 12.7 W.

The basic processes contributing to the observed broadband generation can be further understood by characterizing the output spectrum while seeding the supercontinuum at several different spectral locations, as shown in Figure 4.21. This is accomplished by combining the high-power pump pulse train with a weak ($<$ 0.2 mW) mid-IR CW tunable laser. By comparing the green trace, seeded at 2415 nm close to the Raman Stokes wavelength, with the blue reference curve, which illustrates the unperturbed supercontinuum, the injected seed signal can be seen to experience stimulated Raman amplification at the output of the waveguide. The amplification is demonstrated by the appearance of a strong pedestal at the base of the CW seed line, which is also broadened by cross-phase modulation by the pulsed pump. The red trace, seeded at 2496 nm near the narrowband phase-matching wavelength MI(2), shows that a similar signal amplification pedestal is generated along with a wavelength-converted idler peak at approximately 1880 nm, this time via phase-matched FWM parametric amplification [24]. Moreover, through a cascaded FWM process in which the idler acts as the pump and the 2120 nm pulse train acts as the signal, a second peak at approximately 1690 nm appears.

Through analysis of several experiments in which the seed signal is tuned over the range 2200-2500 nm, the on-chip gain and conversion efficiency occurring

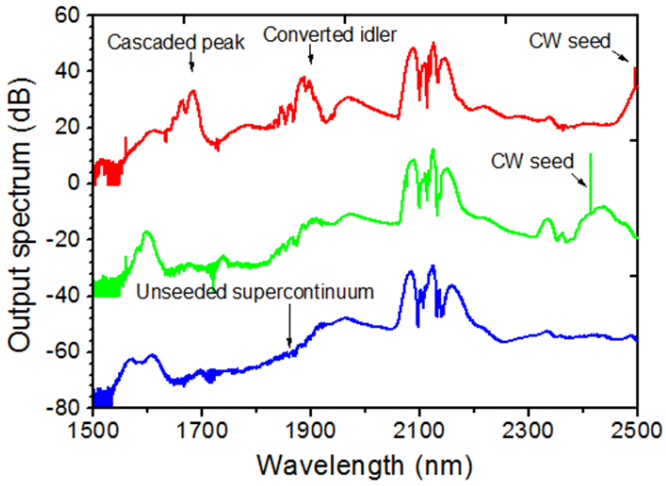

Figure 4.21: Measured output spectra obtained while seeding the supercontinuum at a wavelength of 2415 nm (green) and 2496 nm (red), using a CW mid-infrared laser. The blue curve shows the unseeded output spectrum as a reference. The coupled peak power is 12.7 W in all cases. The spectra are vertically offset by multiples of 40 dB for clarity.

across the supercontinuum are quantified in Figure 5, following the approach applied in [15]. Strong signal amplification (red circle symbols, as large as 31 dB) occurs within the pump's Raman Stokes band (hatched), centered around 2375 nm. However, the absence of wavelength conversion gain (black square symbols, less than 0 dB observed in experiment) within the associated anti-Stokes band near 1910 nm indicates that phase-matching is not preserved between the MI(1) and MI(2) peaks seen in Figure 4.21, and that Raman scattering is not coherently reinforced within the supercontinuum. In contrast, Figure 4.22 illustrates that within both the MI(1) regions (2200-2300 nm) closest to the pump and the MI(2) regions (2387-2500 nm) beyond the hatched Raman band, phase-matching leads simultaneously to efficient wavelength conversion and parametric signal gain, ranging from 18-30 dB. These observations illustrate that the supercontinuum is generated primarily through broadband amplification of noise, both with and without phase-matching. As discussed previously, this conclusion is in agreement with what one would expect from the effective optical length scales involved within the SOI wire. Because the soliton fission length is significantly longer than the length of the wire waveguide, soliton fission is unlikely to occur and the supercontinuum is predictably dominated by modulation instability and Raman scattering.

The experiments described above illustrate that in addition to contributions from Raman scattering and dispersive waves, the supercontinuum generation is largely dominated by the phase-matched process of modulation instability. Aside

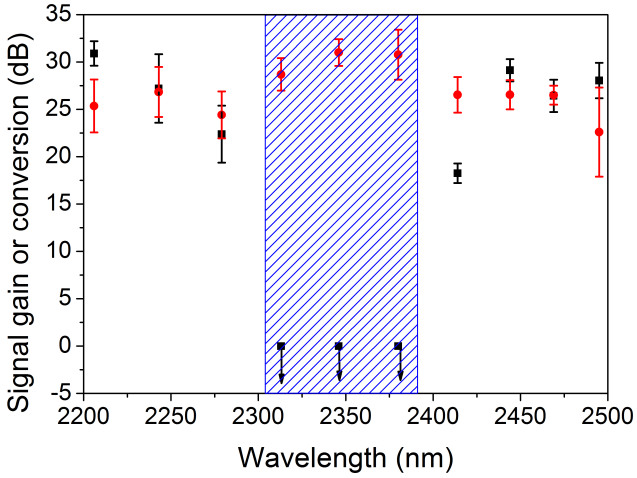

Figure 4.22: On-chip signal gain (red dots) and wavelength conversion efficiency (black squares) at a peak power of 12.7 W as measured through seeding the supercontinuum at various wavelengths. The hatched areas label the pump's Raman Stokes and matching anti-Stokes bands.

from the dispersive wave peak appearing near 1600 nm, Figure 4.19 and Figure 4.20 show that the supercontinuum bandwidth is spanned by the phase-matched MI(2) peaks near 1870 nm and 2510 nm. Therefore, in order to understand how to further increase the bandwidth and intensity of the supercontinuum, additional analysis of the wavelength-dependent phase mismatch around the pump, and the associated dispersion coefficients β_2 and β_4, is required. Although we do not have direct experimental access to the value of the linear phase mismatch Δk_{lin}, illustrates that an estimate can be generated using the nonlinear phase mismatch term $\Delta k_{nonlin} = 2Re(\gamma)P$, because the linear and nonlinear phase terms are equal and opposite in sign where efficient MI occurs. Furthermore, the detuning frequencies $\Delta\omega$ where Eq. (1) is satisfied for different values of input peak pump power can be read directly from locations of the MI peaks in Figure 4.19. The experimental nonlinear phase mismatch values can then plotted versus their respective detunings as shown in Figure 4.23. By fitting this data, an estimate of the linear phase mismatch $-\Delta k_{lin}$ around the pump is generated. However, when evaluating the nonlinear phase mismatch term 2Re(γ)P, it is important to account for the fact that the pump power decreases along the length of the waveguide, due to both linear and nonlinear loss from residual two-photon absorption (TPA). As a result, the nonlinear MI process will get weaker with propagation length. The majority of the observable MI (and nonlinear phase shift) will in fact originate near the input end of the waveguide. For this reason, the nonlinear phasematch is estimated using an

average value of the peak pump power calculated along the entrance portion of the waveguide, where the power remains larger than 1/e of the coupled power P0 at the input facet. The average power $P_{avg1/e}$ is calculated by solving Eq. 4.5 and Eq. 4.6 below.

$$P_{avg1/e} = \frac{1}{z_1/e} \int P(z)dz \tag{4.5}$$

$$\frac{dP}{dz} = -\alpha P - 2\gamma_{im} P^2 \tag{4.6}$$

Here, α is the linear loss of the waveguide (0.58/cm), γ_{im} (6.3 (Wm)-1) is the imaginary part of the waveguide's effective nonlinear response from two-photon absorption, and $z_{1/e}$ the length after which the power has dropped by 1/e. Due to the short duration of the pump pulses and the small TPA coefficient, the effect of TPA-induced free carrier absorption is miniscule and can be neglected. The red squares in Figure 4.23 are then located by plotting the nonlinear phase mismatch $2\gamma_{im}P_{avg1/e}$ versus the detuning $\Delta\omega$ for MI bands on the red side of the pump. The uncertainty in the magnitude of the nonlinear phase shift (vertical error bar) is derived from a 1 dB uncertainty in the determination of the input coupling loss, and therefore increases with increasing pump power. The uncertainty in the detuning (horizontal error bar) is derived from the -1 dB bandwidth of the modulation instability peaks in Figure 4.19. As the experimental data points in Figure 4.23 correspond to spectral positions at which the linear and nonlinear phase mismatch are equal and opposite in sign, a fit curve drawn through the data following the form of Eq. (1) will therefore yield $-\Delta k_{lin}(\Delta\omega)$, and can thus be used to obtain an experimental estimate of β_2 and β_4. The solid black line in Figure 4.23 depicts the fit for $-\Delta k_{lin}(\Delta\omega)$ obtained by using a regression technique to minimize the left hand side of Eq. (1). The shaded region illustrates the bounds on the fitted detuning curve resulting from the error on the dispersion coefficients.

The fit results in a value of -0.43 ±0.07 ps2/m for β_2, and 2.3 ±0.4 x 10^{-4} ps4/m for β_4. The fitted dispersion coefficients are also compared to values obtained from numerical mode-solver simulations (Figure 4.18). The fitted value for β_2 agrees within error to the value of -0.47 ps2/m predicted by simulations. However, the simulated value for β_4 of 3.2 x 10^{-5} ps4/m is approximately a factor of 7 smaller than the fitted value. Unfortunately, small variations in β_4 have a large impact in terms of predicting the conditions for phase matching, particularly because the β_4 dependence in Eq. (1) varies as the fourth power of the detuning $\Delta\omega$. For example, substituting the simulated β_2 and β_4 values into Eq. (1) would suggest that the MI(2) band at the red edge of the supercontinuum in Figure 4.20 should appear approximately near 3900 nm, which is inconsistent with the experimental observations. One likely source of the difference between simulated and fitted dispersion coefficients is numerical error. For example, the fourth-order dispersion

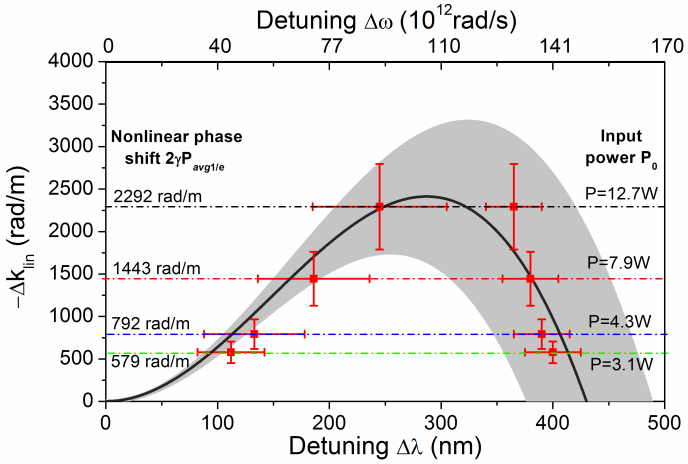

Figure 4.23: Curve fit describing the linear phase mismatch after propagation through the 2 cm long waveguide, as a function of detuning on the red side of the pump. The silicon wire dispersion coefficients extracted from this fit are β_2 = -0.43 ±0.07 ps2/m and β_4 = 2.3 ±0.4 x 10^{-4} ps4/m. The red squares represent the detuning wavelengths of the MI(1) and MI(2) peaks, where the corresponding nonlinear phase mismatch $2\gamma P_{avg1/e}$ term (dash-dotted lines labeled on the left) balances the linear phase mismatch at each value of input peak pump power (labeled on the right). The vertical error bars originate from a 1 dB uncertainty in the input coupling, while the horizontal error bars are associated with the 1 dB bandwidth of each modulation instability peak.

coefficient β_4 is computed by taking four derivatives of the frequency-dependent modal propagation constant $\beta(\omega)$, with numerical uncertainty accumulating at each derivative. However, even if the numerical precision of the mode solver calculations were improved, there will remain more fundamental sources of uncertainty associated with small local variations in the dimensions of the wire waveguide. While the dimensions of a simulated waveguide are assumed to remain constant along its entire length, in practice, the height and width of the core can vary locally due to very small manufacturing variations in the thickness of the SOI layer, lithographic tolerances, and reactive ion etch loading and bias. Various studies have documented that the dispersion of silicon photonic wires is extremely sensitive, even to nanometer-scale variations in their cross-sectional dimensions, on account of their large refractive index-contrast. While it is possible to control the variation of the waveguide dimensions on the level of a few nanometers using state-of-the-art silicon CMOS processing technology, the remaining fluctuations can nevertheless produce significant variations in the dispersion characteristics, particularly in higher-order coefficients such as β_4. Thus, it is important to note that the β_2 and β_4 values derived from the experimental data in fact represent an average waveguide dispersion, which takes into account the inevitable manufacturing-dependent local

dispersion variations seen by the pump pulses propagating along the 2 cm long waveguide. Moreover, given the difficulty of achieving perfectly uniform dispersion throughout a silicon photonic wire, it is likely that an experimental approach for extracting average dispersion values, such as the method outlined above, will be required in combination with numerical simulations to produce a sufficiently accurate design and analysis methodology for broadband highly nonlinear silicon photonic wire devices. In summary, we have shown that a supercontinuum with a bandwidth of nearly 1000 nm spanning from the telecom band to the mid-IR, can be generated by pumping a 2 cm long SOI wire waveguide with mid-IR picosecond pump pulses having moderate peak power. More generally, our demonstration illustrates that when using pump photons with energy close to half the band gap of silicon, SOI wires have an enormous potential as efficient, compact nonlinear optical devices. In addition, we report a valuable method for analysis of the modulation instability peaks within the supercontinuum spectrum, and use this method to re-construct the linear phase-mismatch near the pump as a curve fit to the experimental data. In turn, the linear phase-mismatch is used to extract values for the dispersion coefficients β_2 and β_4. This method is general and can be applied to characterize the dispersion characteristics of various highly-nonlinear optical devices, based upon silicon or other high-index contrast materials. Comparison of the extracted dispersion values with those obtained through numerical simulations illustrates that the experimental analysis approach can be more accurate, particularly for higher orders of dispersion. In practice, a combination of the experimental and simulation techniques will likely be required for sufficiently accurate silicon nonlinear waveguide device design.

References

[1] J M Dudley and J R Taylor. *Supercontinuum Generation in Optical Fibers*. Cambridge books online. Cambridge University Press, 2010.

[2] J Kaminski, CF and Watt, RS and Elder, AD and Frank, JH and Hult. *Supercontinuum radiation for applications in chemical sensing and microscopy*. Applied Physics B, 378:367–378, 2008.

[3] S V Smirnov, T J Ellingham, S M Kobtsev, S Kukarin, and S K Turitsyn. *Optical spectral broadening and supercontinuum generation in telecom applications*. Optical Fiber Technology, 12:122–147, 2006.

[4] W H Reeves, D V Skryabin, F Biancalana, J C Knight, P St J Russell, F G Omenetto, A Efimov, and A J Taylor. *Transformation and control of ultra- short pulses in dispersion-engineered photonic crystal fibres*. Nature, 424(July):2–6, 2003.

[5] NKT Photonics. *Application note: Supercontinuum Generation in photonic crystal fibers*. 2009.

[6] Akira Hasegawa. *Transmission of stationary nonlinear optical pulses in dispersive dielectric fibers. I. Anomalous dispersion*. Applied Physics Letters, 23(3):142, 1973.

[7] John M. Dudley and Stéphane Coen. *Supercontinuum generation in photonic crystal fiber*. Reviews of Modern Physics, 78(4):1135–1184, October 2006.

[8] D R Solli, C Ropers, P Koonath, and B Jalali. *Optical rogue waves.* Nature, 450(7172):1054–7, December 2007.

[9] Michael R Lamont, Barry Luther-Davies, Duk-Yong Choi, Steve Madden, and Benjamin J Eggleton. *Supercontinuum generation in dispersion engineered highly nonlinear (gamma = 10 /W/m) As2S3) chalcogenide planar waveguide.* Optics Express, 16(19):14938–44, September 2008.

[10] Xin Gai, Duk-Yong Choi, Steve Madden, Zhiyong Yang, Rongping Wang, and Barry Luther-Davies. *Supercontinuum generation in the mid-infrared from a dispersion-engineered As2S3 glass rib waveguide.* Optics Letters, 37(18):3870–2, September 2012.

[11] R Halir, Y Okawachi, J S Levy, M A Foster, M Lipson, and A L Gaeta. *Ultrabroadband supercontinuum generation in a CMOS-compatible platform*. Optics Letters, 37(10):1685–1687, 2012.

[12] David Duchesne, Marco Peccianti, Michael R E Lamont, Marcello Ferrera, Francois Légaré, Roberto Morandotti, Sai Chu, Brent E Little, and J Moss. *Supercontinuum generation in a high index doped silica glass spiral waveguide*. Optics Express, 18(2):391–393, 2010.

[13] C R Phillips, Carsten Langrock, J S Pelc, M M Fejer, J Jiang, Martin E Fermann, and I Hartl. *Supercontinuum generation in quasi-phase-matched LiNbO3 waveguide pumped by a Tm-doped fiber laser system.* Optics Letters, 36(19):3912–4, October 2011.

[14] Lianghong Yin, Qiang Lin, and Govind P Agrawal. *Soliton fission and supercontinuum generation in silicon waveguides.* Optics Letters, 32(4):391–3, February 2007.

[15] I-Wei Hsieh, Xiaogang Chen, Xiaoping Liu, Jerry I Dadap, Nicolae C Panoiu, Cheng-Yun Chou, Fengnian Xia, William M Green, Yurii a Vlasov, and Richard M Osgood. *Supercontinuum generation in silicon photonic wires.* Optics Express, 15(23):15242–9, November 2007.

[16] Bart Kuyken, Xiaoping Liu, Richard M Osgood, Roel Baets, Günther Roelkens, and William M J Green. *Mid-infrared to telecom-band supercontinuum generation in highly nonlinear silicon-on-insulator wire waveguides.* Optics Express, 19(21):20172–81, October 2011.

[17] Shaul Pearl, Nir Rotenberg, and Henry M. van Driel. *Three photon absorption in silicon for 23003300nm*. Applied Physics Letters, 93(13):131102, 2008.

[18] Dj Jones, Sa Diddams, Jk Ranka, a Stentz, Rs Windeler, Jl Hall, and St Cundiff. *Carrier-envelope phase control of femtosecond mode-locked lasers and direct optical frequency synthesis*. Science (New York, N.Y.), 288(5466):635–40, April 2000.

[19] V Z Kolev, M W Duering, B Luther-Davies, and a V Rode. *Compact high-power optical source for resonant infrared pulsed laser ablation and deposition of polymer materials.* Optics Express, 14(25):12302–9, December 2006.

[20] Pao T Lin, Vivek Singh, Juejun Hu, Kathleen Richardson, J David Musgraves, Igor Luzinov, Joel Hensley, and Lionel Kimerling. *Chip-scale Mid-Infrared Chemical Sensors Using Air-clad Pedestal Silicon Waveguides*. Lab Chip, 2013.

[21] Bart Kuyken, Xiaoping Liu, Günther Roelkens, Roel Baets, Richard M Osgood, and William M J Green. *50 dB parametric on-chip gain in silicon photonic wires.* Optics Letters, 36(22):4401–3, November 2011.

[22] Xiaoping Liu, Bart Kuyken, Gunther Roelkens, Roel Baets, Richard M Osgood Jr, and William MJ Green. *Bridging the mid-infrared-to-telecom gap with silicon nanophotonic spectral translation*. Nature Photonics, 6(10):667–671, 2012.

[23] Varun Raghunathan, Ramesh Shori, Oscar M. Stafsudd, and Bahram Jalali. *Nonlinear absorption in silicon and the prospects of mid-infrared silicon Raman lasers*. Physica Status Solidi (a), 203(5):R38–R40, April 2006.

[24] Xiaoping Liu, Richard M. Osgood, Yurii a. Vlasov, and William M. J. Green. *Mid-infrared optical parametric amplifier using silicon nanophotonic waveguides*. Nature Photonics, 4(8):557–560, May 2010.

5

A silicon based optical parametric oscillator

Silicon has an indirect bandgap, which makes light generation very inefficient [1]. This chapter shows how tunable sources based on the Kerr nonlinearity can be made in silicon. More specifically, the chapter describes how a silicon based optical parametric oscillator can be built. It starts by summarizing the results from [2], where a widely tunable hybrid fiber-silicon OPO is demonstrated. The chapter concludes by pointing out how a widely tunable monolithically integrated silicon optical parametric oscillator can be made.

5.1 Introduction

The high optical parametric gain in a nonlinear medium can be exploited to make broadband coherent sources. Such sources can be constructed by adding feedback to the nonlinear system. Coherent light can be generated in such devices when the gain of a signal equals the optical loss of the signal. These devices are called optical parametric oscillators (OPO). The bandwidth of these sources can potentially be very broad as a result of the enormous bandwidth of the nonlinear processes which give rise to the optical parametric amplification. In a traditional OPO, the nonlinear parametric gain medium consists out of a crystal made out of a material with a high second order nonlinearity such as lithium niobate [3]. In this work an OPO with a silicon waveguide acting as a nonlinear crystal is demonstrated.

5.2 A silicon based optical parametric oscillator

This section summarizes the results from "A silicon-based widely tunable short-wave infrared optical parametric oscillator" [2]. A schematic of the silicon based OPO is shown in figure 5.1. A 900 nm wide, 220 nm high, 2 cm long spiral waveguide is patterned on the silicon-on-insulator chip and acts as the nonlinear gain medium. Using a cut-back method, the propagation loss in the waveguide is measured to be 0.6 dB/cm. The light is coupled in and out of the chip with lensed fibers introducing a loss of 7 dB per facet. The chip is pumped with 2 ps pump pulses generated by a MIRA OPO (see [2] for the details). The pump and feedback signal are combined in a 90/10 splitter in the absence of a commercially available (de-) multiplexer working at a wavelength of $\approx$ 2200 nm.

In a first experiment, the single pass parametric gain of the silicon waveguides is measured as a function of signal wavelength. Figure 5.2 shows the measured gain when the waveguide is pumped by pump pulses having a central wavelength of 2170 nm with an on chip peak power of 24 W. As seen in the figure, the single pass amplification can exceed 50 dB. In a second experiment, the round trip loss of the cavity is measured. This is shown in blue in figure 5.2. The use of fiber components designed for the telecommunication window instead of the long wavelengths used in the experiment results in high round trip losses. Fortunately, the gain in a wide window around 2070 nm and a small window around 2280 nm surpasses the round trip loss. When the roundtrip time of the cavity is tuned with the variable delay such that the roundtrip time equals the repetition rate of the pump ($\approx$ 13.2 ns), the pump pulses amplify the circulating pulses synchronously.

The roundtrip time of the circulating pulses is highly dependent on the wavelength as a result of the high dispersion in the optical fiber. This property can be used to tune the OPO by changing the delay in the variable delay line: the roundtrip time of a specific circulating wavelength signal can be synchronized with the pump. Figure 5.3 shows the on chip output power of the generated pulses as a function of signal wavelength. In the experiment, the pump pulses have an on chip power of 24 W and are centered at 2175 nm.

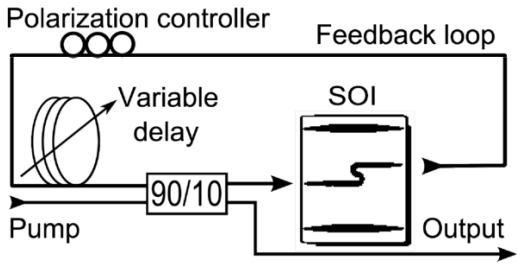

Figure 5.1: A schematic of the silicon based optical parametric oscillator.

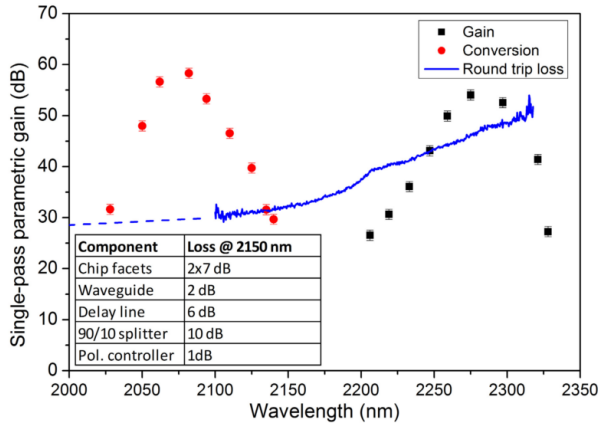

Figure 5.2: The parametric gain as a function of signal wavelength and the round trip loss in the cavity.

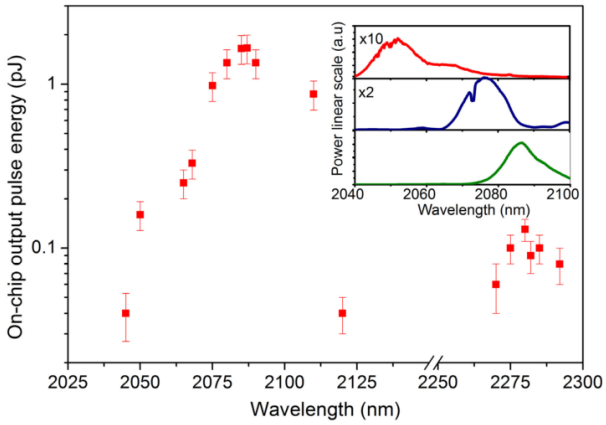

Figure 5.3: The on chip output pulse energy as a function of output wavelength of the OPO. The inset shows the several output spectra of the OPO.

5.3 Future directions

The silicon based OPO demonstrated in the previous section has the enormous advantage that no free space components have to be used, but is still rather complex. Ideally the optical cavity, in the previous section formed by the fiber loop, should be included on the chip. This can potentially reduce the round trip losses significantly because no in and out coupling is needed. The resulting low thresholds make quasi-continuous wave operation within reach. In this section a singly reso-

nant quasi-continuous wave optical parametric oscillator structure is discussed. A schematic is shown in figure 5.4. The OPO is made out of the waveguides very similar to the waveguides discussed in section 3.3.3.2: they are 1700 nm wide and 400 nm high. The OPO can be pumped with a continuous wave signal or a quasi continuous wave signal, as long as the duration of the pulses is much longer than the cavity round trip time. In the cavity the pump will amplify a long wavelength signal, for example at $\approx$ 3800 nm. The evanescent couplers in the coupling section are designed such that they only couple the long wavelength signal back and not the pump or the short wavelength signal generated in the four wave mixing process.

When the gain overcomes the round trip losses, optical parametric oscillation is possible. The propagation loss in the cavity can be assumed to be $\approx$ 1 dB/cm. The gain section can be assumed to be 2 cm long. By numerically integrating the coupled wave equations [4] governing the four-wave-mixing process in Python, while assuming that there is no nonlinear loss and assuming a nonlinear parameter of 15 $W^{-1}m^{-1}$ the single pass gain in the 2 cm long cavity can be calculated. The gain as a function of pump power is shown in figure 5.5. Here it is assumed that the four wave process is perfectly phase matched. Oscillation is possible when the single pass gain is higher than the loss induced by the coupling sections. The coupling section is assumed to consist out of two waveguides with a width of 1700 nm separated by a gap of 470 nm over a length of 300 um. The coupling as a function of wavelength is simulated in Fimmprop ©and shown in figure 5.6. The coupling is approximately 100 % at a wavelength of 3800 nm. The 3 dB bandwidth extends from 3420 nm to beyond 4000 nm. In this range oscillation is possbile as long as the gain exceeds 6 dB, this means that the pump power has to be $\approx$ 7.5 W. Finally, the output wavelength generated by the OPO can be tuned, by tuning the pump wavelength. As discussed in 3.3.3.2, the phase matched signal and idler wavelengths are heavily dependent on the pump wavelength for these waveguides.

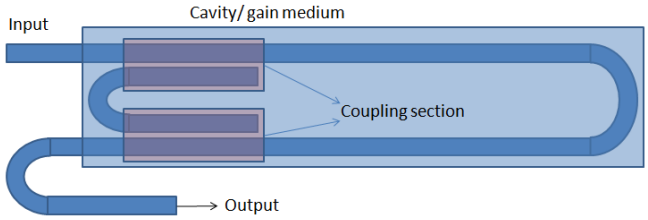

Figure 5.4: A schematic of a singly resonant monolithically integrated optical parametric oscillator.

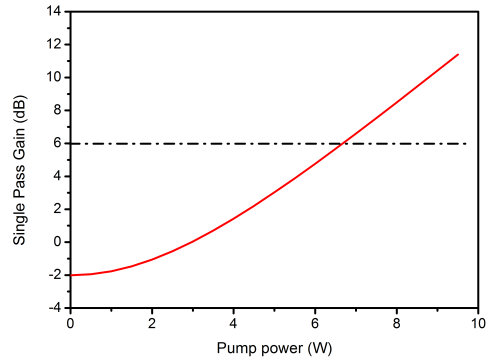

Figure 5.5: The single pass gain in the SROPO cavity.

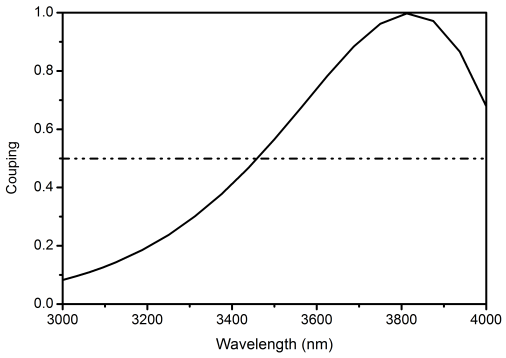

Figure 5.6: The coupling efficiency of one coupling section as a function of wavelength.

5.4 Conclusion

In this chapter a silicon-based OPO is discussed. This OPO uses a silicon waveguide as a nonlinear parametric gain medium. As a result of the broadband parametric gain obtained in such waveguides, it is possible to make a widely tunable OPO. Indeed experimentally it is demonstrated that an OPO can be built: it is tunable in a 75 nm wide band near 2075 nm. Additionally a design for a monolithically integrated quasi continuous wave OPO is discussed. The threshold power of the OPO is sufficiently low to pump the waveguides with a quasi CW signal.

5.5 A silicon-based widely tunable short-wave infrared optical parametric oscillator.

The content of this section was published in Optics Express [2]

The core of the OPO consists of a highly nonlinear silicon photonic wire. The photonic wire is fabricated in a CMOS pilot line on a 200 mm silicon-on-insulator (SOI) wafer, consisting of a 220 nm silicon waveguide layer on top of a 2 μm buried oxide layer. Fig. 5.7 (a) shows a schematic cross section of the silicon photonic wire. The 2 cm-long air-clad photonic wire has a rectangular cross-section of 900 nm x 220 nm. The photonic wire is terminated by an adiabatic taper at both ends, transitioning to a 3 μm wide waveguide section at the cleaved facets. By using a cut-back technique on a set of 0.07, 1, 2, 4, 7 cm long wires, the propagation loss for the quasi-TE mode is determined to be 1 0.1 dB/cm across the 2100-2400 nm wavelength range. Input/output coupling is accomplished with lensed fibers, resulting in a -7 dB ±1 dB coupling efficiency at each facet. The high index contrast between the silicon core and its cladding allows the 2 cm-long wire to be coiled into a small spiral occupying only 700x400 μm^2, as shown in Fig. 5.7(b). The high intrinsic Kerr nonlinearity of silicon ($\chi^{(3)} \approx$ 3.9x10^5 pm2/V2 at 2200 nm [5]) as well as the high optical confinement obtained in these photonic wires (effective mode area of 0.27 μm2) produces a large real part of the complex effective nonlinear parameter γ. For the quasi-TE mode, γ is approximately (150 + i0.6) $W^{-1}m^{-1}$ [6] within the 2150-2200 nm (0.56 eV) wavelength range. The photonic wires are pumped near 2200 nm in order to minimize parasitic two-photon absorption processes in silicon (1.12eV bandgap), resulting in a large nonlinear figure of merit Reγ/(4 Imγ) $\approx$ 20. The efficiency of the FWM process is further enhanced by phase matching the optical waves, achieved by engineering the photonic-wire dispersion. The phase-matching condition in a degenerate FWM process is given by [7]

$$\beta_2 \Delta\omega^2 + \frac{\beta_4 \Delta\omega^4}{12} + 2\gamma P = 0 \tag{5.1}$$

Here, $\Delta\omega$ is the frequency detuning between pump and signal (and also between pump and idler), β_2 and β_4 are the second- and fourth-order dispersion coefficients respectively, evaluated at the pump frequency. This relation yields a solution in the vicinity of the pump (i.e., where the fourth-order dispersion term is negligible) when the second-order dispersion is negative (anomalous dispersion), leading to so-called broadband phase matching. Far from the pump, a second solution (termed discrete-band phase matching) can be found provided that the sign of the fourth-order dispersion is opposite to the sign of the second-order dispersion. This discrete band phase matching principle has been used to obtain amplification in photonic crystal fiber and oscillation in highly nonlinear optical fiber, while pumping the fiber within the normal dispersion regime. The photonic wire used here permits both broadband and discrete band phase matching, since it has a negative second-order dispersion coefficient $\beta_2 \approx$ -0.6 ps2/m and a positive fourth-order dispersion coefficient $\beta_4 \approx$ 5.1x10^{-4} ps4/nm at 2175 nm for the quasi-TE mode, as experimentally measured in [8].

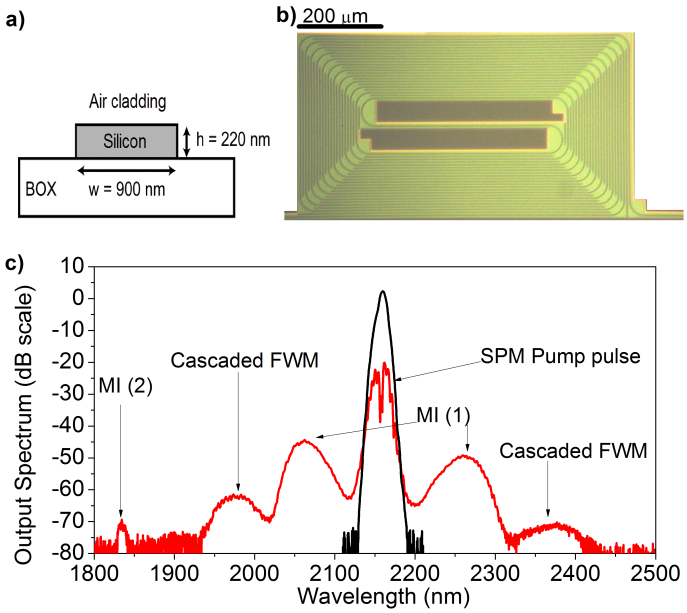

Figure 5.7: (a) Schematic cross-section of the silicon photonic wire. (b) Optical microscope image of the spiral-coiled 2 cm-long silicon wire used within the OPO. The on-chip footprint occupied by the wire is 700 μm 400 μm. (c) The input (black trace) and output (red trace) spectra of the picosecond pump pulses (repetition rate = 76 MHz, FWHM = 2 ps, peak power ≈24W) centered around 2160 nm, going through the 2 cm silicon photonic wire. The pump is broadened by self-phase modulation. The spectral peaks MI(1) and MI(2) label the phase matched wavelengths at which the pump amplifies the background noise via modulation instability.

In the absence of a probe signal, the high peak-power pump pulses will amplify background noise within the highly nonlinear silicon wire [9]. This process is commonly referred to as modulation instability (MI) and/or parametric fluorescence [25], and can be seen in Fig. 5.7 (c). The black trace illustrates the spectrum of the picosecond pump pulse train (Coherent Mira-OPO, FWHM = 2 ps, repetition rate = 76 MHz, peak power ≈24 W, center wavelength of 2160 nm) at the input of the wire, as recorded by a mid-IR spectrum analyzer (Yokogawa AQ6375) at a resolution bandwidth of 1 nm. The red trace is obtained after transmission of the pump through the quasi-TE mode of the 2 cm-long wire. Near the center wavelength of the pump, two side lobes at 2062 nm and 2260 nm (labeled MI (1)) appear in the output spectrum. These side lobes relate to the first set of phase-matching solutions of Eq. 5.2, nearest to the pump frequency. Further away from the pump, an additional lobe labeled MI (2) appears at 1835 nm. At this wavelength Eq. 5.2 is also satisfied, leading to a discretephase matching band. From photon energy

conservation considerations, an MI (2) peak is also expected near 2620 nm. However this is beyond the cut-off wavelength of the optical spectrum analyzer (OSA) used. Finally, two additional peaks appear at 1975 nm and 2378 nm, originating from cascaded FWM processes between the pump and the MI (1) sidelobes.

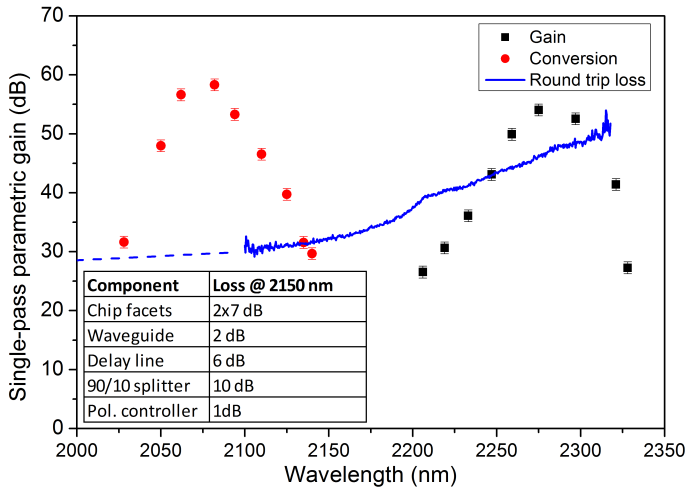

Figure 5.8: The on-chip single-pass parametric gain and conversion of a low-power CW signal (<0.1 mW) within the 2 cm long silicon photonic wire. A CW probe signal is combined with a high peak power picosecond source (repetition rate = 76 MHz, FWHM = 2 ps), having an on-chip peak power of 24 W (48 pJ pulse energy). The error bars are determined by the +/- 1 dB uncertainty in the input/output coupling efficiency. The round-trip loss of the fiber-based cavity is shown in blue. Due to the absence of appropriate optical sources below 2100 nm, the values between 2000 nm and 2100 nm (dashed blue curve) are a linear extrapolation of the round-trip loss to the value obtained at 1550 nm. The inset table shows the contribution of the fiber loop components to the total round-trip loss at 2150 nm.

The strong modulation instability sidelobes in Fig. 5.7(c) mark the spectral regions in which phase matching is achieved, and accordingly label the locations where optical parametric amplification is expected. The magnitude of the on-chip single-pass parametric gain is measured via the amplification experienced by a low power continuous wave (CW) probe signal (IPG Photonics Cr2+:ZnSe external cavity tunable laser), as described in [10]. The picosecond pump operating at a wavelength of 2175 nm is coupled into the quasi-TE mode of the wire, with 48 pJ pulses (peak power ≈24 W) at the wire input. The pump is combined with the co-polarized low-power probe laser (< 0.1 mW), using a 90/10 fused fiber coupler. Fig. 5.8 illustrates that the measured single-pass gain can be as large as 54 dB (black squares) for a probe signal tuned to 2275 nm (MI (1) band on the red side of the pump), while the corresponding on-chip conversion efficiency (red circles)

has a maximum value of 58 dB at 2083 nm. The single-pass gain within the MI (2) bands could not be directly measured, due to the absence of an appropriate optical probe source at either 1835 nm or 2620 nm.

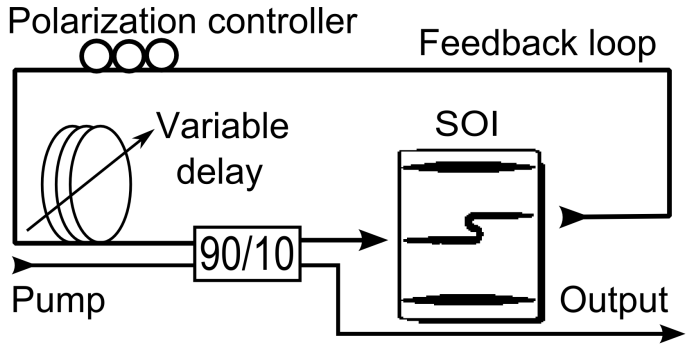

Figure 5.9: Schematic of the fiber cavity configuration of the silicon based OPO. The pump pulses are combined with the output of the silicon chip with a 90/10 coupler. A variable delay line within the cavity ensures that the round-trip time of the signal pulses matches the pump repetition period. A polarization controller ensures that the light within the feedback loop is coupled into the TE mode of the waveguide.

The optical feedback required for the parametric oscillator is achieved using a fiber cavity configuration consisting of ≈ 5.8 m standard single mode fiber (SMF-28), as illustrated in Fig. 5.9. The output from the amplifying silicon photonic wire is combined with the pump pulses using a 90(pump) / 10 (signal) fused fiber coupler and directed back to the wire input facet. The feedback loop contains a variable delay line to synchronize the cavity circulating pulses with the input pump pulses. When the cavity round-trip time is an integer multiple of the pulse repetition period (two times in this work), the circulating generated signals will overlap temporally and spatially with the pump pulse train inside the silicon photonic wire. Therefore, the circulating pulses will be synchronously amplified each round-trip, resulting in optical parametric oscillation provided that the gain exceeds the round-trip loss. We note that parametric amplification within the optical fiber cavity is negligible since the nonlinear parameter of SMF-28 fiber is approximately five orders of magnitude smaller than that of the silicon waveguide. The measured round-trip loss of the cavity, illustrated by the blue curve in Fig. 5.8, originates from the high fiber-chip insertion losses and the insertion loss of the fiber-optic components within the system. The intracavity round-trip losses at 2150 nm are tabulated in the inset of Fig. 5.8. The total round-trip loss is found to increase from 32 dB at 2100 nm, to 37 dB at 2200 nm, and to 48 dB at 2300 nm. The large single-pass parametric gain available in the silicon photonic wire can compensate for the high round-trip losses in two spectral bands near 2075 nm and 2275 nm; thus optical parametric oscillation can occur within these bands. The output spectrum of the

silicon-based OPO pumped at 2175 nm is shown in Fig. 5.10 (a). When the OPO is pumped below threshold, i.e. on-chip pump pulse energy ¡ 15 pJ (see Fig. 5.10 (b)), a broadband modulation instability spectrum is generated. At higher pump energies, the single-pass parametric gain overcomes the round-trip loss in the fiber cavity, and oscillation occurs. In Fig. 5.10 (a), the spectrum of the output pulse train centered near 2078 nm becomes apparent above threshold. When the OPO is pumped at 43.1 pJ the 3 dB optical bandwidth of the output pulse is 7.5 nm. The on-chip output pulse energy, defined as the generated signal pulse energy at the output end of the photonic wire, is plotted as a function of the on-chip pump pulse energy in Fig. 5.10 (b). The parametric oscillation threshold occurs at approximately 15 pJ. The optical pulses reach a peak on-chip pulse energy of 1.52 pJ for an on-chip pump pulse energy of 43.1 pJ. The on-chip slope efficiency at threshold is 22.6 4% In the absence of nonlinear loss, the maximum theoretically expected on-chip slope efficiency, for which all additional pump photons at the input of the wire are converted to signal and idler photons at the output of the wire, is given by

$$\frac{\hbar\omega_s}{2\hbar\omega_p} exp(-\alpha L) = 33.1\% \tag{5.2}$$

where $\omega_s$is the signal frequency, ω_p the pump frequency, $\hbar$ Planck's constant, α the linear loss of the silicon photonic wire, and the L the wire length. The discrepancy between the theoretical and experimental values can be explained in terms of an excess nonlinear loss from residual two-photon absorption at the pump wavelength, as well as from absorption due to the associated free-carriers. The nonlinear loss also makes the OPO round-trip loss pump-power dependent, such that the on-chip output pulse energy is not linearly dependent upon the on-chip input pump pulse energy.

The round-trip time in the fiber cavity depends upon the generated signal wavelength, on account of the dispersion accumulated after propagation through the optical fiber and the silicon photonic wire. The net dispersion contribution of the silicon photonic wire is significantly smaller than that of the fiber feedback loop due to its relatively short length and due to the low dispersion designed into the waveguide. Therefore, by changing the optical path length of the fiber feedback loop, a range of signal wavelengths can be synchronized to temporally and spatially overlap with the pump pulse train, resulting in tunable parametric oscillation. The variable delay line within the fiber cavity can be used to continuously tune the OPO output wavelength, provided that the single-pass-gain exceeds the round-trip loss. As illustrated by the data in Fig. 5.8, oscillation is expected within two bands near 2075 nm and 2275 nm, respectively. Figure 5.11 plots the on-chip output pulse energy of the OPO as a function of output wavelength, selected using the variable delay line. The pump wavelength is 2175 nm, and the on-chip pump pulse energy is 48 pJ. The figure illustrates that the OPO can be tuned across a

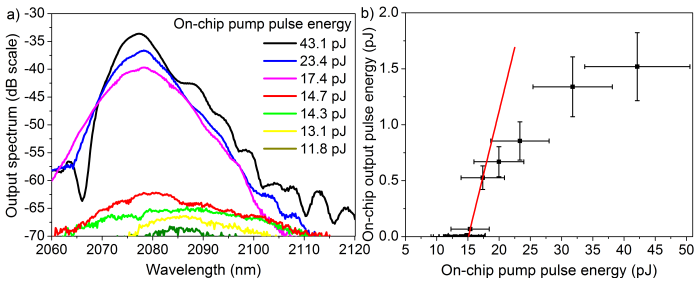

Figure 5.10: (a) The output spectrum of the OPO as a function of on-chip pump pulse energy (documented in the legend). The pump wavelength is 2175 nm. At an on-chip pump energy of 43.1 pJ the 3 dB spectral width of the generated pulses is 7.5 nm. (b) On-chip output energy of the generated pulses as a function of the on-chip pump pulse energy, demonstrating an oscillation threshold of $\approx$ 15 pJ and a slope efficiency of 22.64 %, for a pump at 2175 nm. Using 43.1 pJ pump pulses, the OPO generates 1.52 pJ pulses on-chip. The error bars are determined by the +/- 1 dB uncertainty in the input/output coupling efficiency.

bandwidth of 75 nm near the peak on-chip pulse energy wavelength of 2087 nm. The on-chip pulse energy decreases on either side of this peak due to decreasing single-pass gain. Figure 5.11 also plots the on-chip output energies obtained for OPO operation in the band near 2275 nm. However, the maximum on-chip output power within this wavelength range is approximately 10x lower than that near 2087 nm, on account of the larger round-trip losses shown in Fig. 5.8. The inset of Fig. 5.11 shows several output spectra obtained while tuning the OPO across the band near 2075 nm.

As mentioned above, Eq. 5.2 has another set of solutions far from the pump wavelength, i.e. those from discrete phase matching. As an example, Fig. 5.7(c) illustrates that for pump pulses centered at a wavelength of 2160 nm, an additional modulation instability peak near 1835 nm (MI(2)) is visible. When the pump is centered at 2180 nm, this discrete band shifts to 1857 nm, where phase matching (and thus amplification) is obtained. Oscillation in this band is obtained by changing the cavity round-trip time to be synchronous for pulses generated at 1857 nm. The output spectrum of the OPO operating in this mode is illustrated by the black trace in Fig. 5.12. This discrete band phase matching not only increases the operational bandwidth of the OPO, but it also provides an alternative method of tuning the output wavelength over a broad wavelength range. The frequency detuning $\Delta\omega$ far from the pump, where Eq. 5.2 is satisfied, depends strongly upon the value of the fourth-order dispersion coefficient β_4, which is itself wavelength-dependent. By shifting the pump wavelength, both β_2 and β_4 are varied, and the wavelength for which discrete band phase matching occurs is tuned. A set of output spectra taken with different pump wavelengths is shown in Fig. 5.12. Continuous tuning

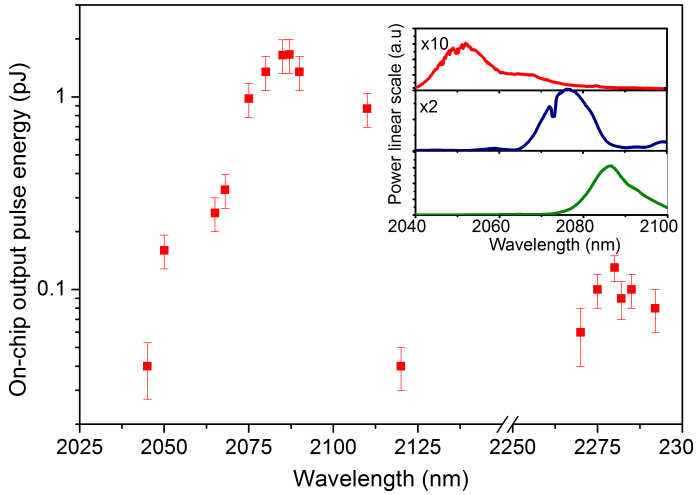

Figure 5.11: On-chip output energy of the generated pulses as a function of oscillation wavelength, for an on-chip pump pulse energy of 48 pJ at 2175 nm. The synchronized output wavelength is tuned using the variable delay line within the fiber cavity. The larger round-trip loss in the cavity leads to lower output at longer wavelengths near 2275 nm. The error bars are determined by the +/- 1 dB uncertainty in the input/output coupling efficiency. The inset plots output spectra obtained for three different settings of the delay line, demonstrating tunable oscillation at three different wavelengths. In comparison with the green trace, the power scale of the blue trace has been magnified by a factor of two, and the scale of the red trace by a factor of 10.

across 150 nm (12.4 THz) from 1857 nm to 2009 nm is obtained by tuning the pump wavelength by only 55 nm (3.38 THz), from 2180 nm to 2235 nm. Optimizing the geometry of the photonic wire to obtain normal dispersion with negative fourth-order dispersion can ultimately lead to even more broadband tuning, with a smaller change in the pump wavelength [11]. Moreover, for the same pump tuning range, the four-wave mixing process simultaneously generates an idler at wavelengths from 2634 nm to 2507 nm. However, the idler lies outside the range of the optical spectrum analyzer used in the experiment and could therefore not be observed.

As shown in Fig. 5.13, the threshold on-chip pump-pulse energy is 16.4 pJ for a pump at 2235 nm generating a signal at 1995 nm. The slope efficiency at threshold is 41 ±8 %, while a value of 35.3 % is theoretically expected. Although these values agree within error, the discrepancy in the mean slope efficiency can be seen to originate from the experimental uncertainty in the wire input/output coupling, which impacts estimation of the on-chip pulse energies. In Fig. 7, the on-chip output pulse energy is linearly dependent upon the on-chip input-pulse energy. From these findings we can conclude that the nonlinear absorption is negligible

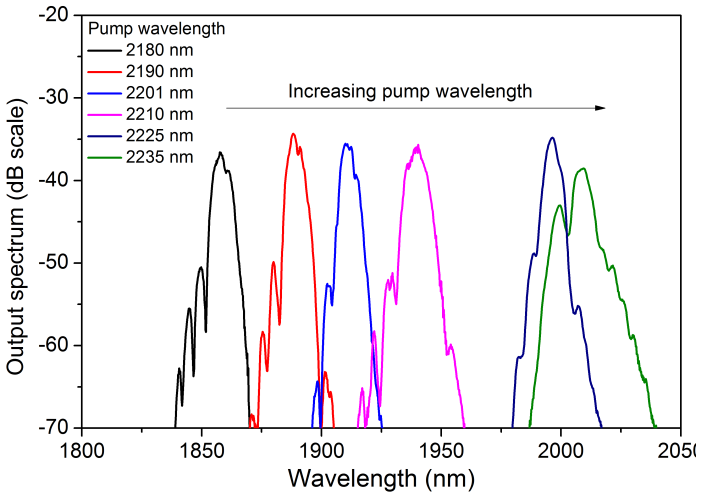

Figure 5.12: Output spectrum of the optical parametric oscillator operating with discrete-band phase matching. The on-chip pump pulse energies (wavelengths) used are 48.4 pJ (2180 nm), 27.0 pJ (2190 nm), 23.4 pJ (2201 nm), 18.8 pJ (2210 nm), 19.0 pJ (2225 nm) and 16.4 pJ (2235 nm). Continuous tuning across a 150 nm spectral range is obtained.

when the OPO is pumped at 2235 nm, at least within the range of on-chip pump pulse energies accessible experimentally.

In summary, we have demonstrated a widely tunable optical parametric oscillator based upon four-wave mixing in a silicon photonic wire. High single-pass broadband optical parametric gain (up to 54 dB) is achieved in a 2 cm long silicon photonic wire when it is pumped with on-chip pump pulses of 48 pJ at 2175 nm. Enclosing the chip within a fiber loop cavity, the high optical gain exceeds the round-trip losses, leading to a synchronously pumped silicon-based OPO. By varying the round-trip time within the fiber cavity, the OPO center wavelength can be tuned across a 75 nm bandwidth near 2075 nm. Furthermore, by taking advantage of the wavelength-dependent higher-order dispersion of the silicon photonic wire, the output wavelength of the OPO can also be tuned from 1857 nm to 2009 nm, by changing the pump wavelength over only 55 nm from 2180 nm to 2235 nm. This silicon-based OPO represents an important step towards a widely tunable monolithically integrated silicon source. Improved performance can be achieved by increasing the input/output coupling efficiency to the chip using inverted taper structures, and by incorporating custom-designed silicon photonic wavelength (de)multiplexing structures for combining/splitting the pump and signal beams with low loss. Further improvement can be obtained by integrating the feedback loop on-chip, for example by using low-loss silicon nitride waveg-

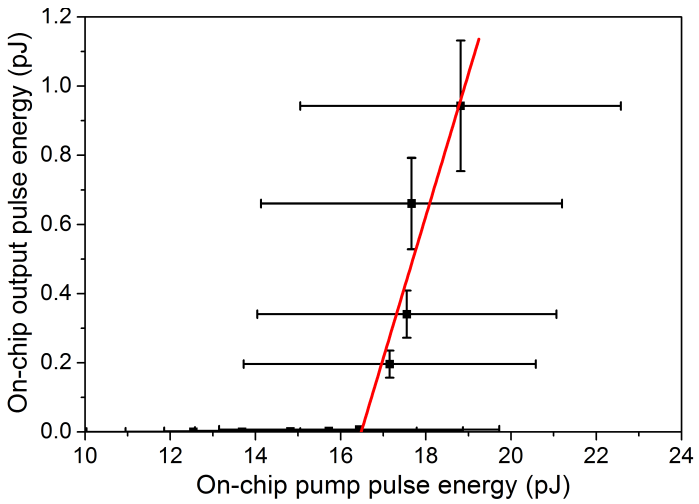

Figure 5.13: On-chip output pulse energy as a function of the on-chip pump-pulse energy, for a pump wavelength of 2235 nm generating an OPO signal at 1995 nm. The threshold on-chip pump energy is 16.4 pJ, and the slope efficiency is 41 8%. Using 18.8 pJ pump pulses, the OPO generates 0.94 pJ pulses on-chip. The error bars are determined by the +/- 1 dB uncertainty in the input/output coupling efficiency.

uides. The thermo-optic effect can then be used on-chip to tune the round-trip time and thus the signal wavelength. Such developments could ultimately result in the miniaturization of large bench-top optical parametric oscillators into highly efficient chip-scale light sources. A promising alternative approach is to make use of integrated high-quality ring resonators pumped with continuous-wave lasers, to enable construction of all-silicon optical frequency comb generators through cascaded four-wave mixing. Another application of such ring resonators could be the generation of ultra-low-noise mode-locked lasers by means of filter driven four-wave mixing.

References

[1] Lorenzo Pavesi and David J Lockwood. *Silicon photonics*, volume 1. Berlin: Springer, 2004.

[2] Bart Kuyken, Xiaoping Liu, Richard M Osgood, Roel Baets, Günther Roelkens, and William M J Green. *A silicon-based widely tunable short-wave infrared optical parametric oscillator.* Optics Express, 21(5):5931–40, March 2013.

[3] V Z Kolev, M W Duering, B Luther-Davies, and a V Rode. *Compact high-power optical source for resonant infrared pulsed laser ablation and deposition of polymer materials.* Optics Express, 14(25):12302–9, December 2006.

[4] Q Lin, Oskar J Painter, and Govind P Agrawal. *Nonlinear optical phenomena in silicon waveguides: modeling and applications.* Optics Express, 15(25):16604–44, December 2007.

[5] Alan D. Bristow, Nir Rotenberg, and Henry M. van Driel. *Two-photon absorption and Kerr coefficients of silicon for 8502200nm*. Applied Physics Letters, 90(19):191104, 2007.

[6] R. M. Osgood, Jr., N. C. Panoiu, J. I. Dadap, Xiaoping Liu, Xiaogang Chen, I-Wei Hsieh, E. Dulkeith, W. M. Green, and Y. a. Vlasov. *Engineering nonlinearities in nanoscale optical systems: physics and applications in dispersion-engineered silicon nanophotonic wires*. Advances in Optics and Photonics, 1(1):162, January 2009.

[7] Mark a Foster, Amy C Turner, Jay E Sharping, Bradley S Schmidt, Michal Lipson, and Alexander L Gaeta. *Broad-band optical parametric gain on a silicon photonic chip.* Nature, 441(7096):960–3, June 2006.

[8] Bart Kuyken, Xiaoping Liu, Richard M Osgood, Roel Baets, Günther Roelkens, and William M J Green. *Mid-infrared to telecom-band supercontinuum generation in highly nonlinear silicon-on-insulator wire waveguides.* Optics Express, 19(21):20172–81, October 2011.

[9] Bart Kuyken, Xiaoping Liu, Günther Roelkens, Roel Baets, Richard M Osgood, and William M J Green. *50 dB parametric on-chip gain in silicon photonic wires.* Optics Letters, 36(22):4401–3, November 2011.

[10] Xiaoping Liu, Richard M. Osgood, Yurii a. Vlasov, and William M. J. Green. *Mid-infrared optical parametric amplifier using silicon nanophotonic waveguides*. Nature Photonics, 4(8):557–560, May 2010.

[11] Q. Lin, T. J. Johnson, R. Perahia, C. P. Michael, and O. J. Painter. *A proposal for highly tunable optical parametric oscillation in silicon micro-resonators*. Optics Express, 16(14):10596, July 2008.

6

Nonlinear optical properties of hydrogenated amorphous silicon waveguides

Using hydrogenenated amorphous silicon for integrated optical circuits has several advantages. The most important one being that hydrogenated amorphous silicon layers can be deposited on any surface at low temperatures. As a result, layers can be integrated on a finished CMOS wafer in the back end [1]. The electronic bandgap is in general wider for a hydrogenated amorphous silicon layer than for a crystalline silicon layer. It is this beneficial property that is used in this work. Instead of going to a longer wavelength window to avoid the two-photon absorption in crystalline silicon as in chapter 4 and 3 a material with lower two-photon absorption in the telecommunication window is used.

6.1 Introduction

6.1.1 Hydrogenated amorphous silicon

In 1975, Spears et al. [2] demonstrated that hydrogenated amorphous silicon (a-Si:H) has semiconductor-like properties. They showed that the resistivity of a layer of a-Si:H changed by orders of magnitude when the doping concentration in the material was changed. Since then, a lot of research has focused on the development of a-Si:H layers for all kinds of applications. The main rationale for the use

of a-Si:H as a semiconductor material has been the fact that the material can be deposited at low temperatures on a lot of different substrates such as glasses, metal and even polymers [3]. The technology is used in a whole range of applications such as photovoltaic cells, flat panel displays, image sensors and so on [3]. The main disadvantage of using a-Si:H, however, is that the material is meta-stable, a result of the so called Staebler-Wronski effect [4]. The metastability was first reported by Staebler and Wronski in 1977. They showed that the conductivity of a-Si:H layers changed after exposing them to a bright light source. Additionally, they showed that it was possible to reverse the photo-induced changes by annealing the sample at 150 °C for half an hour. The metastability has, for example, a detrimental effect on a-Si:H solar cells. The photosensitivity of a-Si:H layers causes the efficiency of solar cells to degrades over time from an initial 10% to 8% [5]. The Staebler-Wronski effect is still widely discussed in the literature until today [6, 7]. However, it is widely accepted that the effect triggering the degradation is the recombination of (photogenerated) electron-hole pairs in the material [8]. The energy released when a electron hole pair recombines gets transferred to the amorphous network and creates a dangling bond.

6.1.2 Hydrogenated amorphous silicon photonic circuits

The combination of the transparency of a-Si:H at telecommunication wavelengths, a high refractive index and the ease of deposition of the a-Si:H layers are the main motivations to develop photonic circuits out of a-Si:H. The low deposition temperature allows to integrate photonic circuits on already prefabricated electronic circuits. Additionally, the possibility to tune the properties of the material by adjusting the deposition parameters [9] gives the material some extra degrees of freedom to tune it [10]. In 1996 [5] the first a-Si:H waveguides were demonstrated and a lot of progress has been made since then. For example in 2009 Selvaraja et al. [1] demonstrated propagation losses as low as 3.5 dB/cm in sub micron waveguides made on 200 mm wafers by 193 nm lithography as well as high Q resonators and Mach-Zehnder interferometers. More recently, people focused on the nonlinear optical properties of these materials. In 2010, researchers at the university of Rochester [11] demonstrated broadband all optical modulation in a-Si:H waveguides. They used a high power short wavelength laser to create carriers in the waveguide by illuminating it from the top. These carriers modulated the absorption in the straight waveguide which is felt by the light traveling through the waveguide. Due to the relatively short carrier recombination time, this all optical modulation is relatively fast. Furthermore, because of the broadband absorption of the generated carriers the demonstrated modulation technique is very broadband. Also in 2010, Shoji et al. reported the first values of the nonlinear absorption and the nonlinear refractive index in a-Si:H nanowire waveguides [12].

They reported a nonlinear absorption coefficient of β = 0.08 cm/GW and a nonlinear refractive index of $0.5 \times 10^{-18} m^2/GW$. These values are 10 times lower than the value found in crystalline silicon (c-Si), making the nonlinear figure of merit, $FOM = \frac{n_2}{\beta\lambda}$ of the material comparable to the one in c-Si. However they found that the carrier lifetime in these waveguides is below 1 ps. This property was exploited in a follow up experiment in 2012 where the group showed pattern effect free wavelength conversion [13]. The basic idea in the paper is that the recombination time is much faster than the symbol rate such that pump pulses converting a signal data at some time do not effect the data at later times by carrier induced absorption. Also in 2010, the Preble group [11] demonstrated highly nonlinear hydrogenated amorphous waveguides. They measured the value for the two-photon absorption coefficient to be as high as 4.2 cm/GW and a nonlinear refractive index of $4.2 \times 10^{-17} cm^2/GW$. Both the values are about 5 times higher than the values found in c-Si resulting in a nonlinear figure of merit of about 0.66, again similar as the value found in c-Si. In 2010, in collaboration with the Université Libre de Bruxelles we demonstrated hydrogenated amorphous silicon waveguides with a much higher nonlinear FOM as compared to its crystalline silicon counterpart for the first time. The value found was 2.1, more than three times higher than the value found in c-Si. The same year in a post deadline conference paper presented at the IEEE annual meeting it was shown that using waveguides made out of this type of a-Si:H all-optical amplification of telecommunication signals up to 26.5 dB was possible. Such an amplification is an improvement of more than a factor of 100 over the best results achieved in c-Si [14] demonstrating the potential of a-Si:H for all-optical signal processing.

6.2 Nonlinear properties of a-Si:H waveguides developed at imec-UGent

This section summarizes the results of "Nonlinear properties of and nonlinear processing in hydrogenated amorphous silicon waveguides" [15]. For the experiments, 220 nm of a-Si:H was deposited using a low temperature Plasma Enhanced Chemical Vapor Deposition process on top of a 1950 nm surface of high-density plasma oxide on a silicon substrate. Waveguides of varying lengths (0.6 to 6 cm) were fabricated using 193 nm optical lithography and dry etching [1]. The photonic nanowires were interfaced to an optical fiber using grating couplers [16]. The cross-section of these waveguides is $500 \times 220 nm^2$. A SEM cross section of the waveguide can be seen in figure 6.1. By using a cutback technique the waveguide loss was measured to be 3.6 dB/cm.

In the experiment, the two-photon absorption and the nonlinear refractive index of the material was measured by studying the transmission of high power short

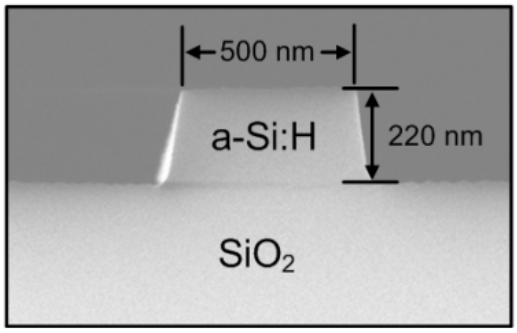

Figure 6.1: A SEM cross-section of the a-Si:H waveguide. The dimensions of the waveguide are shown in the figure.

pulses. The nonlinear absorption was measured by looking at the reciprocal transmission of these short pulses as a function of input peak power of the pulses. It can be shown that this function is linear with the input peak power as long as the nonlinear absorption of the carriers is negligible, so relatively low power pulses need to be used. The relation is found to be [17]

$$\frac{1}{T} = exp(\alpha L) L_{eff} 2Im(\gamma) P + exp(\alpha L) \tag{6.1}$$

Here $L_{eff} = \frac{1-exp(-\alpha L)}{\alpha}$ is the effective length, α the linear absorption coefficient, P the input peak power and $Im(\gamma)$ the imaginary part of the nonlinear parameter of the waveguide. Fitting the experimental data shown in figure 6.2, a value of $-28/Wm$ was found for $Im(\gamma)$. From the imaginary part of the nonlinear parameter of the waveguide the two-photon coefficient was derived and found to be 0.36 cm/GW. To validate the approach, the nonlinear absorption of a deeply etched 220 nm high, 500 nm wide, 1 cm long c-Si photonic wire waveguide was measured as well, the value found here was $-54/Wm$. The value found in c-Si agrees well with literature [18] which validates the setup being used. The nonlinear refractive index of the (hydrogenated amorphous) silicon waveguides was measured by looking at the output spectra of the pulses as a function of the input peak power. By fitting the spectra to a split step algorithm solving the generalized nonlinear Schroedinger equation taking in account carrier effects [19] the nonlinear parameter (and thus the nonlinear refractive index) can be deduced. In figure 6.3, the output spectrum of high peak power pulses (1.4W, 2.9W, 4.6W and 7.3W peak power) after traveling through a 1 cm long a-Si:H waveguide are shown. On the right panel the simulated spectra for the same power levels can be seen. The fit revealed that the real part of the nonlinear parameter is $770 \pm 100/Wm$. This leads to a nonlinear refractive index of $1.2 \times 10^{-17} m^2/W$. Again to validate the approach the experiment was repeated for deeply etched 220 nm high, 500

nm wide, 1 cm long c-Si waveguides. The obtained value of $0.5 \times 10^{-17} m^2/W$ agrees very well with the value found in the literature [18]. For these experiments, it is also important to note that the nonlinearity in the fiber is negligible compared to the nonlinearity in the waveguide. The nonlinear parameter of a fiber ($\gamma = 1.5/Wkm$) is about 500 000 times smaller than the real part of the one found in a-Si:H waveguides such that a couple of meters fiber do not contribute to a significant nonlinear phase shift as compared to that in the a-Si:H waveguide. The larger nonlinear figure of merit found in the a-Si:H waveguides of 2.1 is important in integrated nonlinear optics, because the material is the only CMOS compatible material with such a high nonlinear figure of merit and a high nonlinear refractive index.

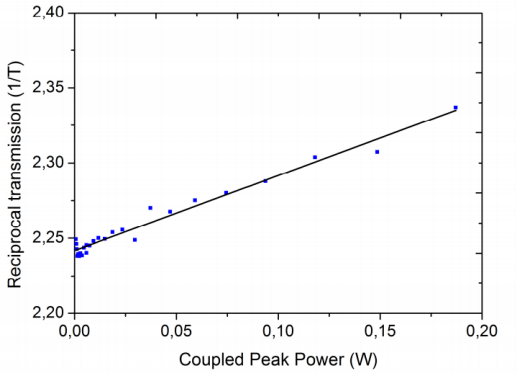

Figure 6.2: The nonlinear transmission of the hydrogenated amorphous silicon waveguide. The reciprocal transmission increases linearly with input peak power.

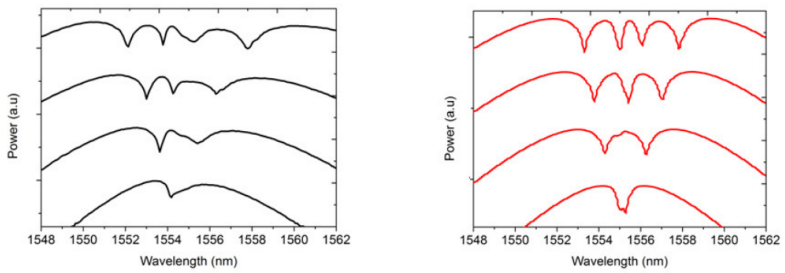

Figure 6.3: The output spectrum of high peak power pulses traveling through the a-Si:H waveguide. The left panel shows the experimental data, the right panel shows the simulation.

6.2.1 Parametric amplification in hydrogenated amorphous silicon waveguides

In this paragraph the most important results from "On-chip parametric amplification with 26.5 dB gain at telecommunication wavelengths using CMOS-compatible hydrogenated amorphous silicon waveguides" [20] are discussed. In a pump probe experiment the amplification of a weak signal by a strong pump is demonstrated. Because of the high peak powers needed in the experiment short bright pulses are used to demonstrate the effect. Since the goal of the experiment was to demonstrate the amplification of a weak (short) pulse by a strong (short) pulse as a function of signal wavelength the pulses had to be synchronized in time and the signal pulse had to be wavelength tunable. This is done by using the scheme shown in figure 6.4. The pump and probe are both derived from the same picosecond pulsed source (PRITEL FF, 3.8 ps FWHM pulses, 10 MHz repetition rate) by using a splitter. The pump pulse is directed right away to the chip after passing through a variable attenuator which allows to alter the (peak) power of the pulses. The signal pulse however is first directed to an EDFA, the enormous amplification by the EDFA makes these pulses so bright that they in fact generate a supercontinuum in the fiber after (and also in) the EDFA. These pulses, having a broad spectrum are sent to a variable delay stage such that at the input of the chip the signal pulses overlap temporally with the pump pulses. The actual signal pulses are made by slicing out a small part of the generated supercontinuum with a tunable filter (1.2 nm passband filter). These are combined with the pump pulses and send to the chip.

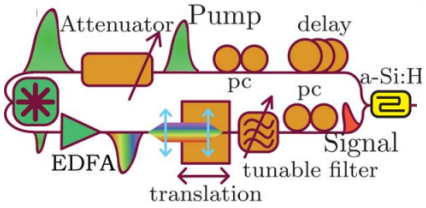

Figure 6.4: A schematic showing how two synchronized short pulses with a different frequency can be created.

On the chip, the nonlinear amplifier consists out of a 1 cm long dispersion engineered hydrogenated amorphous silicon waveguide terminated with grating couplers. The dispersion of the waveguides is measured by measuring the conversion efficiency of a weak continuous wave laser signal as a function of wavelength in the present of a modest power pump continuous wave laser ($\approx 10mW$), see figure 6.5. For a low power pump, the conversion as a function of wavelength is dependent on the phase mismatch as [21]

$$\eta \approx \frac{sin(\Delta kL)^2}{(\Delta kL)^2} \tag{6.2}$$

Fitting the formula to the data reveals the group velocity dispersion, since $-\beta_2 \Delta\omega^2 = \Delta k$. A value of $\beta_2 = -2ps^2/m$ is found.

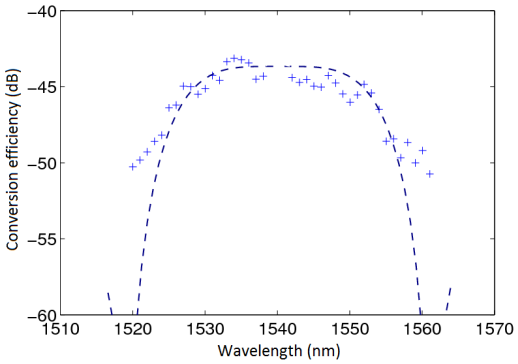

Figure 6.5: The conversion efficiency of a weak signal continuous wave laser as a function of wavelength in a four-wave-mixing experiment with a modest pump power.

The output peak power of the signal pulse when the pulses do not overlap in time was compared with when they did overlap. When the pulses overlap in time the signal pulse gets amplified. This method was used to measure the amplification of the signal as a function of wavelength. The result is shown in figure 6.6 for a coupled pump peak power of 5.3 W.

The more than 26 dB of amplification obtained in the experiment is a more than 20dB improvement over previous results reported in crystalline silicon [14] proving the potential of a-Si:H waveguides for nonlinear optical functions.

6.2.2 Photo sensitivity of the hydrogenated amorphous silicon waveguides

Even when there are no signal pulses to amplify, the high peak power pulses will amplify the background noise in the experiment. This process, called modulation instability (MI), (see section 3.2.2) can be seen in figure 6.7. As a result of the photo sensitivity of the material the nonlinear response decreases over time as shown in the figure. Since the background noise in the system stays the same, the peak of the modulation instability sidebands can be used to quantify the degradation of the material. The peak level of the MI side band as a function of time is plotted in figure 6.7. As expected from the initial paper published by Staebler and Wronski [4] the effect is reversed when the sample is heated at 150 degrees centigrade for 30 minutes (while it is not exposed). When the waveguides, after

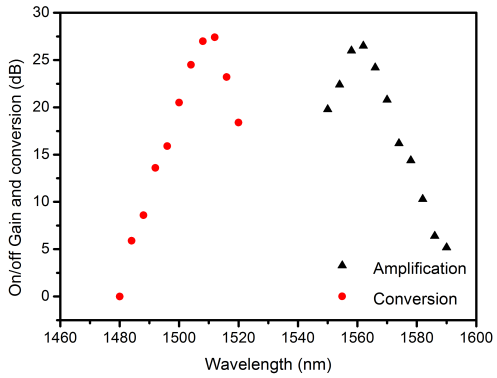

Figure 6.6: The conversion efficiency and amplification in a-Si:H waveguides. The figure shows the conversion efficiency and amplification as a a function of the signal pulse wavelength when the coupled peak power of the pump pulses was 5.3 W in a 1 cm long waveguide.

being annealed, are again exposed to the bright pulses the material degrades again. This can be done again and again as shown in figure 6.8. In all these experiments the pump pulses are centered at 1550 nm.

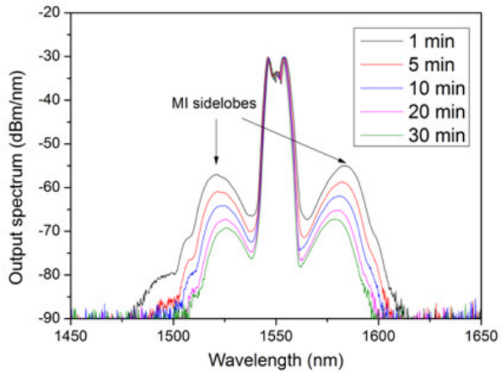

Figure 6.7: Modulation instability over time. The output spectrum of pump pulses with a peak power of 5.3 W is shown.

At first it was believed that the material degrades to a stable state as in the case with a hydrogenated amorphous silicon solar cell: the efficiency goes to a steady state value of about 8% [3]. However, for the a-Si:H waveguides this did not seem to be the case, figure 6.9 shows the result of exposing the material for almost 24 hours to high peak powers (5.3 W) pulses centered at a wavelength of 1565 nm at

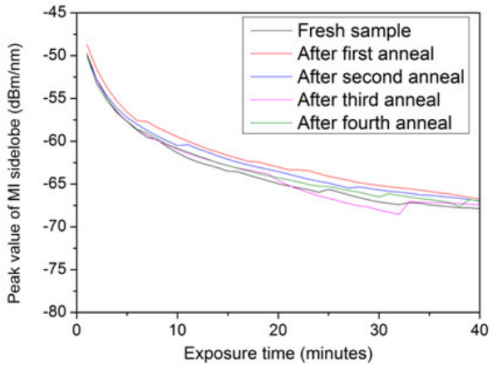

Figure 6.8: Modulation instability over time. The peak of the MI side band as a function of time is shown. When the sample is annealed for 30 minutes at 150 degrees the degradation is reversed.

10 MHz.

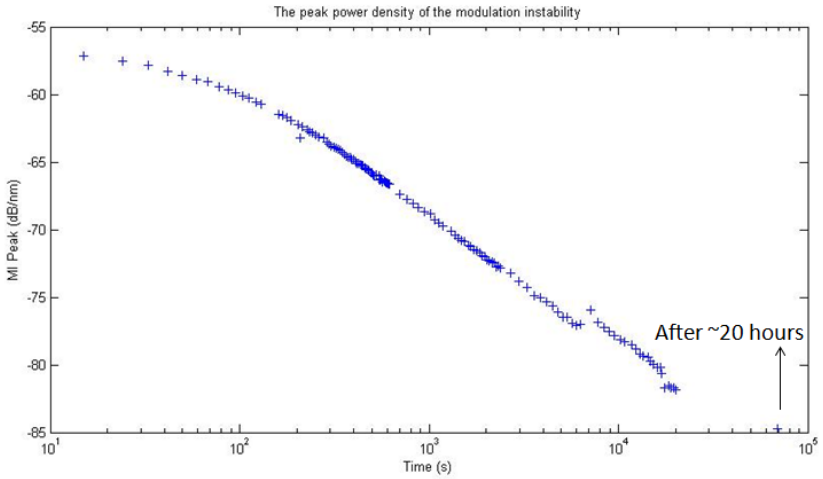

Figure 6.9: Modulation instability peak value as a function of time over an entire day. Here the coupled peak power of the pulses was 5.3 W, while the repetition rate is 10 MHz and the pulse duration is 3.5 ps

6.2.3 Overcoming the material stability problem

6.2.3.1 Temperature dependence of the photosensitivity

In a first experiment the degradation as a function of temperature is investigated. It turns out that the degradation is accelerated when the samples are operated at higher temperatures. The output spectra of high peak power pulses is shown in figure 6.10. At higher operating temperature, the degradation of the material is stimulated.

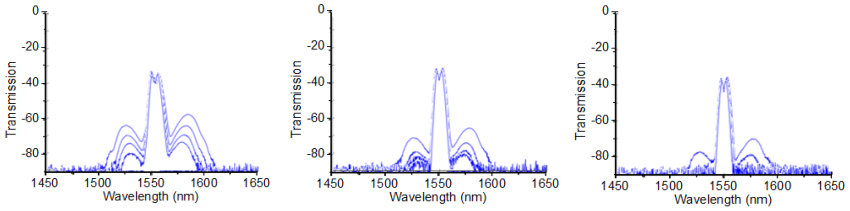

Figure 6.10: Modulation instability as a function of time for different temperatures. The three panels show the output spectrum of 4W peak pulses when the chip is held at room temperature (left), 80 °C (middle) and 120 °C (right). The spectrum is recorded after 1 min, 5 min, 20 min and 60 min for these three temperatures.

6.2.3.2 The bandgap of a-Si:H

The bandgap of the hydrogenated material used so far is about 1.6 eV. At first no two-photon absorption would be expected at 1564 nm (0.792 eV) in the material since we are operating below half bandgap. However the bandgap of amorphous semi-conductors is not as well defined as in a crystalline semiconductor. This stems from the fact that an amorphous semiconductor is not as well structured as its crystalline counterpart. Although it is not well structured, it does have some structure: there is some ordening on an atomic scale. In figure 6.11 the atom pair distribution function is shown for a crystalline solid, an amorphous solid and a gas. For a crystalline solid the distribution has very distinct peaks because the atoms are in a fixed periodic crystal. For an amorphous solid there is some order for atoms which are close to each other, which means that at short distances the atoms can not be at any location they want, however this ordening disappears at longer distances, making the material amorphous.

Due to the ordening at short distances however, the material has a band structure. However the bands are not that well defined as in a crystalline solid. In a crystalline material the electron waves are perfectly periodic because the material is periodic. However for an amorphous material the wave functions can not be periodic since the material is not periodic. This means that the wave functions are localized. Furthermore, due to Heisenberg's uncertainty principle this means

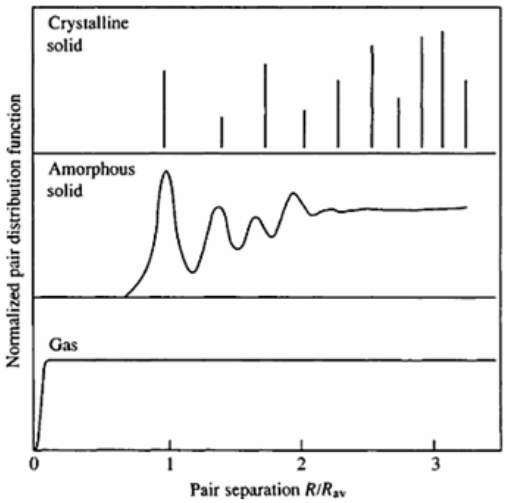

Figure 6.11: The atom pair distribution function for a crystalline solid, an amorphous solid and a gas. Picture from [22]

that the k vector for these states is not well defined. The density of states for an amorphous semi conductor is shown in figure 6.12. The band in an amorphous solid has an exponential tail called an Urbach tail. Additionally there are, because of the presence of defects in the amorphous silicon, defect states in the middle of the bandgap. This can be seen in the figure.

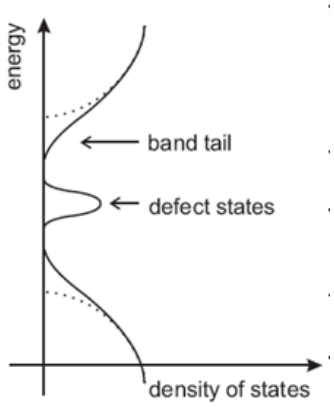

Figure 6.12: The density of states versus energy for an amorphous semiconductor. Picture from [22]

The bandgap is mostly defined (also in this work) as the one found with the

Tauc method [23]. Here it is assumed that the density of states in the bands in the amorphous material are parabolic, but having exponential tails. So when the square root of the optical absorption is plotted as a function of photon energy this will be a linear function for high photon energies, but not for lower energies (because these are in the exponential tail). By extrapolating this line to zero absorption one can find the so called Tauc gap. This is shown in figure 6.13.

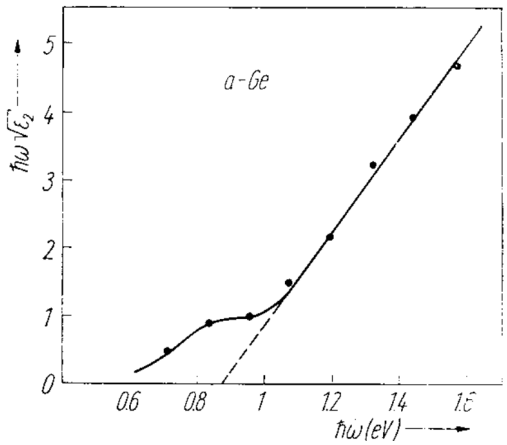

Figure 6.13: The extraction of the bandgap of an amorphous semiconductor, here a-Ge, with the Tauc method.Figure from [23]

This has as a consequence that for the a-Si:H used in this work there is still some two-photon absorption. The remaining two-photon absorption creates carriers, which by their turn create defects when they recombine.

6.2.3.3 Hydrogenated amorphous layers with an increased bandgap

This section discusses some ongoing research on the development of new a-Si:H layers. As mentioned before it is possible to alter the optical and electrical properties of hydrogenated amorphous silicon layers by changing the deposition parameters. However it is also possible to change the optical and electronic properties by doping the layers with impurities such as Sb [24] and C [25]. By increasing the bandgap of the hydrogenated amorphous silicon by doping it with carbon and making waveguides out of it, it is envisioned that nonlinear absorption will be absent in these waveguides. Furthermore, if the nonlinear absorption is absent no carriers can get generated, such that the Staebler-Wronski effect should be absent as well. The ultimate goal is having a stable, nonlinear, CMOS compatible material where two-photon absorption is absent. In a collaboration with the Photovoltaics and Thin Film Electronics Laboratory at EPFL, films with a wider band gap were developed. By ellipsometry the bandgap of the layers was measured. The Tauc

bandgap is found to be 1.8 eV. In collaboration with the University of Saint Andrews waveguides were fabricated with the help of e-beam lithography. A picture of the fabricated layer is shown in figure 6.14. This shows that it is possible to etch the a-Si:H waveguides with a standard etching recipe used for c-Si.

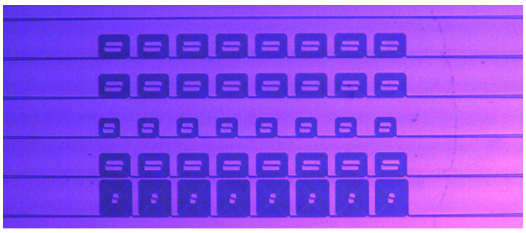

Figure 6.14: A set of spirals with different lengths to measure the optical propagation losses.

However when injecting light in the chip the optical loss was found to be $>$ 15 dB/cm. In figure 6.15 a microscope picture is taken with a Xenics camera sensitive to the injected 1550 nm light of the waveguide.

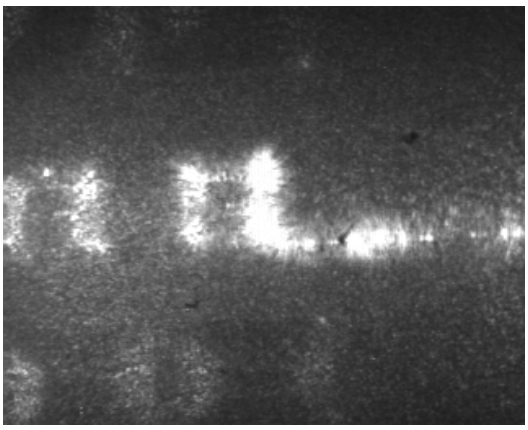

Figure 6.15: telecommunication wavelength light is traveling through the fabricated spiral waveguides.

A new set of a-SiC:H layers has been fabricated with a Tauc bandgap of 1.72 eV. In a collaboration with the optoelectronic research center at the Univseristy of Southampton the optical losses were measured with a prism setup. In this setup the light is coupled in a thin layer with a high refractive index prism. The scattering of the layer as a function of wavelength is measured with a fiber. The optical loss of the layer is measured by fitting the intensity of the light scattered as a function of the length. The light was coupled in the TM mode of the layer. The loss for the

first sample was found to be 1.8 dB/cm. The next step will be the processing of waveguides in the deposited layer with e-beam lithography.

6.2.3.4 Working at longer wavelengths

This section discusses some ongoing work. It has been carried out in the context of a master thesis by Sara Uvin (for which I am the supervisor) and Utsav Dave a newly started PhD student, working on nonlinear integrated optics. When the a-Si:H waveguide are pumped at longer wavelengths there is no two-photon absorption and thus no generated carriers. When there are no carriers generated, there is no degradation. To proof this concept, the a-Si:H waveguides are pumped by 2 ps pulses at 25 MHz by a mode locked thulium doped fiber light source. The waveguides had a width of 900 nm and a height of 220 nm. The strip waveguide used in this experiment is 1 cm long. A supercontinuum could easily be generated, as shown in 6.16. There was no observation of any degradation of the material, even after 3 hours of exposure to the source at peak powers of 30 W. Operating at 1950 nm instead of 2200 nm as in chapter 4 has several advantages, since many commercial sources are available for this wavelength as well as low loss cheap fibers.

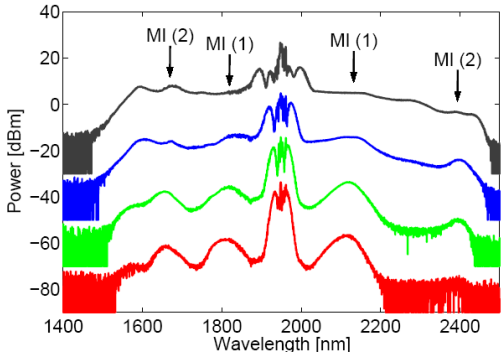

Figure 6.16: The output spectrum of the waveguide as a function of coupled input peak power. 6.4 W (red), 7.2 W (green), 9.5 W (blue) and 16.1 W (black). The spectra are vertically offset by multiples of 20 dB for clarity.

6.3 Conclusion

In this chapter the low nonlinear absorption of a-Si:H layers as compared to c-Si layers in the telecommunication window is demonstrated. Highly efficient nonlinear optical functions are demonstrated. Broadband parametric amplification as well as efficient all-optical sampling are shown. The metastability of the material,

the so called Staebler-Wronski effect, is observed and some directions are given to overcome this problem. The most promising one being, increasing the bandgap of the material by doping the layers with carbon. Another approach is shifting to longer wavelengths where any remaining two-photon absorption is absent.

6.4 Nonlinear properties of and nonlinear processing in hydrogenated amorphous silicon waveguides

The content of this section is published in Optics Express [15]

The a-Si:H photonic wire waveguides were fabricated in a 200 mm CMOS pilot line at imec, Belgium. First, 220 nm of a-Si:H was deposited using a low temperature Plasma Enhanced Chemical Vapor Deposition process on top of a 1950 nm surface of high-density plasma oxide on a silicon substrate. Waveguides of varying lengths (0.6 to 6 cm) were fabricated using 193 nm optical lithography and dry etching [1]. The photonic nanowires were interfaced to an optical fiber using grating couplers. The cross-section of these waveguides is 500220 nm^2 as can be seen in Fig 6.17.

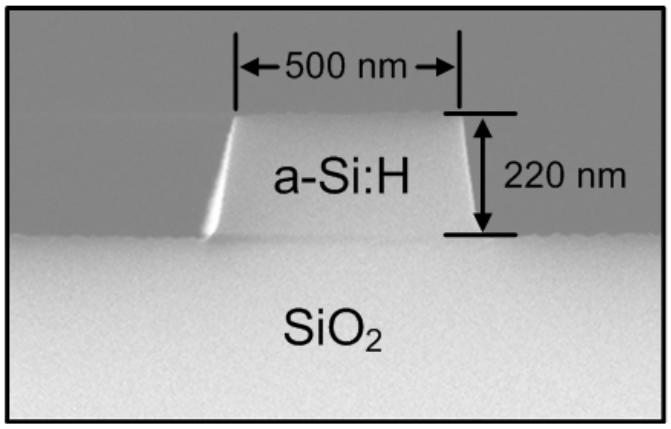

Figure 6.17: Cross-section of the hydrogenated amorphous silicon waveguides used in the experiments.

A preliminary report on the linear and nonlinear optical properties of these waveguides was given in [20]. Here we provide a more complete characterization, as well as details of the measurements that give rise to the parameters we reported previously. For an earlier study of the nonlinear optical properties of a-Si:H waveguides we refer to [12]. Using a cutback method the linear loss in the

photonic nanowires was determined to be 3.6 dB/cm. Grating coupler structures are used to couple the light in and out of the chip. The incoupling loss at 1550 nm was found to be 7 dB. The group velocity dispersion has been measured to be $\beta_2 = -2.0ps^2m^{-1}$ [20]. The nonlinear parameter of the photonic nanowires was measured by coupling in a picosecond pulse train. First, the time-averaged transmission of this picosecond pulse train (4ps, rep rate 10 MHz, center wavelength 1550 nm, spectral width 0.67 nm) in a sufficiently long (1.1 cm) photonic nanowire was measured as a function of the coupled input pulse peak power. It has been shown that the inverse of this transmission is linear as a function of the power [17] in the low power regime, when the free carrier absorption is negligible. The inverse of the transmission is given by [17]

$$\frac{1}{T} = exp(\alpha L)L_{eff}2Im(\gamma)P + exp(\alpha L) \tag{6.3}$$

Here, Im(γ) is the imaginary part of the nonlinear parameter, T is the transmission through the waveguide, L_{eff} is the effective length of the waveguide given by $L_{eff} = \frac{1-exp(-alphaL)}{alpha}$ is the length of the waveguide and α is the linear absorption coefficient of the waveguide. A linear fit as shown in Fig. 6.18 reveals a value of -28 ±3 $W^{-1}m^{-1}$ for the imaginary part of the nonlinear parameter. This moderate nonlinear absorption can be explained by examining the band gap of the a-Si:H, which was measured, using spectroscopic ellipsometry, to be 1.61 eV. This results in a two-photon absorption threshold wavelength of about 1540 nm.

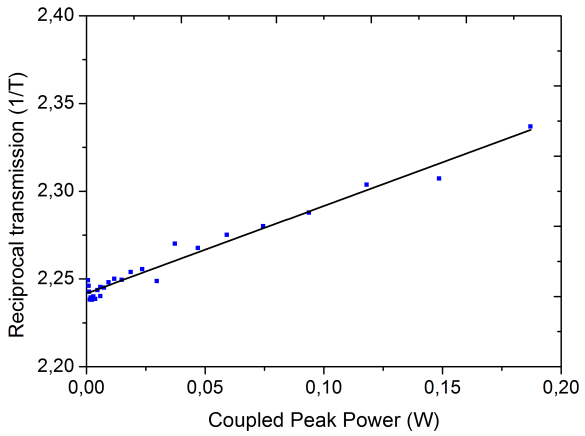

Figure 6.18: The reciprocal transmission as a function of the input peak power of the 4 ps pulse train. The linear fit corresponds to a nonlinear absorption coefficient of -28 ±3 $W^{-1}m^{-1}$.

Next, the free carrier lifetime was extracted in a pump/probe setup. The time

dependent absorption of a continuous wave (CW) laser by carriers created by a short probe by TPA is measured. As shown in Fig. 6.19, a low-power CW laser is combined with a high-power low repetition rate (20MHz) femtosecond laser source. The CW laser is operated at 1530 nm, while the fs laser is operating at 1550 nm such that a bandpass filter at the output only transmits the 1530 nm signal. The absorption of the low power CW signal caused by the carriers generated by the femtosecond source is measured as a function of time using a 40GHz high-speed photodiode connected to an oscilloscope. An exponential fit reveals a free carrier life time of 1.87 ±0.1 ns as can be seen in Fig. 6.20.

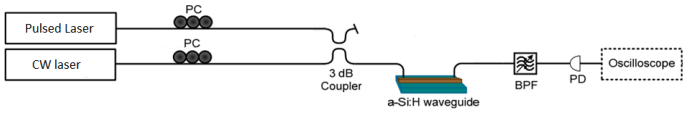

Figure 6.19: Experimental setup used to measure the free carrier lifetime in the hydrogenated amorphous silicon photonic nanowires.

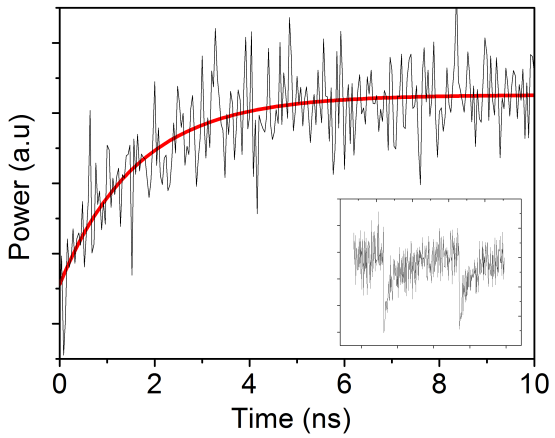

Figure 6.20: Oscilloscope trace of the pump/probe experiment and fit of the exponential decay of the carrier concentration, resulting in a time constant of 1.87 ±0.1 ns.

Finally, the real part of the nonlinear parameter was measured by determing the nonlinear phase shift of the 4 ps pulses in the a-Si:H wire waveguides as a function of input power. This nonlinear phase shift was extracted from the signature [21] of the self phase modulation spectra of the pulses after having propagated through a 1.1 cm long photonic wire. These nonlinear phase shifts were compared with simulations obtained by a split step algorithm that models the pulse propagation in a

nonlinear semiconductor photonic nanowire while taking into account the different forms of nonlinear absorption that occur in such a photonic nanowire. Agreement between the measured and simulated nonlinear phase shift allows the determination of the real part of the nonlinear parameter. In Fig. 6.21 the simulated output spectra as well as the measured output spectra are shown for a pulse peak power of 1.4, 2.9, 4.6 and 7.3 W. This method shows that the real part of the nonlinear parameter is 770 ±100 W-1m-1. By comparing the real and imaginary part of the nonlinear photonic nanowire a figure of merit (FOM) [26] can be defined as

$$FOM = -\frac{Re(\gamma)}{4\pi Im(\gamma)} \tag{6.4}$$

The extracted FOM of 2.2 at λ=1550nm for a-Si:H waveguides is almost four times higher than the value obtained in c-Si photonic nanowires [26].

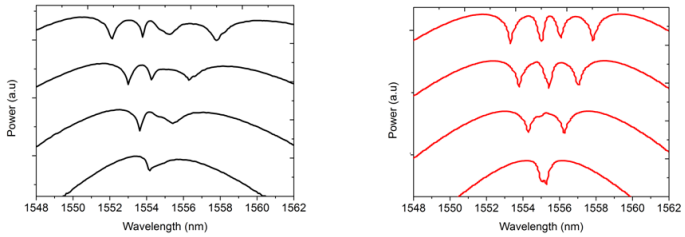

Figure 6.21: The simulated output spectra of a 4ps FWHM pulse train (right) and measured output spectra (left) for a coupled input peak power of 1.4, 2.9, 4.6 and 7.3W after propagation through a 1.1 cm long a-Si:H photonic nanowire.

To demonstrate the ultrafast large nonlinear response of the a-Si:H photonic nanowires, an optical waveform sampling experiment was performed in a 4 mm long waveguide. The setup of this experiment is shown in Fig. 6.22.

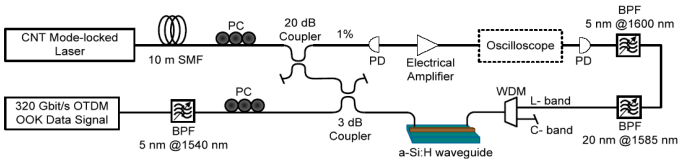

Figure 6.22: Experimental setup used in the 320 Gbit/s waveform sampling experiment.

A fiber ring mode-locked laser is used as the sampling source, which uses a 30 cm erbium-doped fiber as gain medium and a carbon nanotubes (CNT) mode-locker. The generated sampling pulses have a repetition rate of 16.3 MHz and a sech pulse shape with a FWHM width of $\approx$ 710 fs, measured using an autocorrelator directly at the laser output. The central wavelength of the pulses lies at 1558

nm and the 3-dB spectral bandwidth is 4 nm. The sampling pulses are broadened to 1.4 ps by adding 10 m single mode fiber (SMF) to avoid broadening by self phase modulation in the a-Si:H photonic nanowires. Using the Optical Time Division Multiplexing (OTDM) technique, a 320 Gbit/s serial data stream signal is generated. An erbium glass oscillator (ERGO) optical pulse source generates a 10 GHz pulse train at 1550 nm with 2 ps FWHM pulses. After amplification in an EDFA, the 10 GHz data pulses are sent into a dispersion-flattened highly nonlinear fiber (DF-HNLF) to broaden the spectrum. Then a 5 nm bandpass filter is used to filter out part of the spectrum. The pulse width of the 10 GHz pulses is compressed to 1 ps in this way. A Mach-Zehnder modulator encodes a 10 Gbit/s on-off keying (OOK) data sequence (PRBS $2^7 - 1$) on the pulse train and the 10 Gbit/s data signal is multiplexed to 320 Gbit/s by a passive fiber delay and polarization maintaining multiplexer (MUX). The 320 Gbit/s OTDM OOK data signal is coupled into the a-Si:H waveguide together with the sampling pulse train. The average data signal power and sampling pulse train power before coupling into the a-Si:H waveguide is 5 dBm and -5 dBm respectively. In the a-Si:H waveguide, FWM will take place when the sampling pulses (pump) overlap with the data pulses (signal) and generate a new FWM product (idler). After the a-Si:H waveguide, the FWM product is selected by L-band filters and directly detected using a high sensitivity photo-detector (with 200 MHz bandwidth). A tunable optical delay is inserted in the cavity of the sampling laser to fine tune the cavity length so that the repetition rate can be adjusted in a small range, this means in turn that the temporal offset, , between sampling and signal pulses can be adjusted.

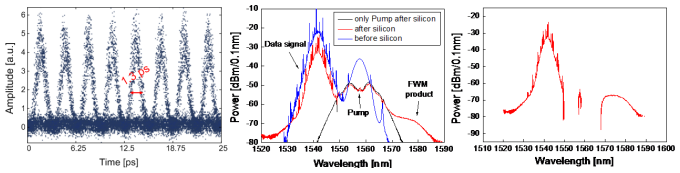

Figure 6.23: (Left) Sampled eye-diagram of the 320 Gbit/s serial data signal using the a-Si:H based optical sampling system, (Middle) Measured optical spectra before and after the a-Si:H waveguide, (Right) Spectrum of data signal and FWM product at output of waveguide when subtracting the pump.

This tunable temporal offset provides a simple synchronization scheme by only using the free running sampling pulses itself as a gate trigger for the oscilloscope. The measured spectra in the experiment are shown on Fig. 6.23 (middle). The output spectrum is broadened by SPM in the a-Si:H photonic nanowires. Fig. 6.23 (Right) shows the spectra of the data signal and FWM product at the output of the waveguide. The output power of the data signal and FWM product are integrated spectrally and measured to be $Pdata_{out}$ = - 14.5 dBm and $PFWM_{out}$ = - 44

dBm, respectively. The conversion efficiency, defined as the ratio between the FWM product power just before it is coupled out from the a-Si:H waveguide and the data signal power coupled into the a-Si:H waveguide, can be expressed as

$$\nu = (P_{FWMout} + l_{coupling}) - (P_{dataout} + l_{coupling}) \tag{6.5}$$

where $l_{coupling}$ is the coupling loss between fiber and waveguide (expressed in dB), and l is the propagation loss of the a-Si:H waveguide (1.5 dB for the 4mm long waveguide). When the duty cycle of the sampling pulse train (-43 dB) is taken into account, the intrinsic conversion efficiency ν is found to be +12 dB. This is an improvement of almost 19.5 dB as compared to a similar optical sampling system based on c-Si, where the intrinsic conversion efficiency was found to be merely -7.5 dB.

The strong nonlinearity in the a-Si:H manifests itself through strong modulation instability [21]. Evidence of modulation instability, the four wave mixing process where white background noise gets amplified, is shown in Fig. 6.24 (a). At the output of the photonic nanowire the spectrum of the pulse train shows sidelobes, resulting from the parametric amplification of the background noise. The pulses used in these experiments were 4-ps FWHM with a coupled peak power of 5.2 W and had a repetition rate of 10 MHz. The experiment shows that the amplification decreases with the time of exposure to the pump, resulting in weaker modulation instability side lobes. The observed decrease of the parametric amplification is believed to be the result of material degradation, probably originating from the Staebler-Wronski effect [8], well known in the a-Si solar cell community. Shortly after the first demonstration of thin-film amorphous silicon solar cells it was shown that these cells where not stable and that their efficiency decreases over time. It was found that this results from the degradation of the material, due to a process in which electron-hole pairs created by energetic photons recombine in the material. When the hydrogenated amorphous silicon photonic nanowires are exposed to telecom wavelengths it is unlikely that a substantial number of electron-hole pairs can be created by single photon absorption. However when high power pulses enter the photonic nanowires free carriers are created due to the presence of two-photon absorption. These free carriers can degrade the material following the Staebler Wronski mechanism. It was however demonstrated in amorphous silicon solar cells that the material can be restored to its original state by thermally annealing the sample. The same occurs for a-Si:H photonic chips. Here, the sample was heated at 200 degrees centigrade for 30 minutes and the effects of the degradation were reversed. Even after four iterations in which the sample is sequentially exposed to the bright pulses (4 ps, 5.2 W coupled peak power, 10 MHz rep rate) for 40 minutes and thermally annealed for half an hour the material was brought again to its original state. This is shown in Fig. 6.24 (b). In this figure the peak power in the side lobes is plotted versus time. Even after four iterations the curve shows

no deviation from the first iteration. It is also important to note that the nonlinear parameters from the waveguide were extracted after 30 minutes of exposure, when the material is in a quasi steady state.

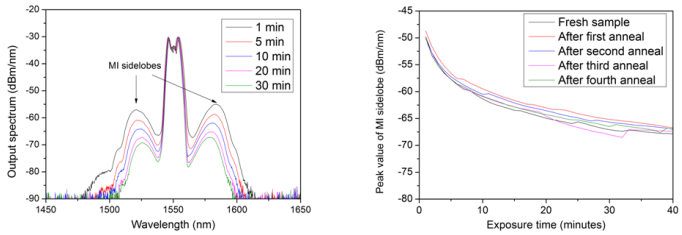

Figure 6.24: The modulation instability (MI) side lobes decrease over time (left) when the sample is exposed to intense light. The optical pulses in this experiment had their central wavelength at 1550 nm, had a repetition rate of 10 MHz and a FWHM of 4ps. The right figure shows the peak value of the right MI side lobe versus time, after successive thermal annealing steps of the sample at 200 degrees centigrade for 30 minutes.

The linear and nonlinear coefficients from the hydrogenated amorphous silicon photonic nanowires were extracted in this paper. The linear absorption was found to be 3.6 dB/cm while the nonlinear parameter was found to be $\gamma = 770 - j28W^{-1}m^{-1}$ after exposing the waveguides for 30 minutes. This results in a figure of merit larger than 2. The carrier lifetime was estimated to be 1.87 ±0.1 ns. The potential of the a-Si:H photonic nanowires for all-optical nonlinear processing was demonstrated by a 320 Gbit/s waveform sampling experiment. The intrinsic FWM conversion efficiency in this experiment was +12 dB. This is an improvement of 19.5 dB as compared to similar sampling experiments in c-Si. The degradation of the hydrogenated amorphous silicon layers is discussed. This degradation is presumably caused by a process similar to the Staebler-Wronski effect in amorphous silicon solar cells. As with the Staebler-Wronski effect in amorphous silicon cells, the degradation can be reversed by thermally annealing the sample. This was demonstrated by heating the sample for half an hour at 200 degrees centigrade. Improving the stability, for example by increasing the bandgap, could make the hydrogenated amorphous silicon photonic nanowires the platform for nonlinear integrated optics in the telecommunication wavelength range.

6.5 On-chip parametric amplification with 26.5 dB gain at telecommunication wavelengths using CMOS-compatible hydrogenated amorphous silicon waveguides

The content of this section is published in Optics Letters [20]

An important goal in photonics is to realize highperformance parametric amplifiers in integrated waveguide circuits. Ideally, this requires low-loss waveguides manufactured in materials with high Kerr nonlinearity, operating in the telecommunication window, realized using a complementary-metal-oxide-semiconductor (CMOS)-compatible fabrication platform. In this context, crystalline silicon (c-Si) waveguides have been studied extensively. However, their performance is limited by nonlinear absorption, resulting in wavelength conversion and parametric amplification gains limited to +5.2 dB and +4.2 dB, respectively [14], in this wavelength range. In order to overcome this problem, a first possibility is to use a cladding layer with a high figure of merit (FOM) [26, 27]. FOM is the ratio of the nonlinear response to the nonlinear absorption: $FOM = -\frac{Re(\gamma)}{4\pi Im(\gamma)}$ being the nonlinear parameter of the waveguide. However, the required evanescent coupling implies stringent design constraints that preclude good phase matching. A second approach is for the waveguide core itself to consist of a material with good FOM [28, 29], but these realizations suffer either from lower linear and nonlinear refractive indices or from incompatibility with CMOS fabrication. One can also step away from the telecommunication wavelength range and work above the c-Si twophoton absorption threshold wavelength of 2.2 μm [30]. Although this approach effectively improves the FOM of the c-Si waveguides, the use for telecommunication applications is not straightforward. Silicon-on-insulator (SOI) waveguides with a hydrogenated amorphous silicon (a-Si:H) waveguide core are an alternative to the standard crystalline SOI high-index contrast waveguide platform. An appealing feature of this solution is that a-Si:H is deposited at relatively low temperatures and can thus be integrated on a finished CMOS wafer in the back end. Recently, the nonlinear response of a-Si:H waveguides was studied [12], and the measured FOM was no better (0.40-0.66) than that of c-Si waveguides (0.4-0.7 [31]). Building on our previous work on low-loss a-Si:H waveguides [1], we present in this Letter engineered a-Si:H waveguides with a FOM of 2.1 ±0.4 at telecommunication wavelengths. A similarly high FOM value was reported in in an amorphous silicon core fiber. The difference from previous work [12] is presumably due to the fact that a-Si:H is a material with considerable freedom in chemical structure. Therefore different fabrication procedures can give rise to different material properties. The high linear refractive index of a-Si:H allows high optical confinement, which not only enhances the nonlinear response of the

waveguide, but also allows for dispersion engineering. By carefully designing the dimensions of the a-Si:H waveguide it is possible to bring the dispersion of the waveguide into the anomalous regime, which allows for nonlinear effects such as soliton propagation and modulation instability (MI). In this Letter we make use of the latter effect to construct a nonlinear parametric amplifier. The circuit is built in 220-nm-thick hydrogenated amorphous silicon deposited on top of a 1950-nm-thick polished high-density silicon dioxide layer. The 220-nmthick a-Si:H film is deposited by plasma-enhanced chemical vapor deposition. The film was formed using silane (SiH4) as a precursor gas along with helium (He) dilution. In order to achieve low losses, we used a gas ratio (He/SiH4) of 9 and a plasma power of 180 W at a pressure of 2.6 Torr. These typical parameters were obtained from extensive process optimizations [1]. After forming the waveguide core layer, 500-nm-wide photonic wires were patterned using CMOS fabrication technology. The bandgap of our a-Si:H films is measured using spectroscopic ellipsometry (in the 3001600nm range). The optical constants were extracted from a multilayer model using the CodyLorentz model and the recommendations of Ferlauto et al. In order to have an accurate result, the interface roughness was also taken into account as well as the film thickness measured independently by cross-section scanning-electron microscopy. By using seven fitting parameters, we obtained a bandgap of 1.613 ±0.022 eV (while c-Si has a gap of 1.12 eV). The half-bandgap is thus approximately 0.8eV, corresponding to $\lambda = 1550$ nm. Working around the half-bandgap gives rise to a high FOM. The single-mode waveguides we use are 500nm wide, and TE-polarized light is used in the experiments. Incoupling and outcoupling of light is realized using diffractive grating couplers, each inducing 7.58dB loss, depending on the wavelength. Waveguides with a variety of lengths were fabricated. Except where mentioned explicitly, all results are for waveguides with a length of 1.1cm. The fiber-to-fiber loss was measured for different waveguide lengths ranging from 6 mm to 6 cm at low input powers to extract the linear loss and the incoupling and outcoupling loss, which are assumed to be identical. The linear waveguide propagation loss at 1535 nm is 4.8dB/cm. The dispersion of the waveguides was estimated from a four-wave-mixing based conversion efficiency spectrum we measured at low power. Indeed, its bandwidth depends only on the propagation length and the group-velocity dispersion, $\beta_2 = -2ps2/m$. The negative sign of β_2 (anomalous regime) is deduced from the existence of MI (see below). These values are confirmed by numerical simulation using the commercial software Fimmwave (Photon Design, Oxford, UK), which predicts $\beta_2 = -2.6ps2/m$. The imaginary part of the nonlinear parameter, estimated by measuring the nonlinear dependence of the absorption, is $Im(\gamma)$ = - 28 ±3 $W^{-1}m^{-1}$. The real part of the nonlinear parameter, determined by comparing the dependence of the self-phase modulation fringes on input power with a simulation that takes into account dispersion, nonlinear absorption, and the presence

of free carriers, is Re(γ) = 770 ±100 $W^{-1}m^{-1}$, in agreement with the value obtained by studying photon pair production in these waveguides. During our measurements, we found that the nonlinear properties of our waveguides degrade with time, rapidly during the first minutes and then more slowly. Annealing the sample at 200 degrees centigrade for 0.5 h restores the FOM to its initial value (and this can be done multiple times). This suggests that with proper further optimization of the a-Si:H material, thermal excitation can compensate for photon-induced decay at moderate operating temperatures, possibly down to room temperature. All results reported in this Letter were taken after a few hours of operation, when the properties of the waveguides change slowly, and without annealing the sample. We intend to report on the decay properties for different temperatures in more detail in a future publication. Parametric amplification occurs in waveguides with Kerr nonlinearity and anomalous dispersion. When the phase-matching conditions are satisfied, a small signal detuned from the pump frequency by a frequency difference is exponentially amplified, while simultaneously an idler signal is created at detuning. This process can be used for both signal amplification and frequency conversion. We studied parametric amplification in an a-Si:H waveguide using a pumpprobe experiment; see Fig. 6.25. The pump was produced by a fiber laser emitting pulses at 1535 nm with a spectral width of 0.67 nm (FWHM), a duration of 3.8 ps (FWHM) at a 10MHz repetition rate. The peak power in the waveguide was adjusted from 0 to 5.3W thanks to a variable attenuator. Signal pulses are obtained from the secondary output of the laser: they are spectrally broadened using the optical nonlinearities in an erbium-doped fiber amplifier (EDFA), and then selected by a 1.2nm tunable passband filter to generate (signal) pulses at arbitrary wavelengths ranging from 1550 to 1590nm. The coupled peak power of the signal was always kept below 100W. An optical delay line was used to synchronize or desynchronize the signal and the pulse. After passing polarization controllers, the combined pump and signal were coupled into the waveguide. At the output of the waveguide, the light is sent to an optical spectrum analyzer. The parametric gain as a function of input pump power and signal wavelength was calculated after removing the effect of spontaneous MI. This was done by subtracting the MI spectrum when signal and pump are not synchronized from the output spectrum when they are synchronized. The on/off gain was calculated in a similar way as in [30] by integrating the power in the sideband caused by the amplification of the signal pulse. We obtained a maximum on/off gain of 26.5 dB and an on/off conversion efficiency of 27 dB for a signal at 1562 nm and an on-chip pump peak power of 5.3W. Taking into account propagation losses, this corresponds to a net on-chip amplification of 21.2 dB, resulting in enough gain to overcome the high incoupling and outcoupling losses, giving rise to 6.2 dB net offchip amplification.

The amplification as a function of the pump power at wavelength 1562 nm is plotted in Fig. 6.25 (c). This amplification is to be compared with the 4.2 dB on/off

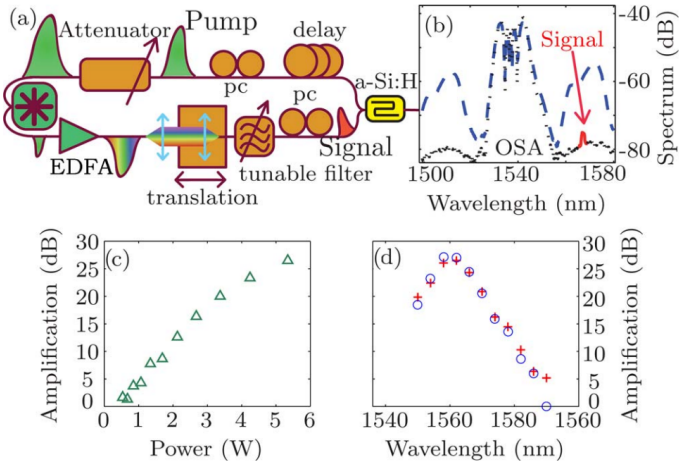

Figure 6.25: (Color online) Pump probe experiment. (a) Experimental setup combines an intense pump pulse with a signal pulse whose polarization (pc), frequency, and time delay can be adjusted. (b) When the pump (dotted curve) and signal (short dashed curve) pulses are not synchronized, the signal is very small in comparison to the pump pulse. If both pulses are synchronized (long dashed curve), signal pulses are amplified by more than 20dB and are converted into idler pulses. Note that the pump pulse is broadened spectrally due to self-phase-modulation, which in turn induces a broadening of the signal pulse. (c) On/off gain as a function of peak power. (d) On/off gain (resp. frequency conversion efficiency) as a function of wavelength.

amplification that was observed in crystalline silicon waveguide structures. Figure 6.25 (d) shows gain and conversion efficiency spectra for the peak pump power of 5.3W. On/off gain in excess of 20 dB was observed in the band 15501570nm, and on/off gain in excess of 10 dB was observed in the band 15501582nm. In the absence of a signal beam, the quasi-continuous nature of the pump pulse is broken by spontaneous MI. The spectra when only the pump pulse travels through the a-Si:H waveguide are shown in Fig. 6.26 for various pump power levels. The bandwidth and strength of the MI sidebands increase with coupled peak input power, while the pump itself also broadens due to self-phase-modulation. Note that MI peak can be related to amplification by comparison with the spectral density in the absence of MI. Spectral density at the MI-peak wavelength before a-Si:H chip is less than -80dB/nm and experiences 20dB fiber-to-fiber loss afterwards. The typical value of MI peak, above -70dBm/ nm, should thus be compared with background level below -100dB/nm, giving an amplification significantly greater than 30dB. The difference from the maximum gain reported in Fig. 1(c) is presumably because in the pump probe experiment, at maximum power, the pump starts to become depleted, which limits the gain. In summary, CMOS-compatible hydrogenated amorphous silicon waveguides provide on-chip parametric amplification

at telecommunication wavelengths. Optimization of the fabrication process could lead to further increases in the nonlinear figure of merit.

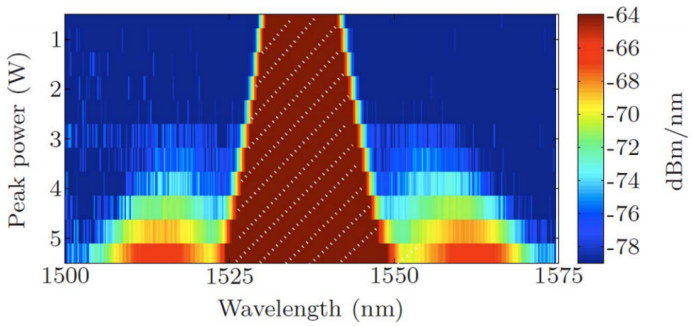

Figure 6.26: (Color online) MI spectra as a function of the input power, which is outside the range of the color coding at approximately -30dBm/nm.

References

[1] Shankar Kumar Selvaraja, Erik Sleeckx, Marc Schaekers, Wim Bogaerts, Dries Van Thourhout, Pieter Dumon, and Roel Baets. *Low-loss amorphous silicon-on-insulator technology for photonic integrated circuitry*. Optics Communications, 282(9):1767–1770, May 2009.

[2] WE Spear and PG Le Comber. *Substitutional doping of amorphous silicon*. Solid State Communications, 17(9):1193–1196, 1975.

[3] Francesco Giuseppe, Della Corte, and Sandro Rao. *Use of Amorphous Silicon for Active Photonic Devices*. IEEE Transactions on Electron Devices, pages 1–11, 2013.

[4] D L Staebler and C R Wronski. *Reversible conductivity changes in discharge-produced amorphous Si*. Applied Physics, 292(31), 1977.

[5] G Cocorullo, F G Della Corte, and I Rendina. *Amorphous silicon waveguides and light modulators for integrated photonics realized by low-temperature plasma-enhanced chemical-vapor deposition*. Optics Letters, 21(24):2002–2004, 1996.

[6] Runyu Yang and Jai Singh. *Study of the stability of hydrogenated amorphous silicon using tight-binding molecular dynamics*. Journal of Non-Crystalline Solids, 240(1-3):29–34, October 1998.

[7] M.J.M. Pathak, J.M. Pearce, and S.J. Harrison. *Effects on amorphous silicon photovoltaic performance from high-temperature annealing pulses in photovoltaic thermal hybrid devices*. Solar Energy Materials and Solar Cells, 100:199–203, May 2012.

[8] A K O Odziej. *Staebler-Wronski effect in amorphous silicon and its alloys*. 12(1):21–32, 2004.

[9] BG Yacobi, RW Collins, G Moddel, P Viktorovitch, and W Paul. *Effect of oxygen on the optoelectronic properties of amorphous hydrogenated silicon*. Physical Review B, 24(10):5907, 1981.

[10] Shankar Kumar Selvaraja, Wim Bogaerts, Dries VanThourhout, and Marc Schaekers. *Thermal trimming and tuning of hydrogenated amorphous silicon nanophotonic devices*. Applied Physics Letters, 97(7):071120, 2010.

[11] Karthik Narayanan, Ali W Elshaari, and Stefan F Preble. *Broadband all-optical modulation in hydrogenated-amorphous silicon waveguides*. Nature, 18(10):9809–9814, 2010.

[12] Yuya Shoji, Takeshi Ogasawara, Toshihiro Kamei, Youichi Sakakibara, Satoshi Suda, Kenji Kintaka, Hitoshi Kawashima, Makoto Okano, Toshifumi Hasama, Hiroshi Ishikawa, and Masahiko Mori. *Ultrafast nonlinear effects in hydrogenated amorphous silicon wire waveguide.* Optics Express, 18(6):5668–73, March 2010.

[13] Satoshi Suda, Ken Tanizawa, Youichi Sakakibara, Toshihiro Kamei, Kouichi Nakanishi, Emiko Itoga, Takeshi Ogasawara, Ryohei Takei, Hitoshi Kawashima, Shu Namiki, Masahiko Mori, Toshifumi Hasama, and Hiroshi Ishikawa. *Pattern-effect-free all-optical wavelength conversion using a hydrogenated amorphous silicon waveguide with ultra-fast carrier decay*. Optics Letters, 37(8):1382–1384, 2012.

[14] Mark a Foster, Amy C Turner, Jay E Sharping, Bradley S Schmidt, Michal Lipson, and Alexander L Gaeta. *Broad-band optical parametric gain on a silicon photonic chip.* Nature, 441(7096):960–3, June 2006.

[15] B Kuyken, H Ji, S Clemmen, S K Selvaraja, H Hu, M Pu, M Galili, P Jeppesen, G Morthier, S Massar, L K Oxenløwe, G Roelkens, and R Baets. *Nonlinear properties of and nonlinear processing in hydrogenated amorphous silicon waveguides.* Optics Express, 19(26):B146–53, December 2011.

[16] Dirk Taillaert, Peter Bienstman, and Roel Baets. *Compact efficient broadband grating coupler for silicon-on-insulator waveguides.* Optics Letters, 29(23):2749–51, December 2004.

[17] H. K. Tsang, R. V. Penty, I. H. White, R. S. Grant, W. Sibbett, J. B. D. Soole, H. P. LeBlanc, N. C. Andreadakis, R. Bhat, and M. a. Koza. *Two-photon absorption and self-phase modulation in InGaAsP/InP multi-quantum-well waveguides*. Journal of Applied Physics, 70(7):3992, 1991.

[18] R. M. Osgood, Jr., N. C. Panoiu, J. I. Dadap, Xiaoping Liu, Xiaogang Chen, I-Wei Hsieh, E. Dulkeith, W. M. Green, and Y. a. Vlasov. *Engineering nonlinearities in nanoscale optical systems: physics and applications in dispersion-engineered silicon nanophotonic wires*. Advances in Optics and Photonics, 1(1):162, January 2009.

[19] J M Dudley and J R Taylor. *Supercontinuum Generation in Optical Fibers*. Cambridge books online. Cambridge University Press, 2010.

[20] Bart Kuyken, Stéphane Clemmen, Shankar Kumar Selvaraja, Wim Bogaerts, Dries Van Thourhout, Philippe Emplit, Serge Massar, Gunther Roelkens, and Roel Baets. *On-chip parametric amplification with 26.5dB gain at telecommunication wavelengths using CMOS-compatible hydrogenated amorphous silicon waveguides.* Optics Letters, 36(4):552–4, February 2011.

[21] Govind P Agrawal. *Nonlinear fiber optics*. Springer, 2000.

[22] Robert A Street. *Hydrogenated amorphous silicon*. Cambridge University Press, 2005.

[23] J Tauc, R Grigorovici, and A Vancu. *Optical properties and electronic structure of amorphous germanium*, 1966.

[24] Assem M Bakry and Ahmed H El-Naggar. *Doping effects on the optical properties of evaporated a-Si: H films*. Thin Solid Films, 360(1):293–297, 2000.

[25] A Tabata, M Kuroda, M Mori, T Mizutani, and Y Suzuoki. *Band gap control of hydrogenated amorphous silicon carbide films prepared by hot-wire chemical vapor deposition*. Journal of non-crystalline solids, 338:521–524, 2004.

[26] C Koos, L Jacome, C Poulton, J Leuthold, and W Freude. *waveguides for all-optical signal processing*. Optics Express, 15(10):5524–5534, 2007.

[27] C Koos, P Vorreau, T Vallaitis, P Dumon, W Bogaerts, R Baets, B Esembeson, I Biaggio, T Michinobu, F Diederich, W Freude, and J Leuthold. *All-optical high-speed signal processing with silicon organic hybrid slot waveguides*. (March):1–4, 2009.

[28] Jacob S Levy, Alexander Gondarenko, Mark A Foster, Amy C Turner-foster, Alexander L Gaeta, and Michal Lipson. *Monolithically integrated multiple wavelength oscillator on silicon*. New York.

[29] Marcello Ferrera, David Duchesne, L Razzari, Marco Peccianti, Roberto Morandotti, Alessia Pasquazi, Yong-woo Park, Jose Azan, Brent E Little, Sai T Chu, and David J Moss. *Advanced Integrated Photonics in Doped Silica Glass*. 2012.

[30] Xiaoping Liu, Richard M. Osgood, Yurii a. Vlasov, and William M. J. Green. *Mid-infrared optical parametric amplifier using silicon nanophotonic waveguides*. Nature Photonics, 4(8):557–560, May 2010.

[31] H. K. Tsang, C. S. Wong, T. K. Liang, I. E. Day, S. W. Roberts, a. Harpin, J. Drake, and M. Asghari. *Optical dispersion, two-photon absorption and self-phase modulation in silicon waveguides at 1.5μm wavelength*. Applied Physics Letters, 80(3):416, 2002.

7

Reducing the effective carrier lifetime

This chapter briefly describes simulations and experiments that show how the effective carrier lifetime in a silicon photonic waveguide can be reduced, in order to reduce the detrimental free-carrier absorption. The free-carrier absorption is detrimental in nonlinear experiments in materials which suffer from parasitic two photon absorption and as such need to be avoided. It is demonstrated that by reducing the carrier lifetime in crystalline silicon, relative efficient nonlinear operations become possible in the telecommunication window.

7.1 Introduction

Instead of moving to a longer wavelength in crystalline silicon to eliminate nonlinear losses or use another material with lower nonlinear absorption at telecommunication wavelengths, the nonlinear absorption can be reduced be reducing the effective carrier lifetime in crystalline silicon waveguides. In crystalline silicon waveguides the free carrier absorption can be reduced by reducing the effective lifetime of the free carriers in the silicon waveguide (or at least the region which spatially overlaps with the optical mode). By reducing the free carrier lifetime in c-Si waveguides, c-Si waveguides can potentially be used for efficient nonlinear optical functions in the telecommunication window. It turns out that the absorption by the generated free carriers is much stronger than the two-photon absorption, even for modest cw power levels. This can be understood by looking at the equations governing the nonlinear absorption of continuous wave lasers. When

we assume a waveguide where the mode area is given by A_{eff} (we assume that the nonlinear modal area is equal to the linear modal area) and the two-photon absorption is given by β, then the absorption of light in such a waveguide where a carrier density of N per cubic meter is present, is given by the following differential equation [1]:

$$\frac{dI(z)}{dz} = [-\alpha - \beta I(z) - \sigma N]I(z) \tag{7.1}$$

Here I(z) is the optical intensity as a function of the propagation distance, α the linear absorption, β the two-photon absorption coefficient, σ the free carrier absorption coefficient [2]. The generation rate G of the carriers is proportional to the two-photon absorption rate, while the recombination rate of the carriers R is proportional to the carrier lifetime τ. In steady state, they are equal and given by

$$G = R \tag{7.2}$$

$$\frac{(\beta I(z))I(z)}{2\hbar\omega} = \frac{N}{\tau} \tag{7.3}$$

and thus

$$\frac{(\tau\beta I(z))I(z)}{2\hbar\omega} = N \tag{7.4}$$

Here it is assumed that for the absorption of light as a result of two-photon absorption that two absorbed photons create one electron. So the nonlinear absorption is described by

$$\frac{dI(z)}{dz} = [-\alpha - \beta I(z) - \sigma\frac{\tau\beta I(z)^2}{2\hbar\omega}]I(z) \tag{7.5}$$

Although the optical absorption as a result of the two-photon absorption coefficient scales linearly with the intensity, the nonlinear absorption as a result of the carriers scales with the square of the intensity. Already for modest powers the nonlinear absorption as a result of the carriers overcomes the two-photon absorption. This can be explicitly calculated for a standard waveguide shown in the inset of figure 7.1. The figure shows the total nonlinear absorption of a continuous wave signal as a function of input power as well as the nonlinear absorption caused by the two-photon absorption only. Here the imaginary part of the nonlinear parameter is assumed to be -50 $W^{-1}m^{-1}$ (see section 6.2). While the carrier lifetime is assumed to be 1 ns and the effective mode area $0.15um^2$.

Looking at equation 7.5, reducing the carrier lifetime can thus clearly lower the nonlinear loss in the waveguide. The effective carrier lifetime in a silicon waveguide can be lowered by introducing defects to trap generated carriers in a waveguide. In [3], for example ion implantation was used to make defect states. However the defects states increase the linear loss significantly. Another approach

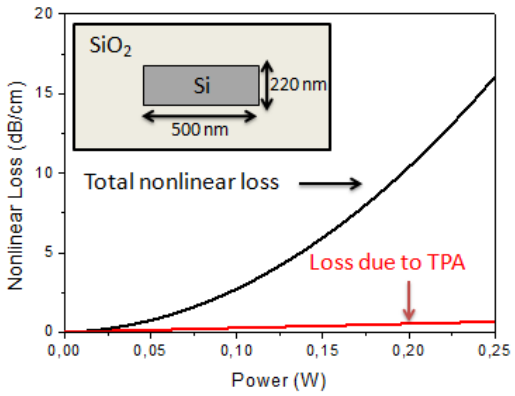

Figure 7.1: The nonlinear absorption of a silicon waveguide. The inset shows the dimensions of the waveguide used in the simulation. The graph shows the absorption in dB/cm as a function of the input power.

is to apply an electric field over the silicon waveguide: generated carriers will get accelerated in that field and move out of the region where the optical mode is. This approach is schematically shown in figure 7.2. The doped silicon regions and the metal are spatially far from the optical mode such that they do not introduce any excess linear loss. Such a structure can be simulated in software such as Silvaco © [4] (with the help of ir. Martijn Tassaert). The effective carrier lifetime of the carriers in the waveguide is shown in figure 7.3. According to the simulation a voltage of approximately 5 V is enough to reduce the carrier lifetime to 10 ps.

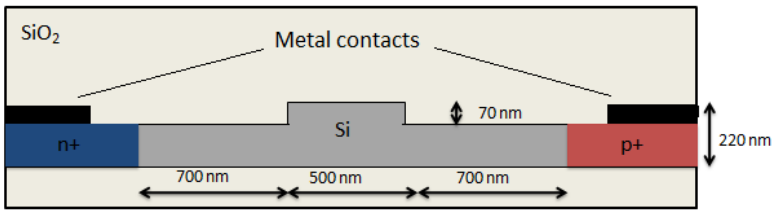

Figure 7.2: The figure shows schematically how a PIN structure that can be used to sweep carriers out of a waveguide region looks like. When a voltage is applied over the junction such that it is reversely biased the strong internal electric field over the waveguide will sweep the carriers out of the waveguide region

In fact, by reducing the carrier lifetime to 10 ps, simulation show that the excess nonlinear loss in such a waveguide due to nonlinear absorption can be very limited. Figure 7.4 shows the excess nonlinear loss of the waveguide shown in figure 7.2. The excess nonlinear loss can be lower than 1 dB/cm for 250 mW continuous wave signals. Here it was assumed that the imaginary part of the nonlinear

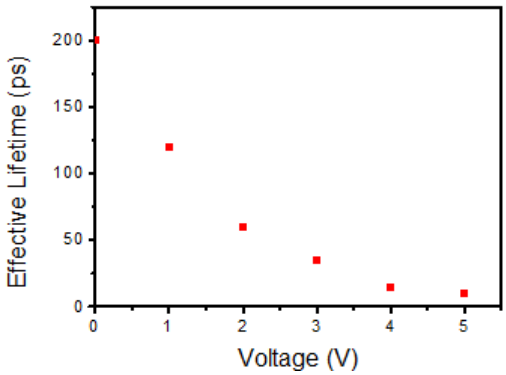

Figure 7.3: The figure shows the simulated effective carrier lifetime as a function of the voltage which is applied over the reversely biased diode. A voltage of about 5 V is enough to reduce the carrier lifetime down to 10 ps.

parameter was $-30W^{-1}m^{-1}$. This waveguide design is compatible with the processes available at imec to make modulators. Although the dispersion can not be made low or anomalous, such a waveguide allows for net amplification of continuous wave signals when the pump wavelength is close to the signal wavelength. For example for the waveguide shown in the inset in figure 7.4 the dispersion is $\approx 1.56ps^2/m$ which leads to a phase mismatch in the four wave mixing process (see section 3) of $\approx 3.7/m$ when the pump and signal are separated by 2 nm. When we assume that the real part of the nonlinear parameter of such a waveguide is 250 $W^{-1}m^{-1}$ around 1550 nm, we can have on chip net-gain when the linear loss is sufficiently low. Waveguide losses for rib waveguides similar as in 7.2, without the doping have shown to be as low as 0.3 dB/cm [5]. Figure 7.5 shows the simulated power in dBm when a small signal is combined with a 250 mW pump in the silicon waveguide when the carriers are swept out of the waveguide with such a lateral junction. The nonlinear parameter is assumed to be 250 - j36 $W^{-1}m^{-1}$ while the carrier lifetime is 10 ps. It is possible to have some net gain in a silicon waveguide when the carrier lifetime is reduced to 10 ps. At the time of writing a 2 and 3 cm long waveguide with the discussed carrier sweep out structure is being processed in the cleanroom of imec.

7.1.1 Reduction of the effective free carrier lifetime in literature

Researchers at Intel have demonstrated the first Raman laser in 2005 [6] by employing this trick in their thick micron wide waveguides. They were able to lower the carrier lifetime to $\approx$ 1 ns by applying a voltage of 25 V. The nonlinear gain by the Raman effect was higher than the round trip losses caused by the linear losses

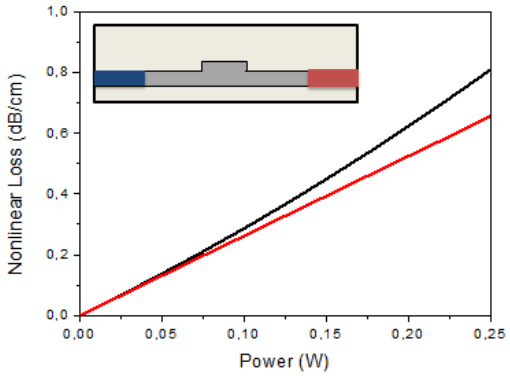

Figure 7.4: The nonlinear absorption of a silicon waveguide with a PIN. The inset shows the dimensions of the waveguide used in the simulation. The graph shows the absorption in dB/cm as a function of the input power. The total nonlinear absorption is in black, while the absorption due to two-photon absorption is shown in red.

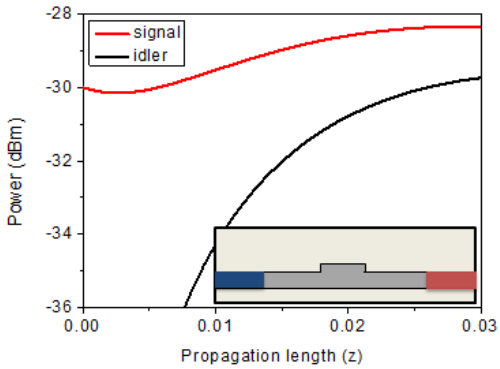

Figure 7.5: The figure shows the simulated power in dBm of an applied signal as a function of time. The converted idler is also shown. After approximately 3 cm net gain is achieved for the applied signal.

as well as the nonlinear losses which enabled lasing in the device. More recently researchers from Cornell in 2010 [7] demonstrated a carrier lifetime as low as 10 ps. In Germany a PIN sweep out structure was used to achieve record conversion efficiency [8] in a silicon waveguide. However due to the high (linear) losses in their waveguides net gain was not possible.

7.1.2 Low cost alternative to sweep out carriers

A simple approach to lower the carrier lifetime without the use of doped regions is to contact the silicon directly without the doped regions. By doing this we make

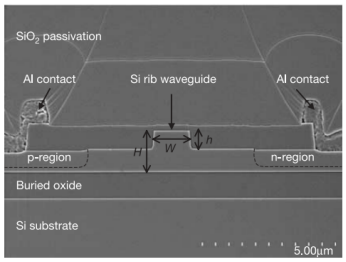

Figure 7.6: The figure shows the PIN junction to sweep out carriers to lower the nonlinear absorption to achieve net gain.

a sort of metal semiconductor metal detector. When putting a voltage across the waveguide one of the two metal semiconductor interfaces will work as a reversely biased Schottky diode which causes a high voltage drop and thus a low electric field over the waveguide. It was analyzed whether the electric field was strong enough to reduce the carrier lifetime significantly. A silicon waveguide with an oxide cladding has low losses due to the reduced difference in refractive index between the waveguide core and the cladding. The process used in this work was done on a set of high Q resonators. After processing, the loaded Q factor of the rings was measured to be the same. The transmission spectrum of the rings after processing is shown in figure 7.7. The line width of the resonance is 4.2 pm, making the Q factor as high as 386000. The process flow is shown in figure 7.8.

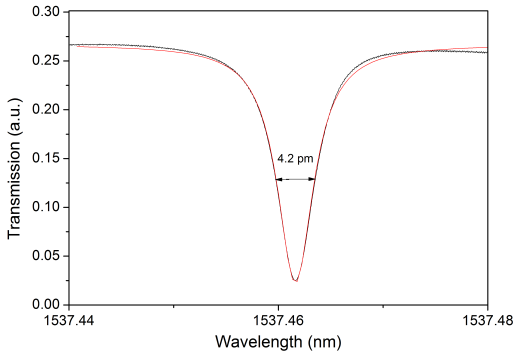

Figure 7.7: Q factor of processed ring resonator. The deposition of the metal layer did not affect the linear loss in the ring. The Q factor after processing was 386000.

First the oxide was opened where the metal contacts needed to be deposited. To protect the oxide elsewhere photosensitive SU8-2 was spin coated at 1000 rpm for 30 s on the sample and exposed for 10 s with UV400 with an appropriate mask with contact lithography. The measured thickness of the photo resist layer was

3.5 μm. After which the samples were dry etched for 22 minutes with SF6/O2 mixture. Then, the samples were wet etched with a HF/water solution (in 1:3 ratio) for 15 s. The wet etch step made sure that the silicon itself was not etched because HF does not attack the silicon. A second lithography step was done on the samples using standard AZ5214 (exposure 15 s) resist (the same mask was used). The resist was removed and a 600 nm Ti/Au layer was deposited on the sample. The process finished with a lift off step. The result can be seen in figure 7.9. Next to ring resonators, some straight waveguides were processed in the same way as well. Figure 7.10 shows a waveguide with metal contacts at both sides.

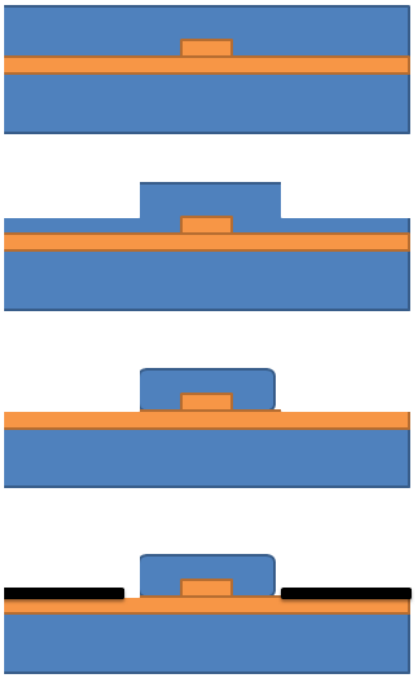

Figure 7.8: The process flow to deposit metal contacts next to a rib waveguide. First the oxide is partially opened with a dry etch to remove most of the oxide, after which the remaining oxide is removed with a HF wet etch. Finally the metal is deposited.

These waveguide were used to measure the effective carrier lifetime in the waveguide. The experimental setup to measure the free carrier lifetime is shown in figure 7.11. High power fs pulses (at 1550 nm) were combined with a cw laser (at 1520 nm) and were coupled to the silicon waveguide. The high peak power pulses create free carriers which modify the cw signal. At the output a Band Pass Filter (BPF) filters out the cw signal which is at a different wavelength than the pulsed source. This signal is monitored with a fast photodiode. The time trace

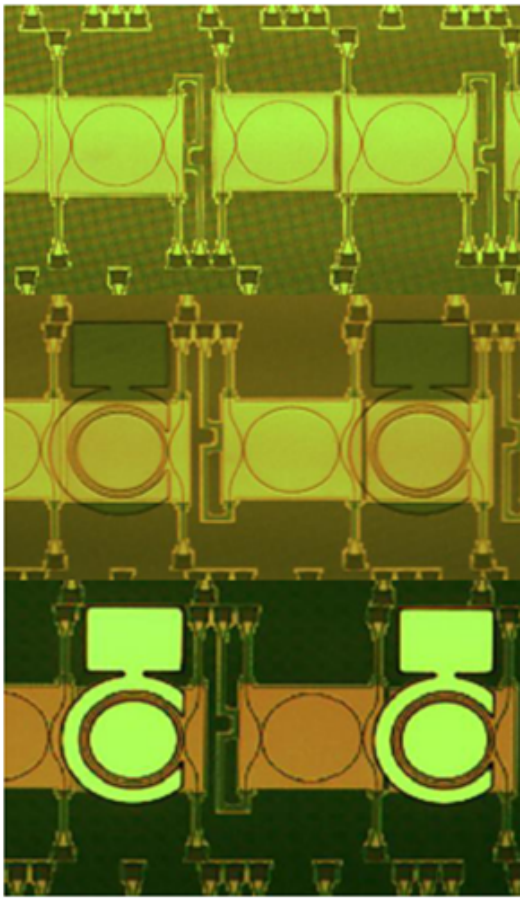

Figure 7.9: A rib waveguide with metal contacts to sweep out the carriers.

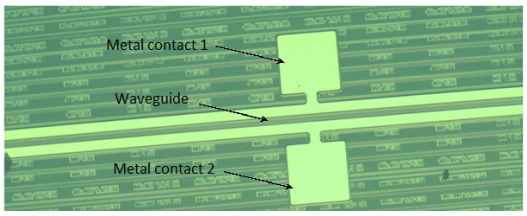

Figure 7.10: A rib waveguide with metal contacts to sweep out the carriers.

coming from the photodiode is monitored and reveals the lifetime of the carriers in the waveguide. Figure 7.12 shows the time trace recorded on the oscilloscope when the metal contacts at both sides of the rib waveguide are in open circuit. By

fitting an exponential function to the trace a carrier lifetime of 2.76 ns is found. Next, a voltage is applied at the metal contacts. The time traces are shown on Figure 7.13 for a set of voltages, by fitting an exponential function to these traces, the lifetime as a function of voltage is calculated. The lifetime as a function of applied voltage is shown in Figure 7.14. It can be seen on the time traces that part of the fs pulse is not filtered out of the cw signal. This is because the fs pulse spectrally broadens in the chip such that it spectrally overlaps with the cw signal and cannot be filtered out completely. This makes it hard to fit carrier lifetimes below 100 ps.

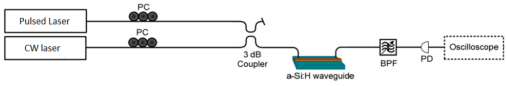

Figure 7.11: The setup used to measure the carrier lifetime.

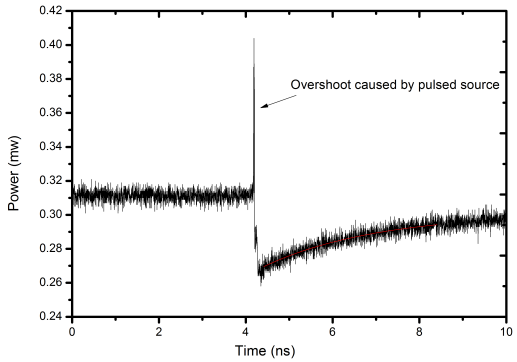

Figure 7.12: The time trace on the photodiode when the metal contacts are in open circuit. An exponential fit reveals a lifetime of 2.76 ns.

7.1.3 Conclusion

The chapter briefly reviews how the nonlinear loss in a silicon waveguide can be reduced by lowering the effective carrier lifetime in the waveguide. The effective carrier lifetime can be reduced by applying an electric field over the waveguide. For a PIN structure, by removing the carriers, this allows to lower the effective lifetime down to 10 ps. It is simulated that in low loss (0.3 dB/cm) waveguides with sufficient interaction length net on-chip gain becomes possible in the telecommunication window in cw. Such structures have been designed and are being processed in the cleanroom at imec. Additionally a cheap alternative to reduce the carrier

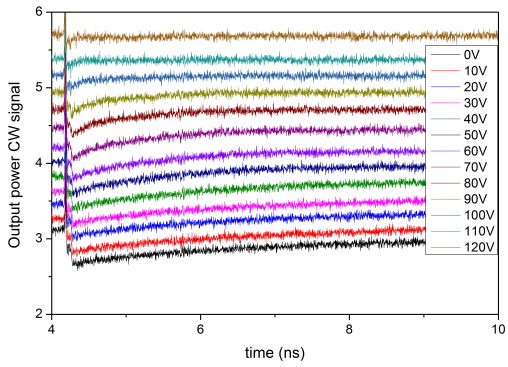

Figure 7.13: The time traces recorded by the photodiode for a set of voltage applied over the metal contacts.

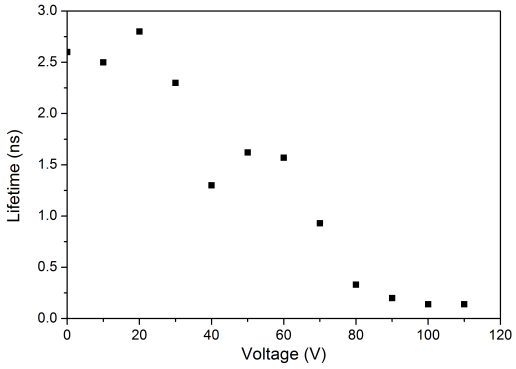

Figure 7.14: The carrierlife as a function of the applied voltage over the rib waveguide.

lifetime is demonstrated. The method is based on a metal-semiconductor-metal structure and carrier lifetimes of about 100 ps are demonstrated.

References

[1] Q Lin, Oskar J Painter, and Govind P Agrawal. *Nonlinear optical phenomena in silicon waveguides: modeling and applications.* Optics Express, 15(25):16604–44, December 2007.

[2] Richard Soref and J Larenzo. *All-silicon active and passive guided-wave components for λ= 1.3 and 1.6 μm.* Quantum Electronics, IEEE Journal of, 22(6):873–879, 1986.

[3] N M Wright, D J Thomson, K L Litvinenko, W R Headley, a J Smith, a P Knights, J H B Deane, F Y Gardes, G Z Mashanovich, R Gwilliam, and G T Reed. *Free carrier lifetime modification for silicon waveguide based devices.* Optics Express, 16(24):19779–84, November 2008.

[4] S Michael, A D Bates, and M S Green. *Silvaco Atlas as a solar cell modeling tool*. In Photovoltaic Specialists Conference, 2005. Conference Record of the Thirty-first IEEE, pages 719–721. IEEE, 2005.

[5] W Bogaerts and S K Selvaraja. *Compact Single-Mode Silicon Hybrid Rib/Strip Waveguide With Adiabatic Bends*. IEEE Photonics Journal, 3(3):422–432, June 2011.

[6] Haisheng Rong, Richard Jones, Ansheng Liu, Oded Cohen, Dani Hak, Alexander Fang, and Mario Paniccia. *A continuous-wave Raman silicon laser*. Nature, 433(7027):725–728, 2005.

[7] Amy C Turner-Foster, Mark a Foster, Jacob S Levy, Carl B Poitras, Reza Salem, Alexander L Gaeta, and Michal Lipson. *Ultrashort free-carrier lifetime in low-loss silicon nanowaveguides.* Optics Express, 18(4):3582–91, February 2010.

[8] Andrzej Gajda, Lars Zimmermann, Mahmoud Jazayerifar, Georg Winzer, Hui Tian, Robert Elschner, Thomas Richter, Colja Schubert, Bernd Tillack, and Klaus Petermann. *Highly efficient CW parametric conversion at 1550 nm in SOI waveguides by reverse biased p-i-n junction.* Optics Express, 20(12):13100–7, June 2012.

8 Conclusions and perspectives

8.1 Conclusions

The ultrafast optical Kerr effect is an ultrafast, broadband nonlinear effect which is very strong in crystalline silicon. By making nanophotonic waveguides out of silicon, light can be squeezed in a very tiny cross section. The intense electric fields in the silicon waveguides enhance the nonlinear interaction further. In this work, these highly nonlinear waveguides were used to demonstrate ultra-fast all-optical signal processing in the telecommunication wavelength window and to generate light in the mid-infrared.

All-optical signal processing in the telecommunication wavelength window All-optical signal processing in crystalline silicon nano waveguides has been demonstrated before, however the efficiency of the nonlinear processes has been limited due to the presence of two-photon absorption in crystalline silicon. In this work two solutions are proposed and proven to overcome this problem.

This first solution is to move away from crystalline silicon and look for another, preferably CMOS compatible material, with a high nonlinear refractive index and a low two-photon absorption coefficient. It is found that waveguides made out of hydrogenated amorphous silicon have a much lower two-photon absorption coefficient, while the Kerr nonlinearity is higher than the one found in crystalline silicon waveguides. Additionally the waveguides can be fabricated in a CMOS fab on a wafer scale. Using these waveguides, an all-optical amplifier was built.

The parametric amplifier is able to amplify signals up to 26 dB. This is an improvement of more than 20 dB over previous demonstrations in crystalline silicon waveguides. Furthermore an all-optical wave form sampling experiment of a 320 GBit/s data stream was performed with an efficiency of 12 dB, 20 dB better than obtained in similar experiments in crystalline silicon. These experiments show the potential for hydrogenated amorphous silicon to do all optical processing in the telecommunication wavelength window. At the moment the meta-stability in the hydrogenated amorphous silicon waveguides, however, is still an issue that needs to be resolved.

The second solution is using a mid-infrared pump source to manipulate the telecommunication signals. The photon energies of the mid-infrared pump are sufficiently low to suppress or eliminate the two-photon absorption. In this work it is shown that by using a mid-infrared source telecommunication signals can be amplified. Extensive dispersion engineering is needed to get the telecommunication signals (and idler) phase matched with the pump. This is successfully demonstrated in a experiment were a pump in the mid-infrared amplifies a telecommunication signal.

Generation of light in the mid-infrared The mid-infrared wavelength region (2 μm - 8 μm) is a very interesting wavelength region for spectroscopic applications because many molecular bonds have specific absorption lines in this wavelength region. However, sources in these wavelength region are not readily available. In this work it is shown that by using the strong nonlinear Kerr effect in crystalline silicon light can be generated in the mid-infrared. In a experiment where narrow band pulses centered around 2120 nm were spectrally broadened through the process of supercontinuum generation, the generation of a white spectrum spanning from 1535 nm up to 2525 nm is shown. Next, by nonlinear mixing of telecommunication signals (1565 nm) and a mid-infrared pump (2190 nm) it is shown that a mid-infrared signal at 3630 nm can be generated. Furthermore a widely tunable optical parametric oscillator (OPO) is demonstrated. The OPO uses a silicon chip as a gain medium and a fiber loop for feedback. The OPO is tunable over 70 nm near 2075 nm. These different demonstrations show the enormous potential of the silicon-on-insulator technology as a nonlinear platform to make tunable sources in the mid-infrared.

8.2 Perspectives

A pulsed source has mostly been used throughout the work to get strong nonlinear effects. Demonstrating these nonlinear optical functions in a continuous wave regime would be a major stepping stone towards applications. Working with continuous wave pumps with lower power means that resonant structures are needed

to achieve high powers in structures. For example, by using silicon nitride ring resonators octave spanning frequency combs have been demonstrated, despite the low nonlinearity of silicon nitride. Similar demonstrations should be possible in silicon resonators. Another way of reducing the power needed for a nonlinear process is by increasing the interaction length. However, increasing the length of a waveguide to increase the interaction length is only useful when the linear propagation loss is sufficiently low. The propagation loss of the silicon waveguides has steadily decreased because of better fabrication techniques over the past few years. When sufficiently low propagation loss (0.1dB/cm) is achieved net cw conversion in silicon waveguides will be possible at low pump powers ($\approx$ 50 mW). Furthermore as simulated in this work chip scale widely tunable optical parametric oscillators would become possible.

A

Mathematical description of nonlinear optical phenomena

This appendix handles the mathematical description of waves traveling through a nonlinear medium. Several simplifications are used, for example it is assumed that the medium is isotropic.

A.1 Nonlinear optical Medium

The main difference between a linear and a (classic) nonlinear optical medium is that the induced polarization by the electric field is a nonlinear function of the electric field instead of being a linear function of it. Mathematically the induced polarization in a linear material by an electric field can be written as follows

$$\mathbf{P}(\vec{t}) = \epsilon_0 \int_{-\infty}^{\infty} \chi^1(t - t^{'}).\vec{\mathbf{E}}(\vec{\mathbf{r}}, t^{'})dt^{'} \tag{A.1}$$

In the frequency domain this can be written as

$$\mathbf{P}(\vec{\omega}) = \epsilon_0 \chi^1(\omega)\mathbf{E}(\vec{\omega}) \tag{A.2}$$

Here $\chi^1(\omega)$ is the Fourier transform of the impulse response of the susceptibility of the material

$$\chi^1(\omega) = \int_{-\infty}^{\infty} \chi^1(t) exp(j\omega t)dt \tag{A.3}$$

Solving the Maxwell equations in a linear (non magnetic) medium is rather simple, with the previous equation. Starting from the Maxwell equations

$$\nabla \times \vec{\mathbf{E}} = -\frac{\partial \vec{\mathbf{B}}}{\partial t} \tag{A.4}$$

$$\nabla \times \vec{\mathbf{H}} = \vec{\mathbf{J}} + \frac{\partial \vec{\mathbf{D}}}{\partial t} \tag{A.5}$$

$$\nabla \cdot \vec{\mathbf{D}} = \rho \tag{A.6}$$

$$\nabla \cdot \vec{\mathbf{B}} = 0 \tag{A.7}$$

Here, $\vec{\mathbf{E}}$ is the electric field vector in the material, $\vec{\mathbf{E}}$ is the magnetic field vector in the material $\vec{\mathbf{D}}$ the electric field flux density and $\vec{\mathbf{B}}$ the magnetic field flux density. The latter two are created as a result of the first two. They obey the following equation

$$\vec{\mathbf{D}} = \epsilon_0 \vec{\mathbf{E}} + \vec{\mathbf{P}} \tag{A.8}$$

$$\vec{\mathbf{B}} = \mu_0 \vec{\mathbf{H}} + \vec{\mathbf{M}} \tag{A.9}$$

Here ϵ_0, μ_0 are the permittivity and permeability of the vacuum respectively, while $\vec{\mathbf{P}}$ and $\vec{\mathbf{M}}$ are the induced electric and magnetic polarization. In a non magnetic material the latter is zero. Taking the curl of A.4 we get

$$\nabla \times \nabla \times \vec{\mathbf{E}} = -\nabla \times \frac{\partial \vec{\mathbf{B}}}{\partial t} \tag{A.10}$$

$$\tag{A.11}$$

Inserting A.9 when assuming that the medium is nonmagnetic, we get

$$\nabla \times \nabla \times \vec{\mathbf{E}} = -\epsilon_0 \nabla \times \frac{\partial \vec{\mathbf{H}}}{\partial t} \tag{A.12}$$

Inserting A.5 at the right hand side, assuming there are no free charges ($\rho_f = 0$) and thus $\vec{\mathbf{J}} = 0$ and taking A.8 in account we get.

$$\nabla \times \nabla \times \vec{\mathbf{E}} = -\frac{\partial^2 \vec{\mathbf{E}}}{c^2 \partial t^2} - \mu_0 \frac{\partial^2 \vec{\mathbf{P}}}{\partial t^2} \tag{A.13}$$

When we assume that the medium is linear and by going to the frequency domain, such that we can use A.2 the equation becomes

$$\nabla \times \nabla \times \vec{\mathbf{E}} = \frac{\omega^2 \vec{\mathbf{E}}}{c^2} + \mu_0 \omega^2 \epsilon_0 \chi^{(1)} \vec{\mathbf{P}} \tag{A.14}$$

Now, taking in account the following identity

$$\nabla \times \nabla \times \vec{\mathbf{E}} = \nabla(\nabla \times \vec{\mathbf{E}}) - \nabla^2 \vec{\mathbf{E}} \tag{A.15}$$

and taking in account that $\nabla \times \vec{\mathbf{E}} = \epsilon \nabla \times \vec{\mathbf{E}} = 0$ in case ϵ is independent of the spatial coordinates. The equation becomes

$$\nabla^2 \vec{\mathbf{E}} + n^2 \frac{\omega^2}{c^2} \vec{\mathbf{E}} = 0 \tag{A.16}$$

with

$$n^2 = 1 + \chi^{(1)} \tag{A.17}$$

However when the polarization is nonlinear, this becomes more difficult. For a given polarization, the polarization is not proportional with the electrical field. When the polarization is nonlinear we can rewrite the polarization as

$$\vec{\mathbf{P}}(\vec{\mathbf{r}}, t) = \vec{\mathbf{P}_L}(\vec{\mathbf{r}}, t) + \vec{\mathbf{P}_{NL}}(\vec{\mathbf{r}}, t) \tag{A.18}$$

Here the nonlinear polarization can be approximated by a Taylor series as

$$\vec{\mathbf{P}(t)}_{NL} = \epsilon_0 \chi^2 \vec{\mathbf{E}^2} + \epsilon_0 \chi^3 \vec{\mathbf{E}^3} + ... \tag{A.19}$$

The material used in this work is silicon, which has a centrosymmetric crystal structure. The second order nonlinear polarization is these materials is zero. This can be proven by assuming that there is a second order nonlinearity and proving that it is zero: when there would be a second order nonlinearity in the material, the second order nonlinear polarization would be given by

$$\vec{\mathbf{P}(t)}_{NL} = \epsilon_0 \chi^2 \vec{\mathbf{E}} \tag{A.20}$$

The medium is centro symmetric, which means that if we apply the opposite electric field the polarization also needs to be opposite. This because the material itself is centro symmetric and reacts thus in the same way for the electric field if it is inversed. This means that

$$\text{-}\vec{\mathbf{P}(t)}_{NL} = \epsilon_0 \chi^2 \text{-}\vec{\mathbf{E}}^2 \tag{A.21}$$

However the right hand side of the equation is also equal to $\epsilon_0 \chi^2 \vec{\mathbf{E}}^2$. So this means that $\text{-}\vec{\mathbf{P}(t)}_{NL} = \vec{\mathbf{P}(t)}_{NL}$ which means that there is no second order nonlinearity

The third order nonlinearity is silicon is thus the most dominant one. There are two major contributions. One comes from the bound electrons in the silicon and is very fast (10fs) such that it can be considered to be instantaneous. The other contribution is coming from the optical phonons. This effect is called the

Raman response. This effect is not instantaneous. Because the response is not instantaneous at all, the bandwidth of the latter is limited. The effect is too slow to follow very rapid changes. In this work it is the broadband, fast third order nonlinearity which is exploited such that

$$\mathbf{P}(\vec{t})_{NL} = \epsilon_0 \chi^3 \vec{\mathbf{E}}^3 \tag{A.22}$$

This means that we can rewrite A.16 as

$$\nabla^2 \vec{\mathbf{E}} + n^2 \frac{\omega^2}{c^2} \vec{\mathbf{E}} = -\mu_0 \omega^2 \vec{\mathbf{P}}_{NL} \tag{A.23}$$

with $\mathbf{P}(\vec{t})_{NL} = \epsilon_0 \chi^3 \vec{\mathbf{E}}^3$, which means that the nonlinear polarization acts as a source term.

A.1.1 Four wave mixing

As discussed before, the nonlinear polarization act as a source term. When several waves are present in a nonlinear system they can interact, when the nonlinearity of the medium is a third order nonlinearity this interaction is called four wave mixing. As a result of four wave mixing, a weak signal can get amplified and converted to another frequency. When there are four wave present in a nonlinear medium at optical frequencies ω_j and propagation constant k_j, for simplicity, they are assumed to excite the same optical mode, with field distribution F(x,y):

$$E_j(x,y,t) = \frac{1}{2} E_{\omega_j}(x,y,z)(exp[(i(k_j z - \omega_j t)] + c.c.) \tag{A.24}$$

with $E_{\omega_j}(x,y,z) = F(x,y)A_j(z)$ and $A_j(z)$ the slowly varying amplitude of the optical wave j the total electric field in the mode becomes

$$E_j(t) = \sum_{1..4} \frac{1}{2} E_{\omega_j}(z)(exp[(i(k_j z - \omega_j t)] + c.c.) \tag{A.25}$$

When we assume that the third order nonlinearity is instantaneous and isotropic the nonlinear polarization is given by

$$P^3_{NL} = \epsilon_0 \chi^3 E^3 \tag{A.26}$$

such that the nonlinear polarization becomes, after substituting the electric field

$$P^{(3)}_{NL} = \frac{1}{2} \sum_{n=1..4} P_{\omega_n} e^{j\omega_n t - k_n z} + c.c.) \tag{A.27}$$

Here it can be shown that for example

$$P^{(3)}_{\omega_4} = \frac{3}{4}\chi^{(3)} {E_{\omega_4}}^2 E_{\omega_4} + \frac{6}{4}\chi^{(3)}(|E_{\omega_1}|^2 + {E_{\omega_2}}^2 + |{E_{\omega_3}}^2) E_{\omega_4} + \frac{6}{4}\chi^{(3)} E_{\omega_1} E_{\omega_2} E_{\omega_3} exp(j\theta_+) + ... \tag{A.28}$$

where θ is defined as

$$\theta = (\omega_1 + \omega_2 + \omega_3 - \omega_4)t - (k_1 + k_2 + k_3 - k_4)z \tag{A.29}$$

Substituting these terms in the nonlinear wave equation

$$\nabla^2 \mathbf{E}_s(z,t) + \frac{\omega_s^2}{c^2}\epsilon_L(\omega)\mathbf{E}_s(z,t) = -\mu_0\omega_s^2 \mathbf{P}_{NL}^{(3)}(z,t) \tag{A.30}$$

Leads to the following coupled wave equations [1],

$$\frac{dA_1}{dz} = j\gamma(|A_1|^2 + 2\sum_{k\neq 1}|A_k|^2)A_1 + 2j\gamma A_2^* A_3 A_4 e^{j\Delta kz} \tag{A.31}$$

$$\frac{dA_2}{dz} = j\gamma(|A_2|^2 + 2\sum_{k\neq 2}|A_k|^2)A_2 + 2j\gamma A_1^* A_3 A_4 e^{j\Delta kz} \tag{A.32}$$

$$\frac{dA_3}{dz} = j\gamma(|A_3|^2 + 2\sum_{k\neq 3}|A_k|^2)A_3 + 2j\gamma A_1 A_2 A_4^* e^{-j\Delta kz} \tag{A.33}$$

$$\frac{dA_4}{dz} = j\gamma(|A_4|^2 + 2\sum_{k\neq 4}|A_k|^2)A_4 + 2j\gamma A_1 A_2 A_3^* e^{-j\Delta kz} \tag{A.34}$$

$$\tag{A.35}$$

where the wave-vector mismatchΔk is given by

$$\Delta k = (n_3\omega_3 + n_4\omega_4 - n_2\omega_2 - n_1\omega_1)/c \tag{A.36}$$

The refractive indices n_1 to n_4 are the effective indices of the fiber at the different frequencies and γ is the nonlinear parameter of the fiber given by

$$\gamma = \frac{n_{2NL}\omega}{cA_{eff}} \tag{A.37}$$

where A_{eff} is the effective area of the propagating mode. It can be shown that [1] that these coupled wave equations can be integrated in the simple degenerate case where one strong beam interacts with two small amplitude signal beams. In that case the amplification of the weak bean is given by

$$g = 2 * \sqrt{(\gamma P)^2 - (\kappa/2)^2} \tag{A.38}$$

with κ

$$\kappa = \Delta k + 2\gamma P \tag{A.39}$$

The maximum gain ($g_{max} = \gamma P_0$) occurs at $\kappa = 0$, or at $\Delta k = -2\gamma P_0$. The range over which the gain exists is given by $0 > \Delta k > -4\gamma P_0$.

References

[1] Govind P Agrawal. *Nonlinear fiber optics*. Springer, 2000.